Thesis for the Degree of Doctor of Philosophy

Probing single-particle and collective states in atomic nuclei with Coulomb excitation

Douglas Di Julio

Division of Nuclear Physics
Department of Physics
Lund University
Sweden

Faculty opponent: Dr. Hans Fynbo
Department of Physics and Astronomy
Aarhus University
8000 Aarhus C, Denmark

Academic dissertation which, by the permission of the Faculty of Science at Lund University, will be publicly defended on Friday the 15th of February 2013, at 10.15 in lecture hall B at the Department of Physics, Sölvegatan 14C, Lund.

Probing single-particle and collective states in atomic nuclei with Coulomb excitation
Thesis for the Degree of Doctor of Philosophy

Printed in 2012 by Tryckeriet i E-huset, Lund, Sweden.

Division of Nuclear Physics
Department of Physics
Lund University
Box 118
SE-221 00 Lund
Sweden

LUNFD6 / (NFFR - 1033)/1 - 127 / (2012)
ISBN 978-91-7473-422-5

Typeset by the author using LaTeX 3.141592-1.21a-2.2

Abstract

A series of experiments and developments, related to stable and radioactive isotopes, have been carried out. These studies have focused on measuring the low-lying excitations of spherical and deformed nuclei using electromagnetic (Coulomb) excitation and also on developments in detector technology for upcoming radioactive ion beams facilities.

The low-lying excitations in the nuclei ^{107,109}Sn and ^{107}In have been investigated using low-energy Coulomb excitation at the REX-ISOLDE facility at CERN. The measured reduced transition probabilities were compared to predictions of nuclear structure models. In addition, a relativistic Coulomb excitation experiment was carried out using the FRS at GSI with the nucleus ^{104}Sn. These radioactive ion beam experiments provide important constraints for large-scale-shell-model calculations in the region of the doubly magic nucleus ^{100}Sn.

A stable Coulomb excitation experiment was also carried out in order to explore the properties of low-lying structures in the nucleus ^{170}Er. These measurements resulted in new data for the reduced transition matrix elements in this nucleus. The results were compared to predictions of models of deformed nuclei.

The last study contained in this work is related to the design of a new detector system, to be deployed at the upcoming radioactive ion beam facility FAIR. A prototype of the detector was tested with a 180 MeV proton beam and the results were compared to Geant4 simulations. The results highlight important constraints for the design of the full detector system.

Organization LUND UNIVERSITY Department of Physics Box 118 SE-221 00 Lund Sweden	Document name DOCTORAL DISSERTATION Date of issue December 17th, 2012 Sponsoring organization
Author(s) Douglas Di Julio	

Title and subtitle

Probing single-particle and collective states in atomic nuclei

Abstract

A series of experiments and developments, related to stable and radioactive isotopes, have been carried out. These studies have focused on measuring the low-lying excitations of spherical and deformed nuclei using electromagnetic (Coulomb) excitation and also on developments in detector technology for upcoming radioactive ion beams facilities.

The low-lying excitations in the nuclei 107,109Sn and 107In have been investigated using low-energy Coulomb excitation at the REX-ISOLDE facility at CERN. The measured reduced transition probabilities were compared to predictions of nuclear structure models. In addition, a relativistic Coulomb excitation experiment was carried out using the FRS at GSI with the nucleus 104Sn. These radioactive ion beam experiments provide important constraints for large-scale-shell-model calculations in the region of the doubly magic nucleus 100Sn.

A stable Coulomb excitation experiment was also carried out in order to explore the properties of low-lying structures in the nucleus 170Er. These measurements resulted in new data for the reduced transition matrix elements in this nucleus. The results were compared to predictions of models of deformed nuclei.

The last study contained in this work is related to the design of a new detector system, to be deployed at the upcoming radioactive ion beam facility FAIR. A prototype of the detector was tested with a 180 MeV proton beam and the results were compared to Geant4 simulations. The results highlight important constraints for the design of the full detector system.

Key words: Coulomb excitation, radioactive ion beams, reduced matrix elements, detector development

Classification system and/or index termes (if any):

Supplementary bibliographical information:		Language English
ISSN and key title:		ISBN 978-91-7473-422-5
Recipient's notes	Number of pages 137	Price
	Security classification	

Distribution by (name and address) D.D. Di Julio, Department of Physics, Box 118, 221 00 Lund, Sweden

Signature _____ Date 2012-12-17

List of Publications

This thesis is based on the work presented in the following publications and submitted manuscripts. The papers are referenced in the text using the indicated labels.

PAPER I: **Coulomb excitation of ^{107}Sn**
Eur. Phys. J. A. **48** *105 (2012)*
D.D. DiJulio, J. Cederkall, C. Fahlander, A. Ekström, M. Hjorth-Jensen, M. Albers, V. Bildstein, A. Blazhev, I. Darby, T. Davinson, H. De Witte, J. Diriken, Ch. Fransen, K. Geibel, R. Gernhäuser, A. Görgen, H. Hess, J. Iwanicki, R. Lutter, P. Reiter, M. Scheck, M. Seidlitz, S. Siem, J. Taprogge, G.M. Tveten, J. Van de Walle, D. Voulot, N. Warr, F. Wenander, and K. Wimmer

PAPER II: **Excitation strengths in ^{109}Sn: Single-neutron and collective excitations near ^{100}Sn**
Phys. Rev. C **86** *031302(R) (2012)*
D.D. DiJulio, J. Cederkall, C. Fahlander, A. Ekström, M. Hjorth-Jensen, M. Albers, V. Bildstein, A. Blazhev, I. Darby, T. Davinson, H. De Witte, J. Diriken, Ch. Fransen, K. Geibel, R. Gernhäuser, A. Görgen, H. Hess, J. Iwanicki, R. Lutter, P. Reiter, M. Scheck, M. Seidlitz, S. Siem, J. Taprogge, G.M. Tveten, J. Van de Walle, D. Voulot, N. Warr, F. Wenander, and K. Wimmer

PAPER III: **Coulomb excitation of ^{107}In**
Manuscript submitted to Phys. Rev. C
D.D. DiJulio, J. Cederkall, C. Fahlander, A. Ekström, M. Hjorth-Jensen, M. Albers, V. Bildstein, A. Blazhev, I. Darby, T. Davinson, H. De Witte, J. Diriken, Ch. Fransen, K. Geibel, R. Gernhäuser, A. Görgen, H. Hess, K. Heyde, J. Iwanicki, R. Lutter, P. Reiter, M. Scheck, M. Seidlitz, S. Siem, J. Taprogge, G.M. Tveten, J. Van de Walle, D. Voulot, N. Warr, F. Wenander, and K. Wimmer

PAPER IV: **Electromagnetic properties of vibrational bands in ^{170}Er**
Eur. Phys. J. A. **47** *25 (2011)*
D.D. DiJulio, J. Cederkall, C. Fahlander, A. Ekström, P. Golubev, K. Mattsson, D. Rudolph, G. de Angelis, S. Aydin, A. Y. Deo, E. Farnea, G. Farrelly, K. Geibel, C. He, J. Iwanicki, R. Kempley, N. Marginean, R. Menegazzo, D. Mengoni, R. Orlandi, Z. Podolyak, F. Recchia, P. Reiter, E. Sahin, J. Smith, P.A. Söderström, D.A. Torres, G.M. Tveten, C.A. Ur, J.J. Valiente-Dobón, A. Wendt, and M. Zielińska

PAPER V: **Proton in-beam tests of the Lund R^{3}B calorimeter prototype**
Nucl. Instr. and Meth. A **612** *127 (2009).*
D.D. DiJulio, V. Avdeichikov, J. Cederkall, P. Golubev, B. Jakobsson, H. Johansson, C. Tintori

Author's Contribution

Nuclear physics experiments that form the basis of a thesis are typically carried out in collaboration with a number of scientists where a student's supervisor is the experimental leader. The author had a leading role in many of the aspects of the current work. These are highlighted below.

Papers I-IV: Participated in the experiment, carried out the analysis, and wrote the paper as first author.

Paper V: Participated in the proton beam experiment, carried out the simulations and analysis of the experiment, and wrote the paper as first author.

Other publications not included in this thesis

A Gd-based gaseous electron multiplier detector for neutron scattering applications
Nucl. Instr. and Meth. A **579** *71 (2007).*
D.D. DiJulio, A.I. Hawari, R. Berliner

Examination of reactor grade graphite using neutron powder diffraction
J. Nucl. Mat. **392** *225 (2009)*
D.D. DiJulio and A.I. Hawari

Electric quadrupole moments of the 2_1^+ states in ^{100,102,104}Cd
Phys. Rev. C **80** *054302 (2009)*
A. Ekström, J. Cederkäll, D.D. DiJulio, C. Fahlander, M. Hjorth-Jensen, A. Blazhev, B. Bruyneel, P. A. Butler, T. Davinson, J. Eberth, C. Fransen, K. Geibel, H. Hess, O. Ivanov, J. Iwanicki, O. Kester, J. Kownacki, U. Köster, B.A. Marsh, P. Reiter, M. Scheck, B. Siebeck, S. Siem, I. Stefanescu, H.K. Toft, G.M. Tveten, J. Van de Walle, D. Voulot, N. Warr, D. Weisshaar, F. Wenander, K. Wrzosek, and M. Zielińska

Determination of the isomeric fraction in a postaccelerated radioactive ion beam using the coupled decay-chain equations
Nucl. Instr. and Meth. A **614** *303 (2010)*
A. Ekström, J. Cederkäll, D.D. DiJulio, C. Fahlander, J. Van de Walle

Two level scheme solvers for nuclear spectroscopy
Nucl. Instr. and Meth. A **654** *496 (2011)*
Kaj Jansson, Douglas DiJulio, Joakim Cederkäll

Sub-barrier Coulomb excitation of ^{107}Sn
J. Phys. Conf. Ser. A **381** *012073 (2012)*
D.D. DiJulio, J. Cederkall, A. Ekström, C. Fahlander, M. Hjorth-Jensen, for the IS459 Collaboration

Shell model based Coulomb excitation γ-ray intensity calculations in ^{107}Sn
Phys. Scr. **T150** *014012 (2012)*
D.D. DiJulio, J. Cederkall, A. Ekström, C. Fahlander, M. Hjorth-Jensen

Coulomb excitation of ^{104}Sn and the strength of the ^{100}Sn shell closure
Manuscript under preparation and to be submitted

Contents

Chapter 1

Introduction

The atomic nucleus is a small dense region located at the center of an atom. It consists of a number of neutrons and protons bound together by the short-ranged attractive nuclear force. The interplay between the nuclear force and the repulsive electromagnetic force leads to nuclei, with certain combinations of neutrons and protons, which are stable. These are situated along the line of stability in the nuclear chart. For the lightest of the stable nuclei, equal numbers of neutrons and protons are energetically favored. Heavier stable nuclei, on the other hand, require a neutron excess to balance the Coulomb repulsion provided by the increasing number of protons. Nuclei which are removed from the line of stability are unstable and undergo radioactive decay. On the neutron-rich side, nuclei convert neutrons into protons via β^- decay in order to approach stability. Similarly, proton-rich nuclei decay through β^+ emission or electron capture, converting protons into neutrons. The heaviest of nuclei can decay by emitting tightly-bound α particles. The limits of nuclear existence are marked by the location of the neutron and proton drip lines. Nuclei beyond these limits are no longer stable with respect to nucleon emission.

The vast majority of our current knowledge, in particular the foundations for many nuclear models, is derived from nuclei near the line of stability. Unstable nuclei are difficult to produce and study in the laboratory and the understanding of their properties is rather limited at this time. In total, there are about 300 stable nuclei. This pales in comparison to the thousands of identified and predicted number of unstable nuclei. One of the major questions in nuclear physics today is how well do nuclear models hold up for the nuclei far from stability. Over roughly the last 15 years, new technical developments in accelerator and detector technology have made it possible to push further into unexplored regions of the nuclear chart. Modern-day facilities can now provide beams of unstable nuclei in

significant enough quantities to make it possible to carry out experimental investigations of exotic short-lived radioactive nuclei. These studies may reveal new nuclear phenomena which will challenge modern nuclear structure models and our understanding of fundamental nuclear interactions.

The lowest-lying modes of excitation of an atomic nucleus largely depend on the number of neutrons and protons in the nucleus. Two types of low-lying states are single-particle and collective excitations. Single-particle excitations refer to those which involve the excitation of individual nucleons while collective excitations originate from the motion of all the nucleons working together in a group. A number of different theoretical models have been developed to understand these modes of motion. In principle, it should be possible starting from the nucleons and their basic interactions, to describe all nuclear properties under one unifying model. This scenario has so far yet to be realized, primarily related to an incomplete understanding of the nucleon-nucleon interaction and also to computational limits imposed by the shear size of the problem. Instead, nuclear models make use of a number of experimentally observed phenomena in order to simplify the situation and make calculations possible. For example, the nuclear shell model is founded on the experimental observation that nuclei with proton or neutron numbers $N = Z = 2, 8, 20, 28, 50, 82$ and 126, known as the magic numbers, have unique properties compared to other nearby nuclei in the nuclear chart. In the nuclear shell model, these nuclei can be treated as cores. To a first approximation, the shell-model state space for a nucleus can be divided into two regions. One region consists of the core of nucleons and the other is the valence space containing the remaining nucleons. The nuclear states are then described by the excitations of the individual valence nucleons and their interactions amongst themselves.

The nuclear shell model holds up well in the vicinity of magic nuclei. However, the model cannot describe features such as rotations and vibrations in nuclei, observed in regions of the nuclear chart distanced from the magic nuclei. These characteristics have led to the creation of a completely different model, developed by Bohr and Mottelson [1]. In this framework, the structure of a nucleus arises from the collective effort of all the constituent nucleons. These types of nuclei are characterized by a series of low-lying excitations with large transition probabilities, as oppose to single-particle excitations which and have small transition probabilities. Most nuclei exhibit properties which are characteristic of both single-particle and collective excitations and some combination of the different types of models may be needed to explain all their properties. In this regard, experimental studies exploring the interplay of collective and

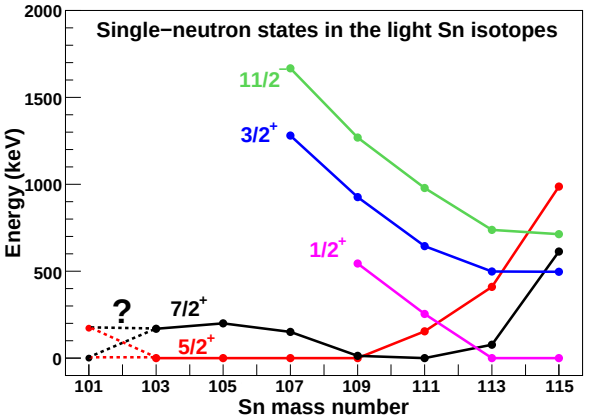

Figure 1.1: Experimentally determined single-neutron states in the light-Sn isotopes. The data points are taken from Ref. [3]. The spin ordering of the states in ^{101}Sn is debated at this time [4, 5].

single-particle degrees of freedom help bridge the gap between the different types of models.

One technique for studying low-lying excitations in nuclei is Coulomb excitation. As a beam of particles impinges on a stationary target, the projectile and target nuclei are mutually excited due to the time-dependent electromagnetic field between them. The power of the technique lies in the fact that the electromagnetic interaction is well understood [2]. At low energies, the repulsion of the Coulomb barrier keeps the two colliding nuclei separated and the interaction is purely electromagnetic in nature. The above two points make it possible to deduce nuclear data from experimental observations without encountering obstacles related to the strong nuclear force. The nuclear quantity of interest in Coulomb excitation measurements is the reduced transition matrix element between two nuclear states, or alternatively the reduced transition probability, which is proportional to the square of the reduced matrix element. The quantity can also be calculated using a various number of nuclear models and thus the Coulomb excitation technique is a means for directly testing these models.

A number of experimental and computational developments have also contributed to the applicability of the Coulomb excitation technique. Measurements today are carried out using large γ-ray detector arrays which provide highly efficient setups for measuring the γ rays emitted in nuclear reactions. Furthermore, these setups have been coupled with sensi-

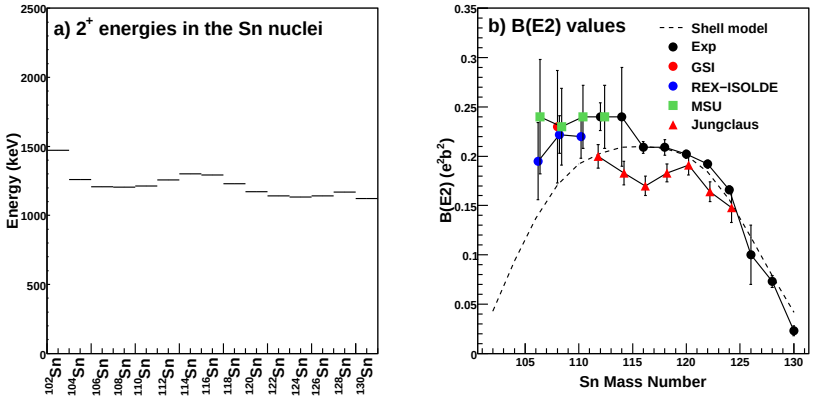

Figure 1.2: a) The measured first 2^+ excited states in the even-even Sn nuclei and b) the measured reduced transition probabilities of the first 2^+ excited states in the even-even Sn nuclei [6, 7, 8, 9, 10]. The shell-model calculations were carried out in Ref. [6] using a ^{100}Sn core.

tive particle detectors, allowing for accurate measurements of the angular dependence of the Coulomb excitation cross section. Modern day accelerators can also provide heavy ion beams at energies above the Coulomb barrier, making it possible to also study the excitation cross section as a function of beam energy and proton number. On the computational side, the development of Coulomb excitation analysis codes has made it possible to determine reduced matrix elements from highly complicated data sets. In a heavy ion beam experiment, a large number of nuclear states may be populated. The population for a single excited state can depend in a complicated way on all the nuclear states involved in the excitation. Semi-classical Coulomb excitation codes employing least-squares search routines combined with fast analytical approximations have been developed specifically to tackle these types of challenges.

This thesis describes the results of several different studies. These include an experiment with the odd-mass ^{107,109}Sn and ^{107}In isotopes, a relativistic measurement using the nucleus ^{104}Sn, a stable ion beam experiment with ^{170}Er, and the design of a new detector system for future radioactive ion beam experiments. The experimental studies, near ^{100}Sn, are primarily related to the nuclear shell model. The Coulomb excitation experiments explored the collective properties of low-lying nuclear excited states in the odd-mass and even-even neutron-deficient Sn nuclei, ^{107,109}Sn and ^{104}Sn, and also in the proton-hole nucleus ^{107}In. To a first approximation, the

low-lying states in the Sn nuclei can be described in shell-model calculations by the excitations of neutrons outside of a ^{100}Sn core. One important input parameter for such calculations is the set of single-neutron energies relative to ^{100}Sn. These states are largely unknown as the nucleus ^{101}Sn is difficult to produce in the laboratory environment. One approach to get at them is instead to trace their migration across the Sn isotopic chain, as shown in Fig. 1.1, where the first five states above $N = 50$ are tentatively assigned down to ^{109}Sn. The motivation for the experiments in the odd-mass Sn nuclei was to confirm the previous findings in ^{109}Sn and to search for single-neutron states in ^{107}Sn. The motivation for the ^{104}Sn experiment, on the other hand, concerned the recently observed increase in the reduced transition probabilities in the even-even Sn isotopes (see Fig 1.2). The unexpected enhanced transition strengths call into question the validity of using ^{100}Sn as a core. The increased transition strengths may indicate the importance of neutron and/or proton excitations across the $N = Z = 50$ shell gap, which are typically omitted in the shell-model calculations. In this regard, it is also interesting to explore the properties of nuclei removed by a few protons from $Z = 50$ in order to study the proton-neutron interaction. This was the aim of the ^{107}In Coulomb excitation experiment.

The next study presented in this thesis concerns ^{170}Er, which has the typical properties associated with a deformed nucleus described by the collective model of Bohr and Mottelson. The Coulomb excitation technique is particularly well suited for investigating the excitations of these types of nuclei, as discovered in earlier studies [11], due to their large transition probabilities and low-lying energies. The nucleus ^{170}Er is unique in that it exhibits two low-lying rotational bands at nearly the same energy. Through the Coulomb excitation technique, it is possible to investigate the interactions between these bands and compare them with predictions of collective nuclear models.

Progress in the field of experimental nuclear physics is largely driven by advancements in accelerator and detector technology. The final work contained in this thesis is related to the development of a new detector system, to be used in upcoming nuclear physics experiments with radioactive ion beams. The detector may be used in investigations employing a reaction closely related to Coulomb excitation, known as Coulomb dissociation.

As a final note, the importance of fundamental investigations in nuclear physics should not be understated. From a historical perspective, basic research in nuclear physics has led to a number of important advancements which have impacted society. The discovery of the neutron by James Chadwick in 1932 paved the way for the development of nuclear power and led to events which shaped the political landscape in the latter

half of the 20^{th} century. Nuclear power currently offers one of the most promising methods for meeting the increasing demand in energy production while limiting the emission of greenhouse gas. New advancements in safety and waste technology will only make this option more attractive. Other fields which have benefited from nuclear physics research include nuclear medicine, earth science, and materials science and engineering. A new and exciting possible application of nuclear physics is related to using the properties of weakly-interacting neutrinos, emitted during radioactive decay, to help predict earthquakes. In the future, discoveries and developments related to radioactive ion beams may ultimately lead to additional important technological advancements which are beneficial for society.

Chapter 2

Nuclear Models

The theoretical nuclear structure landscape comprises a rich collection of nuclear models. The different models provide a basic understanding of the variety of phenomena observed in atomic nuclei, which have not as of yet, been explained under the framework of a single unifying model. If the nature of the nucleon-nucleon interaction was fully known and if powerful enough computers were available, it may be possible to calculate any desired nuclear property starting with the individual nucleons themselves. This approach is not feasible with the current understanding of the nuclear force and is hindered by computational limits when attempting to solve the many-body Schrödinger equation. For these reasons, a large variety of nuclear models have been developed. However, it is not so that a model developed for one group of nuclei will necessarily be successful in describing the properties of a different group of nuclei. Certain nuclei may require the application of two or more different models to describe their features.

The available models can be grouped into roughly three categories: single particle, collective, and models combining both collective and single-particle degrees of freedom. The most successful model is the nuclear shell model, which has its foundation in the single-particle motion of the constituent nucleons in a mean-field potential, much like electrons in the atom. The approach still has limited application to nuclei as the required model space grows rapidly as the number of states in a calculation increases. Many other models have been developed which are based on an efficient means of truncating the relevant space to make calculations possible. The second group of models are founded on the collective motion of the nucleus as a whole, analogous to the rotations and vibrations of a liquid drop. Generally speaking, these models can be related to the shell model by considering the motion of an individual particle in a rotating deformed po-

tential. However, there exists no simple method which links the the two models together. It may be that these types of motion can arise within the single-particle framework given a complete understanding of the nuclear force and powerful enough computers to solve the nuclear many-body problem. The third group of models build their foundations on some combination of both collective and single-particle degrees of freedom.

In the following discussion, the nuclear models of interest for the analysis and discussion in the later chapters are introduced. The focus is on features of the models which are relevant for the work presented in this thesis.

2.1 The nuclear shell model

2.1.1 The average potential

The basic first order assumption of the nuclear shell model is that the individual nucleons move in orbits, also known as j-shells, independently of each other. The introduction of the concept of the average potential is twofold. First, there is a large amount of supporting evidence for the existence of shell structure in nuclei. The strongest evidence is the experimentally observed magic numbers, $N = Z = 2, 8, 20, 28, 50, 82$ and 126. These can be viewed as major shell closures. The first excited states of these nuclei can be created only by lifting a single nucleon out of the closed shell. In nuclei with unfilled shells, the lowest excited states can be formed by recoupling the angular momenta of the nucleons in the unfilled orbits. One would therefore expect that the first excitations would lie at higher energies in closed shell nuclei than in nuclei with unfilled shells. This agrees well with experimental observation.

The second reason for the introduction of the average potential is motivated from a theoretical point of view. To calculate properties of a nucleus it is necessary to solve the Schrödinger equation to obtain the set of eigenvalues and eigenfunctions. The starting point is the nuclear A-body Hamiltonian, given by

$$H = \sum_{i=1}^{A} T_i + \sum_{1=i<j}^{A} W_{i,j}(\vec{r}_i, \vec{r}_j), \tag{2.1}$$

where $W_{i,j}$ represents the two-body interaction between nucleons. An exact solution of the Schrödinger equation using this Hamiltonian does not exist. The introduction of the average potential makes it possible to move forward and calculate quantities which can be compared to experiment.

The motion of a single particle moving in a central potential is described by the Hamiltonian

$$H_0 = \sum_{i=1}^{A} [T_i + U(\vec{r}_i)], \tag{2.2}$$

where $U(\vec{r}_i)$ is the average potential. On first sight, it may seem difficult to pinpoint the origin of the average potential for which the individual nucleons move in. In the case of the atomic shell model, the Coulomb force of a heavy nucleus provides a center for the lighter electrons. The situation is not as clear for the nuclear case. However, the potential can be shown to naturally arise from the convolution of the nuclear density with a two-body interaction acting between nucleons. The average interaction from all the other nucleons on the i^{th} nucleon is given by

$$U(\vec{r}_i) = \sum_{j \neq i}^{A} \int \psi_j^*(\vec{r}_j) W_{i,j}(\vec{r}_i, \vec{r}_j) \psi_j(\vec{r}_j) d\vec{r}_j. \tag{2.3}$$

The single-particle wave functions can then be calculated by solving the single-particle Schrödinger equation, given by

$$\frac{-\hbar^2}{2m} \Delta\psi_i(\vec{r}_i) + \sum_{j \neq i}^{A} \int \psi_j^*(\vec{r}_j) W_{i,j}(\vec{r}_i, \vec{r}_j) \psi_j(\vec{r}_j) d\vec{r}_j \cdot \psi_i(\vec{r}_i) = \epsilon_i \psi_i(\vec{r}_i), \tag{2.4}$$

where ϵ_i are the eigenfunctions. Here, anti-symmetrization between nucleons is not taken into account. By knowing the wave functions and the interaction between two nucleons, it is possible to calculate the average potential. However, in order to know the wave functions one must first solve the Schrödinger equation with an average potential. A common way forward is to use an iterative approach, such as the Hartree-Fock method. The general idea is to take a guess for the wave functions and solve the Schrödinger equation. The resulting new set of wave functions can be used to solve the Schrödinger equation again and the process is repeated until convergence is achieved. In the case above, in which anti-symmetrization between two nucleons is ignored, the process yields a potential called the Hartree field. Requiring anti-symmetrization leads to a self-consistent potential which depends on two terms. The first is the Hartree term and the second is known as the exchange term. The field calculated in this way is known as a Hartree-Fock self-consistent field.

The mean field is often approximated using potentials with well known solutions, such as the harmonic oscillator, $U(r) = \frac{1}{2} m\omega^2 r^2$, which has the solutions

$$E = \hbar\omega(N + \frac{3}{2}), \tag{2.5}$$

where N denotes the major oscillator number. The gaps between the shells correspond to $N = 2, 8, 20, 40, 70$ and 112, where only the lower three numbers agree with the experimentally determined magic numbers. One possibility is to instead use a more realistic shape of the potential. In a heavy nucleus, a nucleon in the center should experience no net force, suggesting that the potential should be flat in this region. The addition of an l^2 term leads to this effect. A particle at a distance further from the center, which has a higher orbital angular momentum, will feel a stronger force and thus have a lower energy. A Woods-Saxon potential, which has the correct behavior at large distances, also produces a similar effect. Both corrections break the l degeneracy of the shells but still do not produce the correct sequence of magic numbers. The major breakthrough came with the introduction of a strong spin orbit term in the potential, $V_{so} = -V_{so}(r)\vec{l}\cdot\vec{s}$, which splits each state according to $j = l \pm s$ [12, 13]. The interaction pushes several of the orbits down into the lower oscillator shells leading to the proper reproduction of the magic numbers. The effect of the spin orbit force on the single-particle energies is highlighted in Fig. 2.1.

2.1.2 Residual interaction

The previous discussion has revolved mainly around the individual motion of nucleons in the mean-field potential. Experimentally, this picture only holds up well for a very few select group of nuclei; those with one nucleon or hole outside of a closed shell. For nuclei with a few nucleons outside of a closed shell it becomes important to consider the residual interaction between the nucleons. It can be illustrative to look into more detail at Eq. 2.1. The average potential can be introduced in the Hamiltonian by adding and subtracting it to Eq. 2.1, resulting in

$$H = \sum_{i=1}^{A}[T_i + U(\vec{r}_i)] + [\sum_{1=i<j}^{A} W_{i,j}(\vec{r}_i, \vec{r}_j) - \sum_{i=1}^{A} U(\vec{r}_i)]. \tag{2.6}$$

The Hamiltonian can further be written as a sum of a core part and a valence nucleon part. For a simple two nucleon and core system, where the core particles are indicated by the indices $i = 3, ..., A$, the core Hamiltonian becomes

$$H_{core} = \sum_{i=3}^{A}[T_i + U(\vec{r}_i)] + [\sum_{3=i<j}^{A} W_{i,j}(\vec{r}_i, \vec{r}_j) - \sum_{i=3}^{A} U(\vec{r}_i)], \tag{2.7}$$

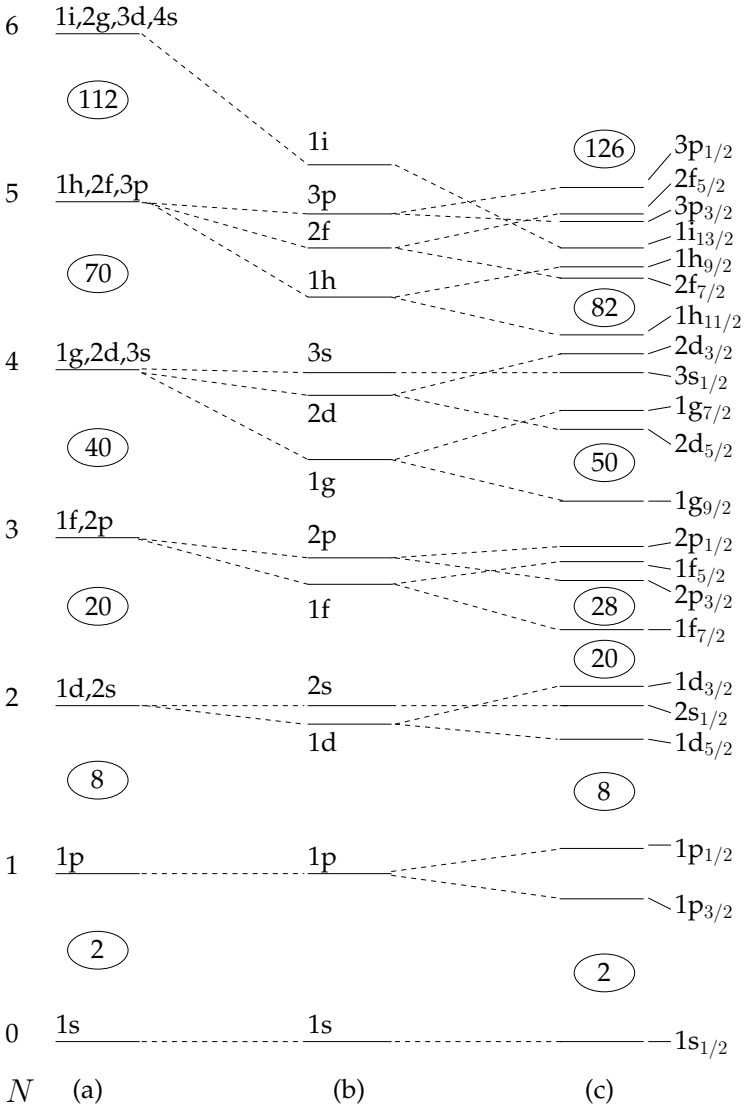

Figure 2.1: The single-particle energies for the (a) simple harmonic oscillator, (b) intermediate form between harmonic oscillator and square well and (c) with spin-orbit interaction. The number N represents the major oscillator shell. The figure was inspired by Fig. 3.2 in Ref. [14].

while the Hamiltonian for the two particles is given by

$$H_{12} = \sum_{i=1}^{2}[T_i + U(\vec{r}_i)] + [\sum_{i=1}^{2}\sum_{j=3}^{A} W_{i,j}(\vec{r}_i, \vec{r}_j) + W_{1,2}(\vec{r}_1, \vec{r}_2) - \sum_{i=1}^{2} U(\vec{r}_i)]. \quad (2.8)$$

The two-particle term can also be expressed as two parts. The first corresponds to the single-particle energies relative to the core, given by

$$H_{12}^0 = [T_1 + U(\vec{r}_1)] + [T_2 + U(\vec{r}_2)] \quad (2.9)$$

and the second term, containing the residual interaction, given by

$$H_{12}^1 = [\sum_{j=3}^{A} W_{1,j}(\vec{r}_1, \vec{r}_j) - U(\vec{r}_1)] + [\sum_{j=3}^{A} W_{2,j}(\vec{r}_2, \vec{r}_j) - U(\vec{r}_2)] + W_{1,2}(\vec{r}_1, \vec{r}_2). \quad (2.10)$$

If it were so that the average potential was simply a sum of the two-particle interactions of all the nucleons, then only the term $W_{1,2}(\vec{r}_1, \vec{r}_2)$ would remain in the above equation. However, in a typical calculation the core part and the valence part of the calculation are separated and the two-body interaction must be replaced with the residual two-body interaction $v_{1,2}(\vec{r}_1, \vec{r}_2)$. This accounts for the fact that the average potential does not fully describe the interaction between the core and valence particles.

The introduction of the residual interaction leads to mixing of the pure shell-model states. The perturbed wave functions will instead be based on linear combinations of the pure states, given as

$$\psi_p = \sum_{k=1}^{g} a_{kp}\psi_k^0, \quad (2.11)$$

where a_{kp} represents the amplitude of state k in the total wave function, g is the total number of configurations considered in the mixing, and $p = 1, ..., g$. In this case, the Schödinger equation can be shown to be

$$\sum_{k=1}^{g} H_{lk}a_{kp} = E_p a_{lp}, \quad (2.12)$$

and in matrix form,

$$\begin{bmatrix} H_{11} & H_{12} & \cdots & H_{1g} \\ H_{21} & H_{22} & \cdots & H_{2g} \\ \vdots & \vdots & \ddots & \vdots \\ H_{g1} & H_{g2} & \cdots & H_{gg} \end{bmatrix} \begin{bmatrix} a_{1p} \\ a_{2p} \\ \vdots \\ a_{gp} \end{bmatrix} = E_p \begin{bmatrix} a_{1p} \\ a_{2p} \\ \vdots \\ a_{gp} \end{bmatrix}, \quad (2.13)$$

where the Hamiltonian terms are given by

$$H_{lk} = \langle \psi_l^0 | H_0 | \psi_k^0 \rangle + \langle \psi_l^0 | H_{res} | \psi_k^0 \rangle. \tag{2.14}$$

The first term is just the single-particle energies, which correspond to the eigenvalues of the Schödinger equation with the unperturbed Hamiltonian. The second term in Eq. 2.14 represents the residual interaction, which contributes to both the diagonal and off-diagonal elements. To find the eigenvalues of Eq. 2.13 requires that the determinant satisfies the following condition,

$$\begin{vmatrix} H_{11} - E_p & H_{12} & \cdots & H_{1g} \\ H_{21} & H_{22} - E_p & \cdots & H_{2g} \\ \vdots & \vdots & \ddots & \vdots \\ H_{g1} & H_{g2} & \cdots & H_{gg} - E_p \end{vmatrix} = 0. \tag{2.15}$$

The problem thus boils down to finding an efficient means for diagonalizing the energy matrix.

To summarize, the basic idea begins with the construction of the matrix H_{lk}. The unperturbed part of the Hamiltonian is just the single-particle energies of the individual nucleons moving in the average field and contributes to only the diagonal elements of H_{lk}. The residual interaction introduces corrections to the diagonal and off-diagonal elements into the calculation and diagonalization of the energy matrix yields the perturbed energies and wave functions. The single-particle energies and two-body matrix elements make up the two primary input parameters to shell-model calculations. The basis for the discussion regarding the residual interaction and mixing can be found in Ref. [15], which provides a more detailed overview of the material presented here.

2.1.3 Effective interactions based on realistic nucleon-nucleon potentials

The application of the previous formulation to atomic nuclei introduces several additional obstacles. The first is that the perturbation approach is only valid if the residual interaction is weak. The repulsive core of the nucleon-nucleon interaction means that direct application using perturbation theory is not possible. Secondly, the dimensions of the single-particle basis grow very fast with the addition of neutrons and protons, quickly making it impossible to perform shell-model calculations within a reasonable time. To solve this issue, further truncation of the model space must be carried out.

Ideally one would like to derive the free nucleon-nucleon interaction directly from quantum chromodynamics. This has yet to be carried out, however some progress has been made recently using chiral effective theory (see the review article Ref. [16]). An alternative is to use models based on meson-exchange theory. The parameters of the model are adjusted to fit nucleon-nucleon scattering data such as phase shifts and some properties of the deuteron. The work presented in this thesis has been carried out using such a potential, known as the CD-Bonn potential [17].

In the truncated shell-model space, there is no reason to believe that the nucleon-nucleon interaction should be the free nucleon-nucleon interaction. Instead, one has to introduce the concept of an effective interaction. The hope is that this interaction will account for all the configurations which were not included in the model space. In a typical calculation the model space includes a few single-particle orbits just above a magic nucleus. This is usually a reasonable assumption as the energy gaps between the major shells are larger than the energy gaps between the orbits within a shell. In the current work, the effective interaction was derived from the CD-Bonn potential using the G-matrix renomalization method. An overview of the procedure applied to the Sn nuclei can be found in Ref. [18].

The reduction of the shell-model space also introduces the concept of the effective charge, similar to the reasons discussed for the need for an effective interaction. The calculation of the $E2$ electromagnetic transition matrix elements, $\langle\psi_i|E2_{eff}|\psi_f\rangle$, is carried out by operating on the wave functions of the states with the electric multipole operator $E2_{eff}$. In the truncated model space, the wave functions are only projections of the full wave functions. If the full wave functions were known, the bare operator could be used in the standard form. Instead, the $E2$ operator must be renormalized by the effective charge e_{eff}. This hopefully accounts for any missing contributions to the full wave functions omitted during the truncation of the shell-model space. The effective charges are another important input parameter for shell-model calculations.

2.1.4 The seniority scheme

One efficient truncation of the shell-model space is known as the seniority scheme [19, 20]. The method will only be briefly introduced in this section, but is relevant for the Sn nuclei and is particularly useful for single closed shell nuclei if strong pairing correlations are present. The basic idea of the scheme takes advantage of the fact that like particles tend to pair in groups of two to $J = 0^+$. The seniority of a state, ν, is defined as the number of

unpaired nucleons in a given j^n configuration with angular momentum J. For example, the $J = 16$ state for the configuration $(h_{11/2})^4$ has seniority four, as all four particles must be maximally aligned. One simple prediction of the model is that for a particular j-orbit, the energy level differences between $\nu = 0$ and $\nu = 2$ states are independent of n and constant. When more than one j-orbit is occupied, admixtures of the j^n configurations can be accounted for by using a generalized seniority scheme [21]. There are two important predictions for the Sn nuclei. The first being that the energies of the 2^+ states should be roughly constant across the isotopic chain. The even-even Sn nuclei are an excellent example of this behavior, as indicated in Fig. 1.2 panel a. The second prediction is that the reduced transition probabilities of these states should exhibit a parabola like behavior which peaks at midshell for the major neutron shell. The reduced transition probabilities on the neutron rich side of the shell show the expected behavior while evidence has mounted for deviations from this trend on the neutron deficient side of the shell (Fig. 1.2 panel b). Results from large-scale-shell-model calculations using a ^{100}Sn core are also shown in the figure and show the expected behavior from the seniority scheme. Interestingly, recent measurements also indicate a loss of collectivity near the midshell (Fig. 1.2 panel b). These results have however been shown to be consistent with the generalized seniority scheme and related to the filling of the j-orbits [22].

2.2 Geometric collective model

2.2.1 Collective coordinates

The collective model of Bohr and Mottelson [1] describes the low-lying excitations of a nucleus in terms of the collective effort of all the constituent nucleons. The nucleus can be viewed as a liquid drop and a point on the surface of the drop can be described by the following expansion in spherical harmonics

$$R(\theta, \phi) = R_0(1 + \sum_{\lambda\mu} \alpha_{\lambda\mu} Y^*_{\lambda\mu}(\theta, \phi)), \tag{2.16}$$

where $\alpha_{\lambda\mu}$ are called the collective coordinates, R_0 is the equilibrium radius, λ is the multiple order, and $\mu = \lambda, \lambda - 1, ..., -\lambda$. The mutipoles of the expansion correspond to different types of nuclear motion. The monopole part relates to a change of the nuclear radius, which does not occur at low energies. The dipole part corresponds to a shift of the center of mass of the nucleus and thus no changes in the nuclear shape. The quadrupole term is the lowest multipole which influences the nuclear shape and is the

most important mode for the work carried out in this thesis. The collective coordinates can thus be reduced to the five quadrupole variables, α_μ, in the laboratory frame of reference. It is however often useful to consider their shapes relative to the nuclear axis of symmetry. This is carried out by transforming the laboratory coordinates to the intrinsic coordinates which results in two non-vanishing intrinsic deformation variables, usually written as

$$a_0 = \beta cos\gamma, \quad a_2 = \tfrac{\sqrt{2}}{2}\beta sin\gamma. \tag{2.17}$$

The variables β and γ provide a very simple means for describing nuclear shapes. The relation between the shape parameters and the nuclear radius is given by

$$\delta R_k = \sqrt{\frac{5}{4\pi}}\beta R_0 \cos(\gamma - k\frac{2\pi}{3}), \tag{2.18}$$

where k represents the three intrinsic axes of the nucleus. Adjustments of the parameter β only effect the extent of the quadrupole deformation while γ changes the degree of axial symmetry. A prolate axially symmetric nucleus is described with $\beta \neq 0$ and $\gamma = 0^o$ while an oblate axially symmetric shape is given by $\beta \neq 0$ and $\gamma = 60^o$. Increments of the parameter γ in multiples of 60^o only changes the orientation of the nucleus. In this way, all possible nuclear shapes can be described by the plane defined by $\beta \geq 0$ and $0^o \leq \gamma \leq 60^o$ (Fig. 2.2 panel a). The contours represent a typical potential energy surface for an axially symmetric prolate nucleus.

2.2.2 Rotational and vibrational states

Two types of collective motion are rotations and vibrations. A deformed nucleus can undergo both rotation and vibration. As no rotations are allowed quantum mechanically with respect to a symmetry axis, spherical nuclei can only vibrate. The Hamiltonian for an axially symmetric rotor is given by

$$H_{rot} = \frac{\vec{R}^2}{2\mathcal{J}}, \tag{2.19}$$

where $\mathcal{J}$ represents the moment of inertia and $\vec{R}$ is the rotational angular momentum. The relationship between the total angular momentum $\vec{I}$, the collective angular momentum $\vec{R}$, and the intrinsic angular momentum $\vec{J}$, is shown in Fig. 2.2 panel b. The projection of the total angular momentum onto the symmetry axis is known as K. When rotational motion is superimposed on an intrinsic excitation, the total angular momentum will

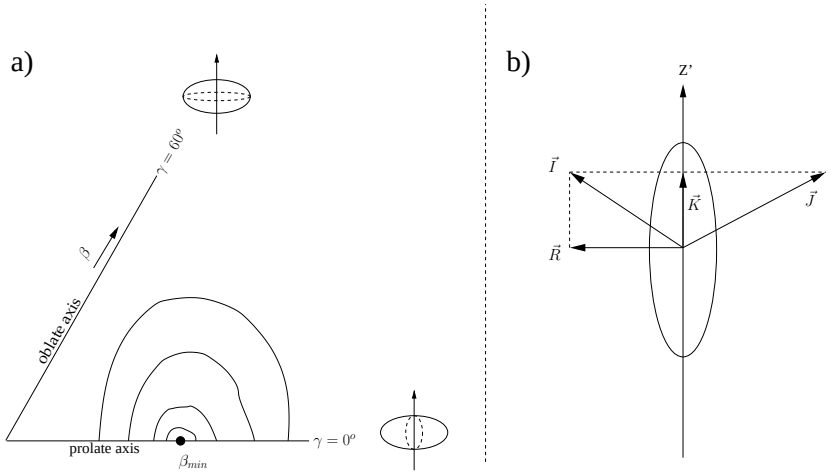

Figure 2.2: a) The β and γ plane describing various shapes of nuclei and b) the relation between the angular momentum vectors of a nucleus. The potential energy contour lines in a) represent a typical deformed axially symmetric nucleus, such as ^{170}Er.

be equal to $I = K, K+1, K+2, ...$ The energy spectrum is classified in terms of bands with constant values of K, given by

$$E = \frac{\hbar^2}{2\mathcal{J}}(I(I+1) - K^2). \tag{2.20}$$

The ground-state band of an even-even rotational nucleus has $K = 0$.

One type of intrinsic excitation is believed to be due to vibrations of the nuclear shape. These can be accounted for in Eq. 2.16 by introducing a time dependence in the collective coordinates. The Hamiltonian representing this system, for quadrupole vibrations, is given as

$$H_{vib} = \frac{1}{2}\sum_{\mu} C|\alpha_\mu|^2 + \frac{1}{2}\sum_{\mu} D|\dot{\alpha}_\mu|^2, \tag{2.21}$$

where $\dot{\alpha}_\mu$ is the time derivatives of the collective coordinates. The constants C and D are the restoring force and mass parameters, respectively. The quantum of vibration is called a phonon and the energy spectrum can be described in terms of these quanta as

$$E_N = \hbar\omega(N + \frac{5}{2}), \tag{2.22}$$

with $\omega = \sqrt{\frac{C}{D}}$ and N is the number of quadrupole phonons.

As discussed previously, a deformed nucleus can undergo vibrations in the β and γ directions and in addition have rotations superimposed on the vibrations. The energy spectrum in the rotation-vibration model is given as [23]

$$E = \hbar\omega_\beta(n_\beta + \frac{1}{2}) + \hbar\omega_\gamma(2n_\gamma + \frac{1}{2}|K| + 1) + \frac{\hbar^2}{2\mathcal{J}}(I(I+1) - K^2), \quad (2.23)$$

where n_β and n_γ are the β and γ quantum numbers. Excited states with the same values of n_β, n_γ, and K form rotational bands according to the simple $I(I+1)$ dependence. Typically the β- and γ-vibrational bands occur around 1 MeV in deformed nuclei, corresponding to the quantum numbers $K = 0, n_\beta = 1, n_\gamma = 0$ and $K = 2, n_\beta = 0, n_\gamma = 0$, respectively. The γ-vibrational state has $n_\gamma = 0$ due to the rotation-vibration coupling. This coupling leads to excited states which include a γ-vibrational component when K is not equal to zero [23, 24]. The two different types of vibrational bands can be distinguished from each other by examining both the band-head spins and the spins of the members of the rotational bands. The β band only contains even spin members while the γ band contains both even and odd members. For bands with $K = 0$, the rotational component of the wave function for odd I members of the band vanishes [24]. In addition to states built on single-phonon excitations, one would would also expect two-phonon excitations. These could be, for example, two-phonon γ-excitations built with $K = 0$ and $K = 4$. The identification and classification of such states has historically been the focus of many experiments in the Er nuclei.

2.2.3 Reduced matrix elements

One feature of the collective model of Bohr and Mottelson is that it predicts very simple relations for the reduced matrix elements between excited states of a nucleus. If there is not a strong coupling between the intrinsic and rotational degrees of freedom, known as the adiabatic approximation, the reduced matrix elements $\langle K_2 I_2 \| \mathcal{M}(\lambda) \| K_1 I_1 \rangle$, to the leading order are given by

$$\langle K_2 I_2 \| \mathcal{M}(\lambda) \| K_1 I_1 \rangle = (2I_1 + 1)^{1/2} \langle I_1 K_1 \lambda, \Delta K | I_2 K_2 \rangle \langle K_2 | \mathcal{M}(\lambda, \nu) | K_1 \rangle \xi. \quad (2.24)$$

For transitions between two bands or within a band, this means that all the reduced matrix elements can be described by a single intrinsic matrix element $\langle K_2 | \mathcal{M}(\lambda, \nu) | K_1 \rangle$, multiplied by a spin correction and a Clebsch

Gordan coefficient $\langle I_1 K_1 \lambda \Delta K | I_2 K_2 \rangle$. The constant $\xi = \sqrt{2}$ if K_2=2 and K_1=0 and is equal to 1 if both bands have $K = 0$.

For an axially symmetric nucleus, the intrinsic matrix element in Eq. 2.24 is a direct measure of the deformation of a particular K band. The intrinsic quadrupole moment is related to the intrinsic matrix element by

$$eQ_0 = (\frac{16\pi}{5})^{1/2} \langle K | \mathcal{M}(\lambda, \nu) | K \rangle, \tag{2.25}$$

which in turn is related to the deformation parameter β by

$$Q_0 = \frac{3}{\sqrt{5\pi}} Z R_0^2 \beta (1 + 0.16\beta). \tag{2.26}$$

In this way, the various shape parameters of axially symmetric nuclei can be inferred by measuring the in-band reduced matrix elements of a rotational band.

Higher order effects, such as an interaction between the vibrational and rotational modes of motion, lead to deviations from Eq. 2.24. The interaction results in band mixing. For simple two-band mixing between the ground-state and γ-vibrational bands, the reduced $E2$ matrix elements are given by

$$\begin{aligned} \langle K_2 I_2 || \mathcal{M}(E2) || K_1 I_1 \rangle =& (2I_1 + 1)^{1/2} \langle I_1 K_1 2 \Delta K | I_2 K_2 \rangle \times \\ & (M1 + M2(I_2(I_2 + 1) - I_1(I_1 + 1)))\sqrt{2}, \end{aligned} \tag{2.27}$$

where M_1 is the intrinsic matrix element between the bands and M_2 is the coupling matrix element. A simple way to analyze the extent of mixing between two rotational bands is to plot the square root of the downward $B(E2)$ values (see Eq. B.2) divided by $\langle I_\gamma 22 - 2 | I_g 0 \rangle$ versus the spin dependence $(I_g(I_g + 1) - I_\gamma(I_\gamma + 1))$. Such a graph is known as a Mikhailov plot. If the two-band mixing formalism is applicable, the points will lie on a straight line described by the parameters M_1 and M_2. A horizontal line indicates that there is no mixing between the two bands. Potential sources of deviations from a straight line may be due to the presence of undetected $M1$ components, differences in the quadrupole moments of the bands, assumed to be zero in the model, and possibly the mixing with additional intrinsic excitations. A formalism for three-band mixing has been presented in Refs. [25, 26].

For the the leading order relation (Eq. 2.24), transitions between bands with $|K_1 - K_2| > \lambda$ are forbidden. However, $M1$ transitions between the ground-state and γ-vibrational bands have been observed. A coupling with a $K = 0$ band could give rise to $M1$ transitions to the ground-state band. Another possible origin could be related to mixing with nearby

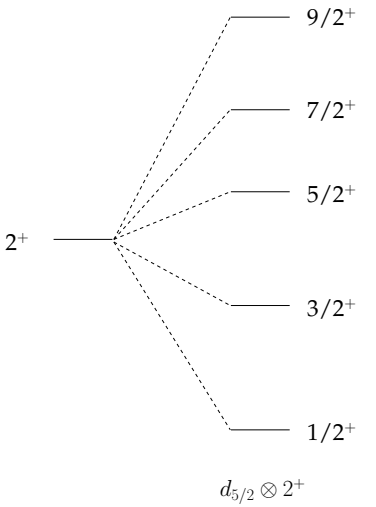

Figure 2.3: Schematic illustration of the coupling of a single particle in the $d_{5/2}$ orbit and a 2^+ core state.

$K = 1$ bands and the reduced matrix elements can be calculated using the spin-dependent model of Bohr and Mottelson, given as

$$\langle K_2 I_2 || \mathcal{M}(\lambda) || K_1 I_1 \rangle = (2I_1+1)^{1/2} \langle I_1 (K_2 - \lambda) \lambda \lambda | I_2 K_2 \rangle \times \left(\frac{(I_1 - K_1)!(I_1 + K_1 + n)!}{(I_1 - K_1 - n)!(I_1 + K_1)!} \right)^{1/2} \langle K_2 | m_{\Delta K, \nu} | K_1 \rangle \xi, \tag{2.28}$$

with $\xi = \sqrt{2}$ when $K_1 = 0$ and equal to 1 otherwise. The degree of K forbiddeness is given by $n = |K_1 - K_2| - \lambda$.

The geometric collective model also predicts a simple relation for $M1$ transitions between two $K = 0$ bands, given as

$$\langle K_2 I_2 || \mathcal{M}(M1) || K_1 I_1 \rangle = ((2I_1+1) I_1 (I_1+1))^{1/2} m(\mathcal{M}1) \delta(I_1, I_2). \tag{2.29}$$

The parameter $m(\mathcal{M}1)$ represents the intrinsic element between the two $K = 0$ bands. The coupling schemes presented in this section form the foundation for the analysis of the ^{170}Er data.

2.3 Core-excitation model

The core-excitation model of de-Shalit [27, 28] is a model for odd-A nuclei which assumes that the low-lying excited states of a nucleus result from the coupling of the odd nucleon to a core which has similar properties as

an excited state in a nearby even-even nucleus. If the single-particle excitations are much higher in energy than excitations of the collective core state, then a likely situation is the excitation of the core while the single-nucleon remains in the ground-state orbital. When no interaction between the particle and core is present, the possible states resulting from the angular momentum coupling of the particle and the core are degenerate. The particle-core coupling breaks the degeneracy of the states and yields a multiplet of core-coupled states. The idea is illustrated schematically in Fig. 2.3. In some detail, the matrix element between two states is given by [27, 28]

$$\langle J_c' j_p J_f || Q^k || J_c j_p J_i \rangle = (-1)^{J_c'+j_p+J_f} [(2J_f+1)(2J_i+1)]^{1/2} \times [\langle J_c' || Q_c^k || J_c \rangle \times \begin{Bmatrix} J_c' & J_f & j_p \\ J_i & J_c & k \end{Bmatrix} + (-1)^{J_i-J_f} \langle j_p || Q_p^k || j_p \rangle \begin{Bmatrix} j_p & J_f & J_c \\ J_i & j_p & k \end{Bmatrix} \delta_{J_c J_c'}], \tag{2.30}$$

where the multipole Q is divided into a core and particle component. In the model, the multipole is of the form of the standard static multipole moment of order k.

For transitions with $J_c = 2$ to the ground state, i.e. $J_c = 0$, Eq. 2.30 leads to a simple relation between the $E2$ transition of the core excitation and the members of the multiplet [27], given by

$$B(E2, I_i \to I_f) = \frac{2I_f+1}{2I_i+1} \frac{B(E2,\uparrow)_{core}}{5}, \tag{2.31}$$

where $B(E2)_{core}$ is the reduced transition probability of the core. Furthermore, the center of gravity of the multiplet corresponds to the unperturbed position of the core-excited state, given by

$$\sum (2J+1)(E(J) - E_c) = 0, \tag{2.32}$$

where E_c is the energy of the core state. The core state in the odd nucleus may not be identical to the excitation in the even-even nucleus, thus these relations are expected to give only a qualitative picture of the situation.

2.4 Unified model for odd-mass isotopes

The unified model of odd-mass nuclei [29] provides a description of nuclei removed from a closed shell by ± 1 nucleon. The excited states for such a nucleus include both the single-particle or hole states along with excitations of the particles or holes across the closed shell, leading to 2p-1h

or 2h-1p states. In the model, the configuration space includes these excitations coupled to the underlying collective excitations of the core. The Hamiltonian for such a system is given by

$$H = H_{core} + H_{sp} + H_{sh} + H_{p-core} + H_{h-core} + H_{ph-core} + V_{hh} + V_{pp} + V_{ph}, \tag{2.33}$$

where H_{core} refers to the excitations of the even-even core, $H_{sp,sh}$ to the particle or hole excitations, $H_{p,h,ph-core}$ to the interaction of the particle, hole, or particle-hole excitations with the core, and V to the residual h-h, p-p, or p-h interaction. The wave function for a state is then formed from the $|j_h^{-1}, X(R'); JM\rangle$ and $|j_p, Y(R); JM\rangle$ configurations, where X represents the even-even closed shell nucleus, Y represents the nucleus removed 2h from the closed shell, and R and R' denote the unique quantum numbers for a particular state. The model makes it possible to explore the constructive interference between states of single-particle and collective character. The analysis of the odd-mass isotope ^{107}In is further discussed under the framework of this model.

2.5 The interacting boson approximation

The interacting boson approximation (IBA) [30] is an algebraic and group theoretical approach to nuclear structure. The basic idea is to assume that valence nucleons outside of a closed shell couple in pairs with angular momentum $L = 0$ and $L = 2$, known as s- and d-bosons, respectively. The low-lying excited states of a nucleus are described by the interactions between the bosons. In this way, the IBA can be considered as a truncation of the shell-model space onto a bosonic subspace. Under certain conditions, it can be shown that rotational and vibrational structures arise from the basic foundations of the model. Thus the IBA provides a unique approach for generating collective properties based on microscopic assumptions.

The first version of the model is known as the IBA-1 and makes no distinction between neutrons and protons. The Hamiltonian for the various interactions between the bosons is given by

$$H = \epsilon n_d + a_o P^\dagger P + a_1 L^2 + a_2 Q^2 + a_3 T_3^2 + a_4 T_4^2, \tag{2.34}$$

where the various operators can be expressed in terms of the s- and d-boson creation and annihilation operators. Each of the terms has a corresponding physical meaning. The term n_d is the number of d-bosons, L is the angular momentum operator, P is the pairing operator, Q is the quadrupole operator, and T_3 and T_4 are the octupole and hexdecapole operators, respectively.

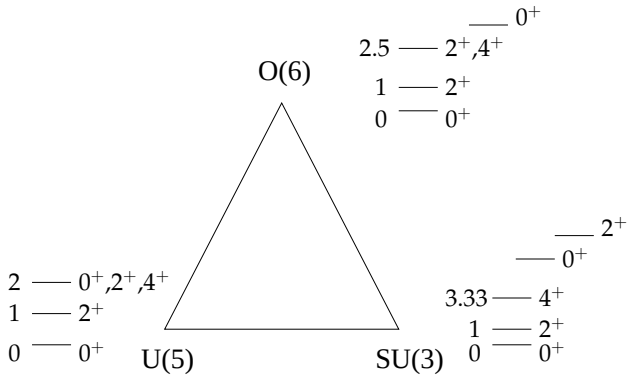

Figure 2.4: The IBA symmetry triangle. The small level schemes show the characteristic properties of the limiting dynamical symmetries. Inspired by Ref. [31].

The unique features of the IBA model are rooted in its group theoretical foundation. The magnetic substates of the d- and s-bosons can be viewed as forming a six-dimensional vector space. The group structure of the IBA can be deduced by looking for pairs of operators, which under commutation, yield linear combinations of members of the set, known as closing on commutation. It can be shown that there are 36 possible combinations which satisfy boson number conservation, called the generators of the set. This group structure is known as U(6).

Within the original 36 sets of generators there exist subgroups which close on commutation. There are three physically relevant subgroups of interest. These are U(5), SU(3), and O(6) and are known as dynamical symmetries. Each group corresponds to simplifications of the IBA Hamiltonian and can be viewed as limiting cases of the model. The Hamiltonians are given by

$$(I)U(5) \qquad H = \epsilon n_d + a_1 L^2 + a_3 T_3^2 + a_4 T_4^2, \quad (2.35)$$

$$(II)SU(3) \qquad H = a_1 L^2 + a_2 Q^2, \quad (2.36)$$

$$(III)O(6) \qquad H = a_o P^\dagger P + a_1 L^2 + a_3 T_3^2. \quad (2.37)$$

Visually, these three groups can be pictured as the apexes of a triangle representing the solutions of the IBA, as shown in Fig. 2.4. The characteristic properties of each of the dynamical symmetries are shown by the mini level schemes. The space between the three limits represents the solutions to the original Hamiltonian of Eq. 2.34.

The three groups given above correspond to ideal situations and realistic calculations require deviations from these limits. For example, consider

the SU(3) group, relevant for the Er nuclei. A SU(3) nucleus has states corresponding to the β and γ bands which are degenerate in this limit. Furthermore, the model makes some interesting predictions for the transitions between the bands. The $E2$ transitions from the γ and β bands to the ground-state band vanish while transitions between them are collective. This means that these bands, while similar to the γ- and β-vibrational bands of the collective model, have several distinctly different characteristics. Transitions between the two vibrational bands are forbidden in the collective model as they would require the destruction and creation of different types of phonons.

While no nuclei meet all the conditions of SU(3), it serves as a good starting point for describing the excited states of deformed rotational nuclei. The degeneracy of the states can be broken by including a perturbation in the direction of O(6). This should be carried out without breaking the rotational like energy spacing of the bands. The pairing term has the desired effect and plays an important role in the description of the Er nuclei within the IBA-1 framework.

Chapter 3

The Coulomb excitation method

The advantage of using Coulomb excitation as a probe of nuclear structure is the fact that the electromagnetic interaction is well understood. This makes it possible to deduce electromagnetic transition matrix elements from observed γ-ray spectra and to compare directly to predictions of nuclear models. A detailed description of the theory is outlined in Refs. [2, 32]. The discussion contained in this chapter is aimed at providing the basic theoretical and experimental foundation of the Coulomb excitation method for which the work presented in this thesis is based upon.

3.1 Theoretical overview

3.1.1 Basics

The critical experimental condition for Coulomb excitation measurements is that the interaction between a projectile and a target nucleus is purely electromagnetic. If the energy of the projectile is low enough to keep the nuclei from penetrating their mutual Coulomb barrier, then the nuclear interaction can be neglected. A conservative estimate for the maximum safe bombarding energy is given by [33]

$$E_{max}(MeV) = 1.44\frac{A_1 + A_2}{A_2}\frac{Z_1 Z_2}{1.25(A_1^{1/3} + A_2^{1/3}) + 5}, \tag{3.1}$$

where 1 stands for the projectile and 2 for the target. This formula corresponds to a minimum separation distance between the nuclear surfaces of

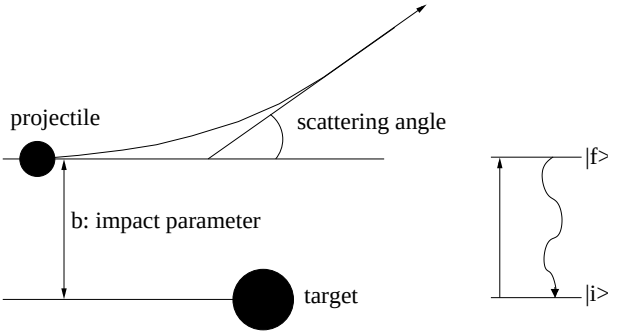

Figure 3.1: Semi-classical picture of Coulomb excitation.

$\sim$5 fm. This condition has been determined from a number of Coulomb-nuclear interference experiments as highlighted in Ref. [34] and references within. To briefly summarize, it was found that near the Coulomb barrier, the Coulomb-nuclear interference was destructive leading to sizable changes in the measured static moments of low-lying excited states. It was determined that a minimum separation distance of 5 fm was required so that the nuclear effects on the excitation cross sections were less than 0.1%.

The quantum mechanical description of the Coulomb excitation process is well known. However, most modern investigations use the simplified semi-classical approximation due to the impractical nature of calculations using the quantum mechanical formalism. In a heavy ion beam experiment, the increasing number of partial waves required quickly makes the problem insurmountable with modern day computers. Quantum calculations have been carried out for a limited number of states [35] and the development of a large-scale code based on the quantum theory can be considered one of the next goals for the theory. In addition to the ease of the application of the semi-classical approximation, it has been found to give excellent agreement, $<5\%$, with the quantum mechnical approach [34].

In the semi-classical approximation of Coulomb excitation, the nuclei are considered to obey the Rutherford scattering formula and move on hyperbolic trajectories. The transition from one nuclear state to another is however treated quantum mechanically. A figure illustrating the semi-classical framework is shown in Fig. 3.1. The application of the semi-classical formalism assumes that the energy loss to nuclear excitation and transfer of angular momentum is small, i.e. $\Delta E << E$ and $\Delta L << L$, so that the trajectories of the nuclei are not perturbed by the excitation process. ΔE and ΔL represent the difference in energy and angular momen-

tum of the initial and final states, respectively. Furthermore, the following condition must be satisfied,

$$\eta = \frac{Z_1 Z_2 e^2}{\hbar v} >> 1, \tag{3.2}$$

where v is the projectile velocity and η is known as the Sommerfeld parameter. The Sommerfeld parameter can be rewritten as $d\pi/\lambda$ where d is the distance of closest approach ($d = 2a = 2\frac{Z_1 Z_2 e^2}{m_o v^2}$) and λ is the wavelength of the projectile. The mass m_o is the reduced mass of the system. The above equation assures that the size of the projectile wavepacket is small compared to the distance of closest approach. Under these conditions the differential excitation cross section for a nuclear state is given by

$$d\sigma = P_n d\sigma_R, \tag{3.3}$$

with P_n being the probability for excitation and $d\sigma_R$ is the Rutherford scattering cross section, given by

$$d\sigma_R = 1.3 \times (\frac{Z_1 Z_2}{E_{cm}})^2 sin^{-4}(\theta/2) d\Omega \ \ [mb]. \tag{3.4}$$

The parameter $E_{cm}\ [MeV] = E_{beam}[MeV](m_t/(m_t+m_p))$ is the energy and $\theta\ [rad]$ is the scattering angle in the center of mass frame. The excitation amplitudes can be calculated by solving the Scrödinger equation, given by

$$i\hbar\frac{\partial}{\partial t}|\psi(t)\rangle = [H_o + V(t)]|\psi(t)\rangle, \tag{3.5}$$

where H_o is the free nucleus Hamiltonian for either the target or projectile and $V(t)$ is the time dependent electromagnetic field felt by the nucleus in question. The equation should be solved under the condition that the nucleus is in its ground state at $t = -\infty$. The solution using only the unperturbed term will yield a set of free nucleon eigenstates E_n and the wave functions, in Eq. 3.5, can be expanded in terms of the excitation amplitudes $a_n(t)$, given as

$$a_n(t) = \langle n|\psi\rangle exp(iE_n t/\hbar). \tag{3.6}$$

The Schrödinger equation is then equivalent to the set of differential equations, given by

$$i\hbar\frac{da_n}{dt} = \sum_m \langle n|V(t)|m\rangle e^{i(E_n - E_m t)/\hbar} a_m(t), \tag{3.7}$$

and the excitation probability is given in terms of the coefficient a_n as

$$P_n = |a_n|^2. \tag{3.8}$$

The population of a state n thus depends on the total number of nuclear states involved in the excitation. This plays an important role in Coulomb excitation experiments with heavy ions as high-lying states in collective bands may be populated. The excitation probability for a particular high-lying state may depend in a complex way on the states below. The calculation of the excitation probability amounts to solving the set of coupled differential equations in Eq. 3.7.

3.1.2 Electromagnetic interactions

The potential $V(t)$ can be expanded in terms of multipoles in the standard way and is given by

$$V(t) = \sum_{\lambda=1,\mu}^{\infty} \frac{4\pi Z_1 e}{2\lambda+1}(-1)^{\mu}\overline{S}_{\lambda\mu}(t)\mathcal{M}(\lambda,-\mu), \tag{3.9}$$

where λ is the multipole order and μ is the magnetic quantum number. The term $S_{\lambda\mu}(t)$ represents the orbital part of the interaction, which only depends on the collision parameters, and $\mathcal{M}(\lambda,-\mu)$ is the corresponding magnetic and electric multipole moment. For electric transitions the multipole moment is defined as

$$\mathcal{M}(E\lambda,\mu) = \int r^{\lambda} Y_{\lambda,\mu}\rho(\vec{r})d\tau, \tag{3.10}$$

where $Y_{\lambda,\mu}$ are the spherical harmonics, $d\tau$ is the volume element, and $\rho(\vec{r})$ is the charge density. The excitation and de-excitation of a nuclear state are both governed by the electromagnetic multipole moments and are subject to the standard angular momentum selection rule, given by

$$|I_i - I_f| \leq \lambda \leq I_i + I_f, \tag{3.11}$$

where λ is the multipolarity and $I_{i,f}$ denotes the initial and final states. The parity of the radiation field is given by

$$\pi(M\lambda) = (-1)^{\lambda+1}, \pi(E\lambda) = (-1)^{\lambda}. \tag{3.12}$$

It follows that transitions between two states which do not result in a change of parity must proceed through even electric and odd magnetic transitions while transitions between states which result in a change of parity have odd electric and even magnetic character. The exception to the rule is transitions with $\lambda = 0$ which de-excite instead through internal conversion.

3.1.3 First order perturbation theory

Forms of the total cross sections for electric and magnetic excitation can be derived using first order perturbation theory. The excitation amplitude for a single state above the ground state is given by

$$a_{I_f M_f, I_i M_i} = \frac{1}{i\hbar} \int_{-\infty}^{\infty} \langle I_f M_f | V(t) | I_i M_i \rangle e^{i(E_f - E_i)t/\hbar} dt, \tag{3.13}$$

which can be obtained from Eq. 3.7 [32]. Taking the definition of the electric multipole operator from above, making use of its properties (pg. 79 in Ref. [32]) and the Wigner-Eckert theorem, given by

$$\langle I_i M_i | \mathcal{M}(E\lambda, \mu) | I_f M_f \rangle = (-1)^{I_i - M_i} \begin{pmatrix} I_i & \lambda & I_f \\ -M_i & \mu & M_f \end{pmatrix} \langle I_i || \mathcal{M}(E\lambda) || I_f \rangle, \tag{3.14}$$

leads to

$$\begin{aligned} a_{I_f M_f, I_i M_i} = & \frac{4\pi Z_1 e}{i\hbar} \sum_{\lambda,\mu} \frac{1}{2\lambda + 1} (-1)^{I_i - M_i} \\ & \times \begin{pmatrix} I_i & \lambda & I_f \\ -M_i & \mu & M_f \end{pmatrix} \langle I_i || \mathcal{M}(E\lambda) || I_f \rangle S_{E\lambda\mu}. \end{aligned} \tag{3.15}$$

The excitation amplitude can be separated into two terms. The factor $S_{E\lambda\mu}$ contains the orbital integral and time dependence while the reduced multipole matrix element $\langle I_i || \mathcal{M}(E\lambda) || I_f \rangle$ depends on the nuclear properties. The final relation for the electric excitation cross section is given by

$$d\sigma_{E\lambda} = (\frac{Z_1 e}{\hbar v})^2 a^{-2\lambda+2} B(E\lambda) df_{E\lambda}(\theta, \xi), \tag{3.16}$$

and for magnetic excitation,

$$d\sigma_{M\lambda} = (\frac{Z_1 e}{\hbar c})^2 a^{-2\lambda+2} B(M\lambda) df_{M\lambda}(\theta, \xi), \tag{3.17}$$

where $B(\sigma\lambda)$ is the reduced transition probability (Eq. B.2 in the appendix). The functions $df(\theta, \xi)$ depend solely on the geometry of the collision and the adiabaticity parameter, defined as $\xi = a\Delta E/\hbar v$. A determination of the experimental cross section $d\sigma$ makes it possible to determine the reduced matrix elements between the initial and final states. These are model independent and can be compared to the predictions of various models.

Through comparison of Eqs. 3.16 and 3.17, it can be concluded that magnetic excitation is reduced by $\sim (v/c)^2$ compared to electric excitation. Furthermore, $E2$ transitions can be significantly enhanced due to collective

effects. For these reasons, the excitation process is predominately determined by the $E2$ transition matrix elements. Both the $E2$ and $M1$ matrix elements are however important for the de-excitation of a nuclear state.

3.1.4 γ-ray de-excitation following Coulomb excitation

The population of an excited state via Coulomb excitation is followed by the subsequent de-excitation of the state. These two processes can be treated as completely separate events as the time scale for excitation is on the order of 10^{-21}s while the lifetime is on the order of $10^{-13} - 10^{-12}$s [33]. The excitation process generally populates the nuclear states with an unequal distribution of magnetic substates and consequently the emitted γ-ray radiation exhibit a non-isotropic distribution which can be expressed by the following differential cross section [33], given by

$$\frac{d^2\sigma}{d\Omega_p d\Omega_\gamma} = \sigma_R(\theta_p) \sum_{k\kappa} R_{k\kappa}(I, I_f) Y_{k\kappa}(\theta_\gamma, \phi_\gamma), \tag{3.18}$$

where $\sigma_R(\theta_p)$ is the Rutherford cross section and $Y_{k\kappa}(\theta_\gamma \phi_\gamma)$ are the spherical harmonic functions. The equation is valid for any arbitrary coordinate frame in which the origin is centered at the de-exciting nucleus. The term $R_{k\kappa}(I, I_f)$ is given by

$$R_{k\kappa}(I, I_f) = \frac{1}{2\sqrt{\pi}\sum_\lambda |\delta_\lambda|^2} G_k \rho_{k\kappa}(I) \sum_{\lambda\lambda'} \delta_\lambda \delta^*_{\lambda'} F_k(\lambda\lambda' I_f I), \tag{3.19}$$

where the summation extends over all possible multipolarities, δ_λ is the transition amplitude, and G_k are the attenuation coefficients. The functions $F_k(\lambda\lambda' I_f I)$ are the γ-γ correlation coefficients tabulated in [36]. The polarization $\rho_{k\kappa}$ of the nuclear state is given by

$$\rho_{k\kappa}(I) = \sqrt{2I+1} \sum_{M,m} (-1)^{I-m} \begin{pmatrix} I & k & I \\ -m & \kappa & M \end{pmatrix} a^*_{Im} a_{IM}, \tag{3.20}$$

where the coefficients a are given by the excitation amplitudes. These formulas describe the angular distribution of γ rays after Coulomb excitation. When a state is fed by the de-excitation of a higher-lying state, corrections need to be introduced and the relevant expressions are given in Ref. [33]. In a typical situation, the de-excitation of an excited state proceeds predominately by both transitions of $E2$ and $M1$ character. In this case, the double differential cross section depends on the mixing ratio, defined as

$$\delta = 0.835 E_\gamma(MeV) \frac{\langle I_i || \mathcal{M}(E2) || I_f \rangle}{\langle I_i || \mathcal{M}(M1) || I_f \rangle}. \tag{3.21}$$

An overview of the theory of γ-ray angular distributions can be found in a review article by Rose and Brink [37].

3.1.5 GOSIA Coulomb excitation codes

The GOSIA suite [33] (see also a review article by D. Cline [34]) is a set of codes used to determine reduced matrix elements from observed γ-ray yields. There are two different main codes named GOSIA1 and GOSIA2. Both use a least-squares minimization routine to determine the best set of reduced matrix elements, based on the semi-classical framework, which reproduce a list of experimentally measured γ-ray yields. The main difference between the programs is that GOSIA1 is limited to the excitation of a single nucleus while GOSIA2 can handle simultaneous excitation of both target and projectile nuclei. The general procedure for both codes is based on the calculation of the excitation amplitudes and the double differential cross section for γ-ray de-excitation as described in the previous sections. After calculation of the double differential cross section, GOSIA computes the point yields, defined as

$$Y((I \rightarrow I_f), \theta_p, E) = sin(\theta_p) \int \frac{d^2\sigma}{d\Omega_p d\Omega_\gamma} d\phi_p \, [mb/srad/rad]. \qquad (3.22)$$

The double differential cross section used in this expression is not exactly the same as defined in Eq. 3.18 as several additional corrections are in addition accounted for. These include feeding from higher-lying states, the nuclear deorientation effect, solid angle factors, and transformation to the laboratory frame of reference. Reproduction of the experimentally determined yields is carried out by integrating the point yields over the finite angles of the particle detector and including energy loss in the target, leading to

$$Y_i = \int_{E_{min}}^{E_{max}} dE \frac{1}{dE/dx} \int_{\theta_{p,min}}^{\theta_{p,max}} Y((I \rightarrow I_f), \theta_p, E) d\theta_p [\frac{mb}{srad} \times \frac{mg}{cm^2}]. \quad (3.23)$$

The integration of the point yields is however a time consuming process and is only carried out periodically during the minimization. In the first iteration, the integration is performed and the experimental yields are corrected according to the ratio of the point and integrated yields. These correction factors may then be computed at any given later time. After calculation of the yields and the corrected experimental yields, the minimization process is carried out in the standard fashion through definition of the

statistic S, given by

$$S = \frac{1}{N}(S_y + S_1 + \sum_i w_i S_i), \tag{3.24}$$

where each S term represents a different set of data and N is the total number of data points. The term S_1 represents an observation limit. All γ-ray yields which exceed the upper limit contribute to the total statistic. The term S_i includes additional data to be used in the fit such as branching ratios, lifetimes, mixing ratios, and other previously known reduced matrix elements. The term S_y is given by

$$S_y = \sum_k \frac{1}{\sigma_k^2}(CY_k^{calc} - Y_e^{exp})^2, \tag{3.25}$$

where the sum should be taken over all individual γ-ray detectors used in the experiment. In the current work, the sum of all γ-ray detectors was used as input to the code rather than the individual detectors themselves, thereby defining a single detector array. The constant C is the experiment normalization factor and is the essential difference between the two GOSIA codes. The constant is fit during the minimization procedure along with the reduced matrix elements. If the system of equations is sufficiently overdetermined, then there should exist only one solution and all parameters can be uniquely determined. However, in the case of radioactive ion beam experiments with weak beam intensities, only very few transitions are usually observed and the constant can not be determined reliably. Instead, a transition in the target nucleus with a well known transition probability is used for normalization. This method is implemented in GOSIA2 and is used for the Sn experiments. In GOSIA1, the constant can be determined through normalization to other γ-ray yields, reduced matrix elements, or by comparison to the Rutherford scattering cross section. The latter is however difficult due to dead time and pile up effects.

3.1.6 Relativistic Coulomb excitation

As already mentioned previously, the key condition for a Coulomb excitation measurement is that the interaction is purely electromagnetic. In a typical low-energy experiment the projectile energy is below the Coulomb barrier and this condition is satisfied. There may however be situations where the measurements can only be carried out at energies above the Coulomb barrier. At higher energies the projectile nucleus will come closer to the target and nuclear interactions may occur. The nuclear interactions

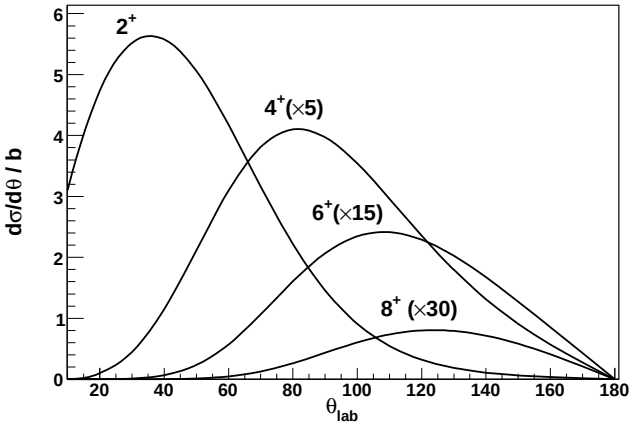

Figure 3.2: GOSIA calculated excitation cross sections for a typical rotational nucleus.

can however be neglected by considering the deflection angle of the projectile. The relation between the minimum impact parameter (see Fig. 3.1) and the deflection angle, in the center of mass frame, is given by [38, 39]

$$b_{min} = \left(\frac{Z_p Z_t e^2}{\gamma m_o v^2}\right) cot(\theta_{CM}^{max}/2), \tag{3.26}$$

where γ is the Lorentz factor. The relation shows that a larger scattering angle means a smaller impact parameter, thus bringing the two nuclei closer together. By limiting the scattering to smaller angles, the nuclear interaction can be safely ignored. Experimentally, the method may be the only means for producing certain groups of nuclei. In measurements using relativistic beams, the radioactive nuclei are produced in fragmentation reactions and separated in flight. These nuclei may not be available using the low-energy method. A review of the theoretical description of the technique is given in Ref. [40].

3.2 Experimental technique

3.2.1 Experimental considerations

The goal of a Coulomb excitation measurement is to measure the excitation cross sections of the observed states and determine the reduced matrix elements involved in the excitation. The cross sections are extracted by detecting the scattered particles in coincidence with emitted γ rays. Consider the observation of a single excited state in a nucleus. The excitation cross section is related to the number of observed γ rays by

$$N_\gamma = \epsilon_\gamma \cdot \sigma \cdot t \cdot \frac{N_A}{A} \cdot I \tag{3.27}$$

where N_γ is the number of observed coincident particle-γ rays, N_A is Avogadro's number, t is the target thickness (typically in mg/cm^2), ϵ_γ is the efficiency to detect the γ ray, σ is the excitation cross-section, and I is the intensity of the beam. The number of particle γ-ray coincidences depends crucially on the locations of the various detector positions. For example, the angular dependence of the Coulomb excitation cross section for states in a rotational band is shown in Fig. 3.2. The important angular ranges to cover differs for the different states. The experimental particle setup should be optimized to cover the most sensitive ranges of the cross sections for the states of interest.

The placement of the particle detectors also depends on the kinematics of the reaction under study. There should be good separation between the scattered target and beam particles. The kinematics for the ^{170}Er and ^{109}Sn experiments are shown in Figs. 3.3 and 3.4, respectively. In the ^{170}Er experiment, the range of the ^{32}S particles extends up to 180^o while the maximum angle for the ^{170}Er particles is 90^o. The separation in energy makes it possible to uniquely identify and Doppler correct for each detected particle during the analysis. In the Sn case, the inverse kinematics of the reaction leads to a maximum scattering angle for the Sn particles around 32^o. The bending point is useful during the data analysis as it serves as a clear energy calibration point and additional check of the scattering angles.

The measurement of the angular distribution of the emitted γ rays can also provide information on the properties of particular states. For instance, Fig. 3.5 shows a set of calculated angular distributions as a function of the Ge rings of the GASP [41] detector system, which was used in the ^{170}Er experiment and described in section 3.2.3. The angular distribution of a state at 1.702 MeV feeding a lower-lying state at 0.860 MeV, for three different spin choices of the higher-lying state, is shown as a function of the rings of the detector system. The 0^+ selection shows an isotropic behavior while the two other spin choices exhibit differing behaviors. In this way,

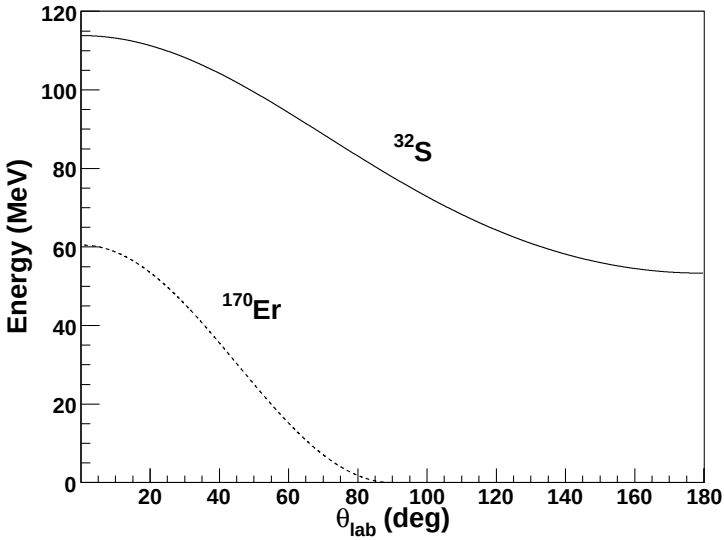

Figure 3.3: Calculated kinematics for the ^{170}Er experiment in the laboratory frame.

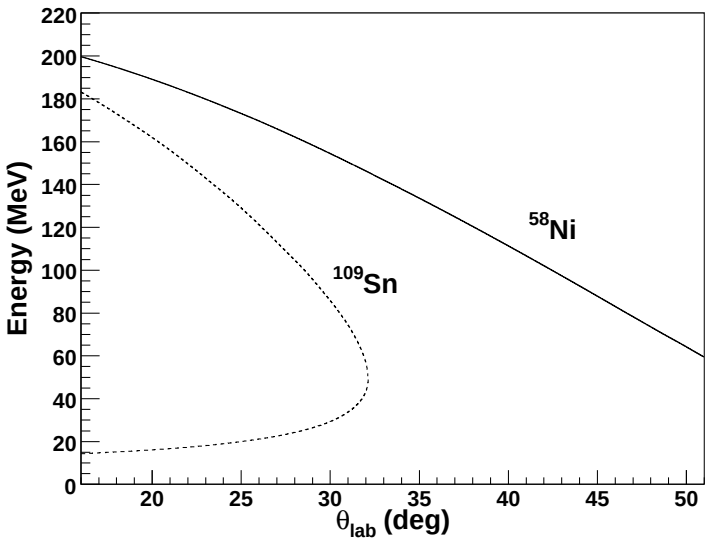

Figure 3.4: Calculated kinematics for the ^{109}Sn experiment in the laboratory frame. The calculations also account for energy loss in the target.

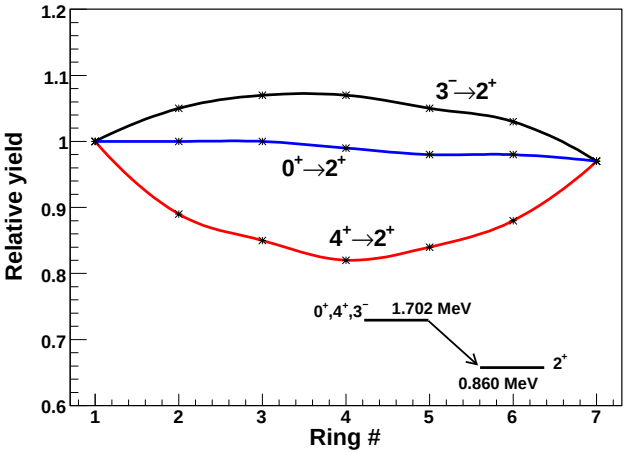

Figure 3.5: GOSIA calculated angular distributions of three different states as a function of the GASP rings of Ge detectors. The rings are placed at θ_{γ}^{lab}=[35^o,60^o,72^o,90^o,108^o ,120^o,145^o] [41]. The calculations included the experimentally measured efficiency curves from the ^{170}Er experiment.

the position of the γ-ray detectors can be placed in sensitive locations to help identify the properties of a particular state.

3.2.2 Radioactive ion beam techniques

The majority of nuclear physics studies using accelerators have involved stable targets and beams. The technology has matured to the point where high intensity beams of a large number of stable isotopes can be delivered to experimentalists. Typical beam intensities are on the order of 10^9 p/s ($\sim$ 1 pnA). The Tandem accelerator at Laboratori Nazionali di Legnaro [42] is such a facility and was used during the ^{170}Er experiment to provide a 117 MeV ^{32}S beam directed onto a 1 mg/cm^2 ^{170}Er target.

The construction of radioactive beam facilities is a much more recent development. There are basically two different methods for the production of radioactive beams in use today. The first method is known as the Isotope Separator OnLine (ISOL) method. In this technique, a high energy beam of light particles (1 GeV protons) is incident on a thick heavy target resulting in the creation of a wide variety of isotopes. Not all isotopes

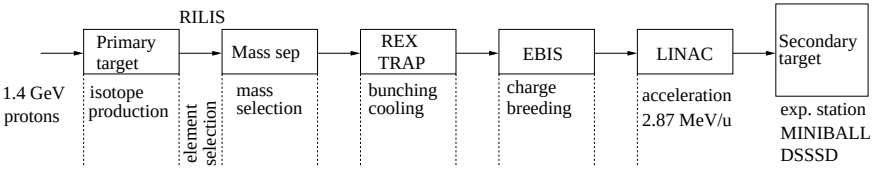

Figure 3.6: Schematic of the REX-ISOLDE facility at CERN.

created however escape the target volume. Once an element of interest diffuses out of the target, it is then extracted and delivered to an isotope separator. The isotopes are subsequently accelerated to an energy suitable for the experiment. The advantage of the ISOL technique is the high quality of radioactive beams produced and the fact that the beam energies are well known. The beam spot sizes are also quite small, on the order several millimeters.

The second method uses projectile fragmentation in a thin target to produce a wide species of isotopes. The fragments are separated in flight as they travel towards the secondary target area of the experiment. The main advantage of the technique is that all isotopes created sufficiently during fragmentation can be separated and studied. The disadvantage of the technique is that the quality of the beams is usually rather poor and the beam spot sizes can be large. The degradation of the beam is related to the amount of matter needed to slow down and separate out the isotopes of interest. The low intensity of the beams can however be compensated for by using thick secondary targets, as compared to the thickness of targets used in low-energy beam experiments. The recoiling particles must however still be able to escape the target volume.

3.2.3 Low-energy Coulomb excitation experiments

The ^{107,109}Sn experiments were carried out at the REX-ISOLDE facility [43, 44] at CERN, which is based on the ISOL concept. A schematic of the general layout of the facility is shown in Fig. 3.6. The elements were produced by bombarding a thick LaC_x target with a 1.4 GeV beam from the Proton Synchrotron (PS) booster. A typical intensity of beams from the PS booster was 3.3×10^{13} protons/pulse with between 10-20 pulses/min. After bombardment, the isotopes produced diffused out of the target and into the transfer cavity where the species of interest were singly ionized using a resonant laser ionization scheme (RILIS) [45] and delivered to the mass separator. During the transfer process from the target to the mass separa-

Table 3.1: Characteristics of radioactive beams in the Sn region produced at the REX-ISOLDE facility. Taken from Ref. [48] and the experiments presented in this thesis.

Isotope	Energy (MeV/u)	Intensity (p/s)
^{110}Sn	2.82	$\sim 10^6$
^{109}Sn	2.87	$\sim 10^5$
^{108}Sn	2.82	$\sim 10^6$
^{107}Sn	2.87	$\sim 10^5$
^{106}Sn	2.83	$\sim 10^5$
^{104}Cd	2.87	$\sim 10^5$
^{102}Cd	2.87	$\sim 10^5$
^{100}Cd	2.87	$\sim 10^3$

tor, contaminate isotopes can be singly ionized by the heated walls of the transfer tube. In the ^{107,109}Sn experiments, sizable fractions of the In isobars were extracted. The methods for determining the relative fraction of the beam components is discussed in section 4.2.4. After mass separation, the ions were transferred to REX-TRAP [46] where they were bunched, cooled, and delivered to the electron beam ion source (EBIS) [47] for charge breeding. After charge breeding, the ions underwent further separation according to their A/q ratios and were injected into the REX-linear accelerator which brought the beam energy up to 2.87 MeV/u. The intensities of typical beams using this technique for nuclei in the $A = 100$ region are shown in Table 3.1. The table shows that the neutron-deficient Sn beams are generally on the order of $10^5 - 10^6$ p/s for ^{106}Sn to ^{110}Sn. In both experiments presented in this work, the Sn and In beams were incident on a 99.93% isotopically enriched 1.95 mg/cm^2 ^{58}Ni target.

Particle detection

Both the ^{170}Er and ^{107,109}Sn experiments employed double sided silicon strip detectors (DSSSDs) for the detection of scattered beam and target nuclei. The ^{170}Er experiment was the first to make use of the Lund Silicon Strip Array (LuSiA). A picture of the setup is shown in Fig. 3.7. The detector setup consists of four DSSSDs arranged in a box like configuration around the target position at a distance of 37.5 mm from the target. The

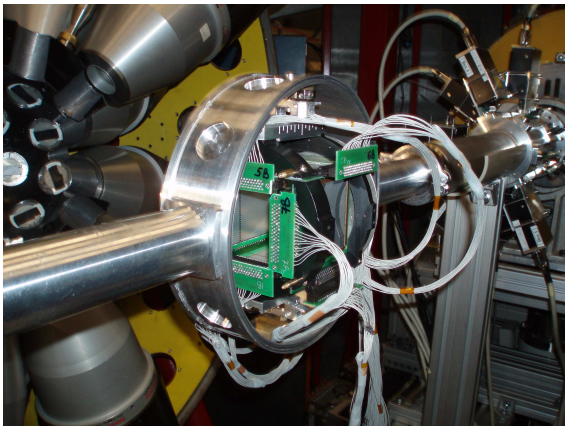

Figure 3.7: The mounted LuSiA detector setup used during the ^{170}Er experiment.

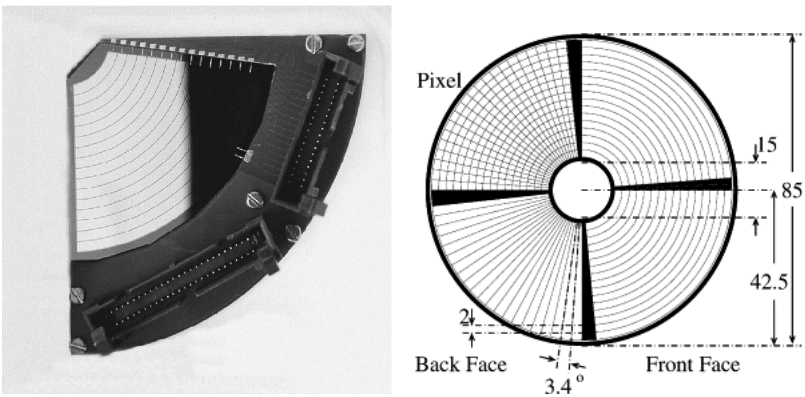

Figure 3.8: One quadrant of the DSSSD at REX-ISOLDE (left) and schematic of the DSSSD (right). The figures are reprinted from Ref. [49] with permission from Elsevier.

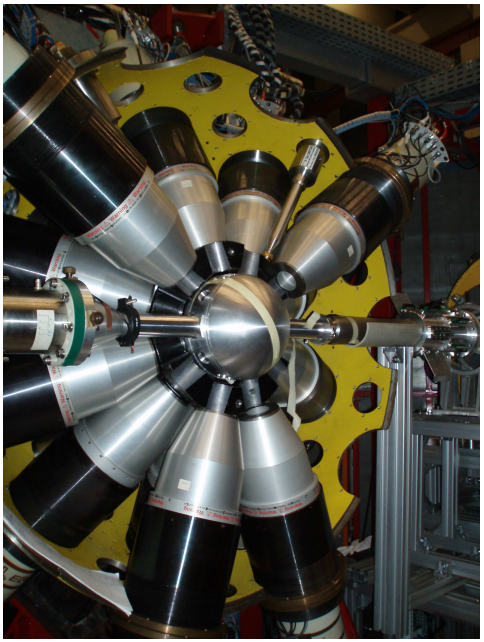

Figure 3.9: One hemisphere of the GASP detector system used for the ^{170}Er experiment.

Figure 3.10: A closeup of the MINIBALL Ge detector setup used for the Sn experiments. The figure was adapted by the author from Ref. [43].

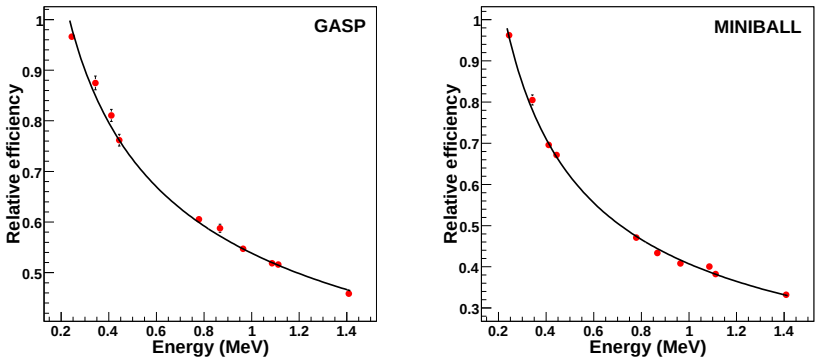

Figure 3.11: The relative efficiencies for (left) GASP and (right) MINIBALL. The calibration points are taken from [51].

setup also allows for the addition of two circular DSSSDs, each in the forward and background positions. Each 6×6 cm^2 square detector contains 32×32 strips yielding a total of 4096 channels. During the experiment, the strips were however coupled pairwise to reduce the complexity of the system. An Al foil was placed cylindrically around the target in order to stop secondary electrons created during the reaction process.

The setup at REX-ISOLDE used a single circular DSSSD [49] placed downstream of the target. The detector is shown in Fig. 3.8. The DSSSD consists of four individual detectors, represented by the four quadrants shown in Fig 3.8. Each quadrant contains 16 annual strips (front face) and 24 radial strips (back face). The back strips were coupled pairwise during the experiment. The average distance from the target to the detector has been reported to be 31(1) mm [50]. For the Sn experiments, a distance of 30.5 mm was found to give the best consistency for the data detected in the four quadrants, as described in section 4.2.2.

γ-ray detection

Modern day γ-ray detector systems consist of large clusters of Ge detectors. In low-energy beam experiments, the detectors are typically placed around the target position covering as much of the available solid angle as possible. The granularity provided by the systems is important for determining the emission angle of the γ ray with respect to the direction of the scattered beam or target particle, which is used for Doppler correction

of the energy of the emitted γ ray. The recoil velocities of the particles are on the order of $v/c \sim 0.1$, which leads to significant Doppler broadening. Since thin targets are used for these types of experiments, the scattered particles recoil into the vacuum and are detected by the DSSSDs. The measured particle energy, γ-ray energy, and the detected angles can be used to correct for the Doppler effect, using the relation given by

$$E_{\gamma}^{rest} = \gamma E_{\gamma}^{lab}(1 - \beta cos(\theta_{p\gamma}^{lab})), \tag{3.28}$$

where $\beta = v/c$ and $\gamma = 1/\sqrt{1-\beta^2}$. The angle between the particle and γ ray is defined as

$$cos(\theta_{p\gamma}^{lab}) = sin(\theta_p)sin(\theta_\gamma)cos(\phi_p - \phi_\gamma) + cos(\theta_p)cos(\theta_\gamma). \tag{3.29}$$

where p and γ denote the angles of either particles or γ rays, respectively.

The GASP detector system was used for the ^{170}Er experiment and is shown in Fig. 3.9. The array consists of 40 hyper-pure high-efficiency Ge detectors placed at a distance of 22 cm from the target position. Each Ge detector is surrounded by a BGO shield to suppress the Compton background. The array has a total efficiency of $\sim$5.8% at 1.33 MeV.

The ^{107,109}Sn experiments were carried out using the MINIBALL array [50] at the REX-ISOLDE facility. A closeup of the setup is shown in Fig. 3.10, which highlights the granularity of the system. In total, the array consists of 24 segmented Ge crystals. Each tapered crystal is 78 mm long, has a 70 mm diameter on the unshaped end [50], and is six-fold segmented in order to provide additional granularity for the Doppler correction. The efficiency of the detector system is $\sim$8% around 1 MeV (see Ref. [50]).

The measured relative efficiency curves for both detector arrays are shown in Fig. 3.11. Both arrays were calibrated using a standard ^{152}Eu source and were parametrized using the following relation

$$ln(\epsilon) = \sum_{i=0}^{N} A_i (ln(E_{keV}))^i. \tag{3.30}$$

3.2.4 Relativistic Coulomb excitation experiment

The ^{104}Sn experiment was carried out using parts of the RISING/FRS setup [52, 53] coupled to the newly developed Lund-York-Cologne CAlorimeter (LYCCA) [54] located at the Gesellschaft für Schwerionenforschung (GSI) facility [55]. The general method was presented in section 3.2.2, however a more detailed overview will be given in this section.

Radioactive ion beam production

The ^{104}Sn radioactive ion beam was produced by bombarding a 4 mg/cm^2 ^{9}Be target with a 793 MeV/u ^{124}Xe beam from the GSI linear accelerator (UNILAC) and the heavy ion synchrotron (SIS). The SIS can accelerate ions from hydrogen up to uranium to energies in the range of 1-4.5 GeV/u. The heavy ion beam is directed towards the primary target where the isotopes of interest are produced during fragmentation reactions. The process is described theoretically by the abrasion-ablation model [56], which treats the reaction as two distinct steps. The first step is the abrasion stage which occurs over a time interval of some 10^{-23} seconds. The model divides the target and projectile objects into regions consisting of participator and spectator nucleons. The participator nucleons are involved directly in the interaction while the spectator nucleons of the projectile keep moving as if undisturbed by the interaction and form what is called a prefragment. The target spectator nucleons are left essentially at rest. The second stage is the abrasion stage which occurs on the timescale of $\sim$10^{-16}-10^{-21} seconds. The excited prefragment can de-excite via a number of different channels, which may include fission, emission of particles, and/or γ rays. As mentioned before, one advantage of the technique is the large range of isotopes produced during the fragmentation process.

The fragment recoil separator (FRS)

Following the fragmentation reaction at the production target, the isotopes of interest must be individually identified and separated from the other produced isotopes. This is the primary purpose of the FRS, which is shown schematically in Fig. 3.12. The projectile fragments, resulting from the fragmentation of the production target, move with relativistic speeds in a forward focused direction. The FRS accepts the fragments and separates out the isotopes of interest using a combination of energy loss measurements with a magnetic rigidity analysis. The instrument itself consists of four separate 30^o dipole magnets, each surrounded further by quadrupole magnets, and a wedge shaped degrader at the central focal plane. The FRS is in total 74 m long. In the first section of the FRS, the two dipoles focus fragments which have equal magnetic rigidity onto the same location of the wedge-shaped degrader. The basic idea of magnetic rigidity can be shown by starting from the force exerted on a particle with mass m, charge q, and velocity v in a magnetic field, given by

$$\vec{F} = q \cdot \vec{v} \times \vec{B}. \tag{3.31}$$

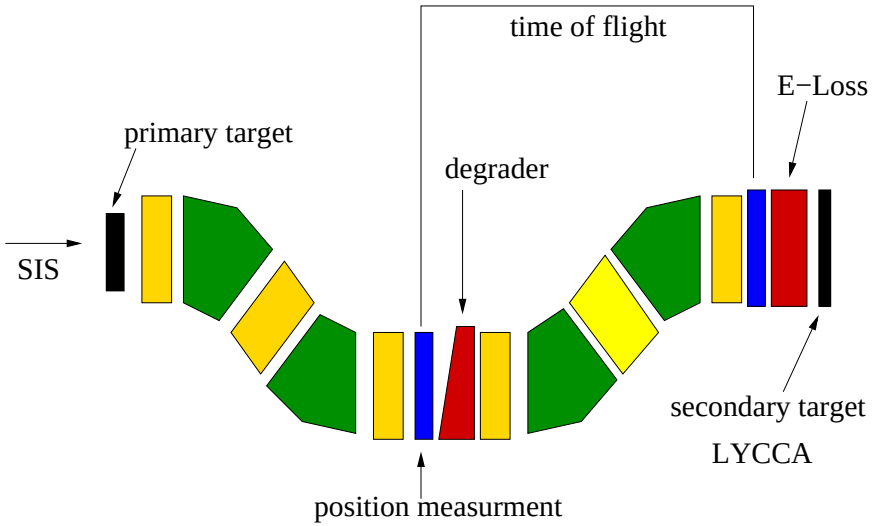

Figure 3.12: Illustration of the FRS setup. Inspired by Ref. [57].

As a fragment travels through the FRS, the resulting force from the magnetic field acts in a direction perpendicular to the fragments velocity. Treating the force as a centripetal acceleration reduces Eq. 3.31 to

$$B\rho = \frac{mv}{Ze}, \tag{3.32}$$

where ρ is the radius of motion, $m = \gamma m_o$, and q has been rewritten as Ze. The quantity $B\rho$ is known as the magnetic rigidity. The first stage of the FRS provides separation according to A/Z. During the second stage, the fragments lose energy in the wedge-shaped degrader and are further separated according to their energy loss in the material of the degrader itself.

FRS detectors

In order to identify the particles of interest, a series of detectors are located within and after the FRS setup. Energy loss detectors, known as MUltiple Sampling Ionization Chambers (MUSIC) [58], are used to determine the charge of a particular particle. A typical fill gas is CF_4. As a particle traverses the detector volume, it losses a fraction of energy proportional to its

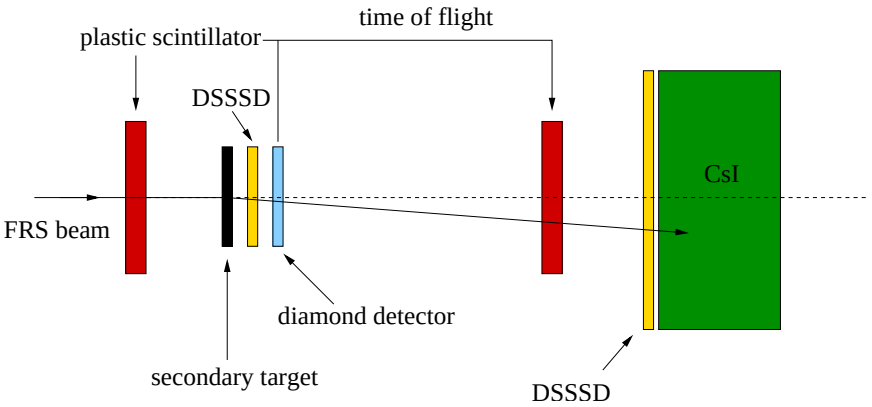

Figure 3.13: Illustration of the LYCCA setup.

charge and velocity, as given by the Bethe-Bloch formula,

$$-\frac{dE}{dx} = Z^2 \cdot F(\beta), \tag{3.33}$$

where $\beta = v/c$. The factor $F(\beta)$ is dependent only on the velocity of the ion. The velocity information is provided by time-of-flight detectors. These are either plastic scintillators or a finger detector, which is a segmented plastic scintillator. The signals from these detectors not only provide time-of-flight-information but also give the interaction position of a particle at the location of a detector. Lastly, time projection chambers (TPCs) provide further data on the positions of the fragments. The measured positions are used to correct the magnetic rigidity as most particle trajectories do not lie on the beam optical axis. This information, along with the measured energy loss, is used to determine the A/q ratios of the particles of interest.

LYCCA detectors

After separation and identification of the particles, the beam is directed onto a secondary target where Coulomb excitation takes place. A ^{197}Au target was used for the ^{104}Sn experiment. The target and projectile particles, after interacting in the target, are detected using the LYCCA detector setup, shown schematically in Fig. 3.13. The setup consists of a wall of DSSSDs for energy loss measurements followed by CsI scintillators for total energy measurements. Furthermore, fast plastic scintillators [59] or

large area polycrystalline diamond detectors [60] provide time-of-flight information. A single DSSSD placed near the secondary target is used to measure the x and y coordinates of the interaction at the target. These data, combined with the x and y coordinates determined from the TPCs placed upstream of the secondary target, are used to determine the incoming velocity vector of a particle. The DSSSDs in the DSSSD-CsI wall and the target position can be used to calculate the outgoing vector of a particle in order to determine the scattering angle.

Chapter 4

Experiments near ^{100}Sn

4.1 Introduction

The nuclei near the doubly magic nucleus ^{100}Sn are an important testing ground for theoretical models. The Sn nuclei, which have 50 protons, can to a first approximation be described by the excitations and interactions of the neutrons above $N = 50$. The first excited states of the even-even Sn nuclei, shown in the left panel of Fig. 1.2, exhibit a nearly constant behavior across the isotopic chain. This feature can be explained by the well known behavior that nucleons tend to pair in groups of two. The first excited states correspond to the recoupling of the angular momenta of one of the neutron pairs. This leads to a nearly constant energy which is also well reproduced by calculations. The reduced transition probabilities for these nuclei are shown in the right panel of Fig. 1.2. On the neutron rich side of the shell, the shell-model calculations are in good agreement with the experimentally measured values. On the neutron deficient side, recent measurements have shown that the transition probabilities are enhanced with respect to calculations. This could possibility indicate the importance of proton and/or neutron excitations across the $N = Z = 50$ shell gap. It is also interesting to see if this trend extends to the odd-Sn nuclei.

Another physics investigation in the same region is related to the single-neutron states just above ^{100}Sn. The states are important ingredients for shell-model calculations. No information outside of the energy splitting between the two lowest-lying states, measured to be 172 keV [4, 5], is known at this time. The spin ordering of the two states is also highly debated. An alternative method to locating the positions of the single-neutron states in ^{101}Sn is to study the migration of these states across the Sn isotopic chain, as shown in Fig. 1.1. This has been carried out down

to ^{109}Sn, where the assignments for the five states above $N = 50$ are still preliminary. One of the main motivations for the ^{107,109}Sn experiments was to confirm the positions of these states in ^{109}Sn and to identify them in ^{107}Sn. It is also interesting to see if the reduced transition probabilities in these nuclei are enhanced with respect to shell-model calculations, as found in the above mentioned even-even nuclei. To a first approximation, low-lying excited states in the odd-Sn nuclei can be considered as arising from the coupling of a single neutron to an underlying even-even core. Under this assumption, it could be expected that the low-lying states of these nuclei would likewise also be enhanced.

In the ^{107}Sn experiment, it was also possible to extract information for the isobaric beam contaminant ^{107}In. Experimental studies in the In nuclei can provide important information on the proton-neutron interaction near the doubly magic nucleus ^{100}Sn. The lowest-lying excitations in these nuclei can be approximately described by the excitations of the proton hole relative to the $Z = 50$ shell closure coupled to collective excitations of the underlying core. This chapter is based on the work presented in Papers I, II, and III; for ^{107}Sn, ^{109}Sn, and ^{107}In, respectively.

4.2 The ^{107,109}Sn experiments

The Coulomb excitation experiments of ^{107}Sn and ^{109}Sn were performed at the REX-ISOLDE facility at CERN. The setup used during the experiments is described in Ch. 3. Both experiments used a 2.87 MeV/u Sn beam incident on a 99.93% isotopically enriched ^{58}Ni target. The experiments were analyzed using the same set of methods and software programs, which are described in this section.

4.2.1 Data acquisition

Electronics

A detailed overview of the electronics used at MINIBALL during the experiments can be found in Ref. [61] and a recent review article [50]. However, a short overview is presented here. For a single MINIBALL Ge detector, the preamplifer signals from the six segments and core are digitized by DGF-4C modules [62]. Two modules are used for the core and segment signals per detector. The core signal is stored in channel zero of the first module while the remaining signals are stored in the other channels of the two modules, leaving one channel free. All the modules are synchronized

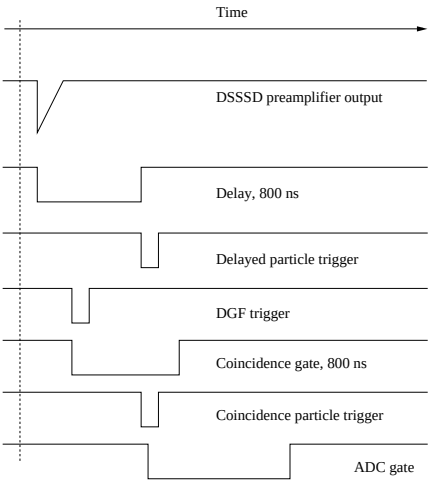

Figure 4.1: The coincidence scheme for γ rays and particles (see also Ref. [50]).

to an external 40 MHz clock for time stamping purposes. In order to avoid dead time effects, the DGF-4Cs are only read out once at the end of a beam spill. For this reason, the external clock is needed in order to correlate γ-ray and particle events.

The signals from the DSSSDs are first processed by Edinburgh/RAL charge sensitive preamplifers and further by Edinburgh/RAL shaping and discriminator amplifiers [63, 64, 65]. The time signals for each quadrant of the DSSSD are read out using CAEN V775 TDCs [66] while the energy signals are read out using mesytec MADC32 modules [67]. The mesytec modules are also synchronized with the common clock used as time reference for the DGF-4Cs.

Coincidence condition

The coincidence scheme used during the experiments is shown in Fig. 4.1. The raw timing signals from the DSSSD are used to generate an 800 ns delayed particle trigger. The delay is necessary as the DGF-4Cs produce a trigger about 500 ns after a γ ray interacts within the crystal volume of a Ge detector. Each γ ray creates an 800 ns coincidence window. If the delayed particle trigger falls within this window, a coincident particle gate trigger is generated which opens the ADC gate and timestamps the rele-

vant particle and γ-ray event. If the particle trigger does not lie within the 800 ns coincidence window, then only one in 2^n triggers are accepted. The downscaled mode is used in order to limit dead time effects arising from particles scattered elastically from the target.

Data format and event building

The data acquisition for the experiment used the MARaBOU [68] system. The format of the stored data is of the MBS Event Data (MED) type [69, 70]. A program was developed for the work presented here based on the mbs2asc software available in Ref. [68]. In its downloadable form, the software reads the MED event buffers and displays them in ASCII representation. The software was modified to dump the information into ROOT [71] trees, making the data suitable for further analysis. At this point, the ROOT trees contained only the raw signals acquired from the experiment. The data was then processed by a series of programs. The main difference between the programs developed for the ^{107,109}Sn and ^{170}Er experiments is related to the particle and γ-ray time matching. In the ^{170}Er experiment, discussed in the following chapter, a particle-γ-ray coincidence was used as the main trigger and all buffers contained at least one of each type of particle. In the Sn experiments, the particle and γ-ray events were stored in separate MED buffers and had to be correlated based on the common time reference. The following sections discuss in detail the analysis procedure.

4.2.2 Particle data

After unpacking the raw data into ROOT trees, the data was processed by a particle construction routine. Each particle was constructed from events which produced TDC/ADC signals in a single front and back strip of the DSSSD for quadrants Q2, Q3, and Q4. An event was accepted if the signals were in the same channels of the ADC and TDC. The TDC signals for Q1 were however not available during the experiments and instead an energy threshold method was used. Events were created only if the single front and back strips produced signals above a threshold. The method was tested against the TDC/ADC matching method and was found to give an average agreement of 97%.

The particle data was divided into two types of events. Those in which only one of the Sn or Ni particles was detected (1p) and those in which both particles were detected (2p). For the 2p events, it was further required that the particles were scattered into quadrants at 180^o with respect to each

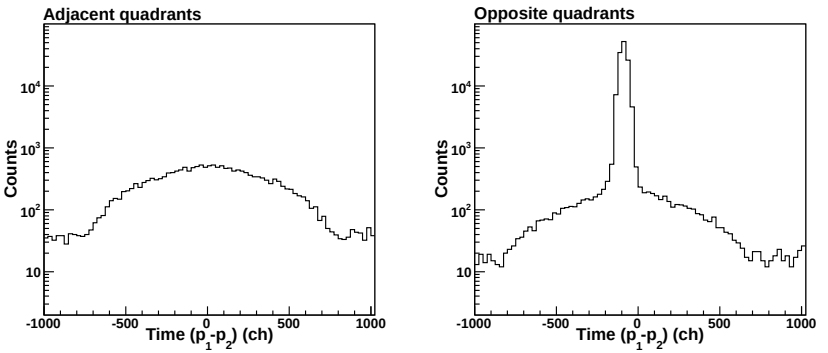

Figure 4.2: Time difference coincidence spectra for adjacent and opposite quadrants of the DSSSD.

other. The time stamped difference between these type of events is shown in Fig. 4.2. The plot on the left shows the spectrum for particles scattered into adjacent quadrants, which exhibits a rather featureless structure. The plot on the right shows a large prompt peak indicating the detection of two coincident events. The events within the prompt peak were used for further analysis. 1p events may have also occurred in the same angular region as the 2p events, as dead time effects in the ADC and TDC modules of the DSSSD may have resulted in the detection of only a single particle.

The collected energy versus scattering angle plots for the two experiments are shown in Figs. 4.3 and 4.4. The spectra were energy calibrated using the known energy loss in the target. The angles were calibrated using the distance of the DSSSD from the target position. It was found that the beam spot position corresponded to x=-0.12 mm and y=-1.49 mm for the ^{109}Sn experiment and x=1.68 mm and y=-1.86 mm for the ^{107}Sn experiment. The positions were deduced based on the 2p events detected in the DSSSD. The distance from the target has been given in Ch. 3 to be 31(1) mm. However, this distance did not yield a consistent position of the maximum scattering angle in the four quadrants. A distance of 30.5 mm, within the quoted uncertainty, was found to give good agreement in all four quadrants of the detector. The kinematical cuts used in the data analysis are indicated in the plots. It can also be mentioned that two strips of the DSSSD were not functioning properly. One strip in Q3 and one in Q4 was broken. The effects of the missing strips were estimated based on the quadrants with working strips and found to have no significant impact on the results.

4.2.3 Particle-γ-ray coincidence data

The suitable events for the Coulomb excitation analysis were further selected based on the particle-γ-ray coincidence spectrum. An example is shown for the 2p events in one of the quadrants in Fig. 4.5, collected from the ^{109}Sn experiment. The prompt events are indicated by the blue cut, which was typically about 150 ns wide. The cut was set separately for both the 1p and 2p events and for each individual quadrant of the DSSSD. The red region marks the area selected for background subtraction in the ^{109}Sn experiment. No background subtraction was carried out for the ^{107}Sn experiment.

4.2.4 Isobaric beam contamination

The radioactive beams during both experiments contained some fraction of the isobaric contaminants ^{107,109}In. As these isotopes also produced additional excitations in the target, it was important to monitor the purity of the beam to provide the proper normalization for the transition probabilities of the Sn nuclei. The purity was monitored by turning the laser ionization on and off at different intervals throughout the experiments. For the ^{107}Sn experiment, two intervals were used at different points during the experiment. First, laser on/off measurements were taken for one hour every three hours. After some time, it was instead decided to run continuously in laser on/off mode. In the ^{109}Sn experiment, the purity was monitored using the laser on/off method for one hour every three hours. A time averaged purity was then deduced for each experiment based on these measurements.

The purity of the beam for the ^{107}Sn experiment, when the laser ionization was switched on, was determined by observing the number of scattered particles and ^{107}In γ rays collected during the laser on and off periods. The beam purity during the laser on runs is related to the number of scattered particles by

$$P(ON) = \frac{N_p^{Tot}(ON) - N_p^{In}(ON)}{N_p^{Tot}(ON)} = 1 - \frac{N_p^{In}(ON)}{N_p^{Tot}(ON)}, \qquad (4.1)$$

where $Tot = Sn + In$, p corresponds to particles, and $P(ON)$ represents the beam purity during the laser on runs. Only the number of total particles is measured during a laser on run. The number of In particles can be calculated from the the observed γ-ray yields. The number of γ rays from

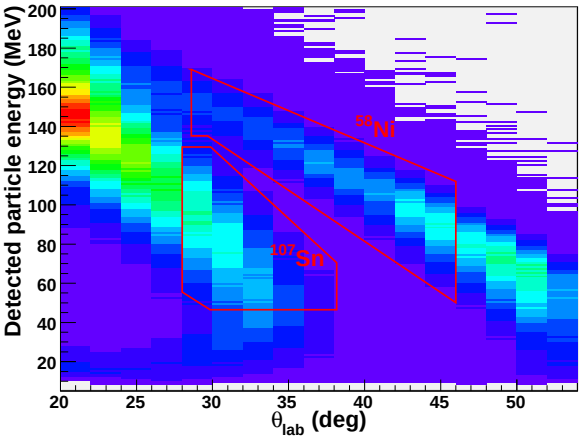

Figure 4.3: Measured energy versus laboratory scattering angle for the ^{107}Sn experiment. The markers show the regions used in the analysis.

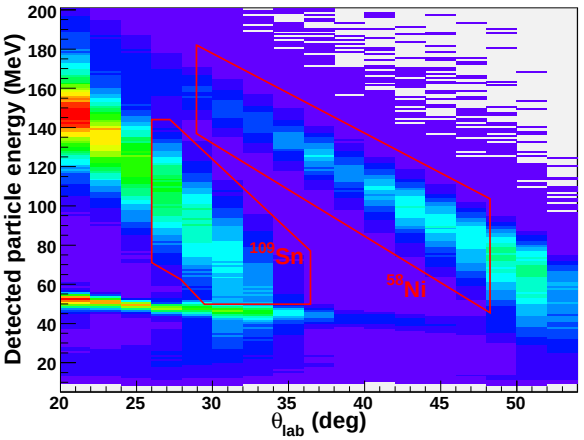

Figure 4.4: Measured energy versus laboratory scattering angle for the ^{109}Sn experiment. The markers show the regions used in the analysis. The branch at lower energies is likely Ne, as Ne gas is used in REXTRAP. Isotopes with similar A/q ratios as the beam of interest cannot be removed by the REX mass separator (see also Ref. [43]).

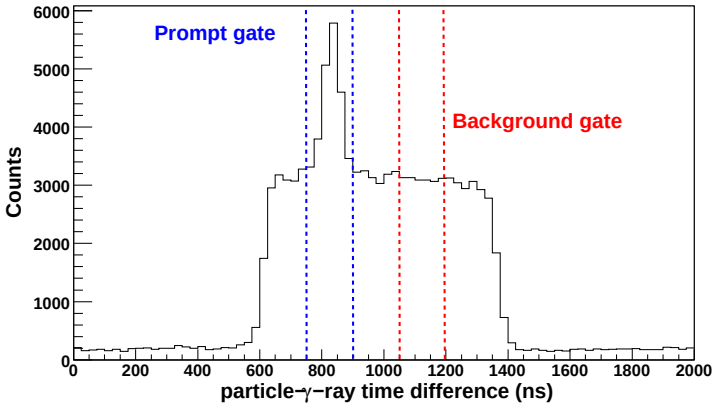

Figure 4.5: Particle-γ-ray coincidence spectrum for 2p events for one of the quadrants during the ^{109}Sn experiment.

the In isobar during a laser on run is related to the number of scattered particles by

$$N_{\gamma}^{In}(ON) = N_{p}^{In}(ON) \times \sigma, \tag{4.2}$$

where σ is proportional to the Coulomb excitation cross section. Likewise, the number of γ rays during a laser off period is given by

$$N_{\gamma}^{In}(OFF) = N_{p}^{In}(OFF) \times \sigma. \tag{4.3}$$

Since the proportionality factor is the same in both cases, Eq. 4.1 can be rewritten as

$$P(ON) = 1 - \frac{N_{p}^{In}(OFF) \cdot N_{\gamma}^{In}(ON)}{N_{p}^{Tot}(ON) \cdot N_{\gamma}^{In}(OFF)}. \tag{4.4}$$

Using this method, the calculated $P(ON)$ for the ^{107}Sn experiment was found to be 31(6)%. The method provides a means for calculating the contamination during the laser on runs, as the beam purity is really only known during the laser on/off runs.

No Coulomb excitation of the ^{109}In isobar was observed in the ^{109}Sn experiment. Instead, the beam purity was deduced from the scattered particles collected during the laser on and off runs [72]. The beam purity was calculated to be 89(1)%.

Table 4.1: Measured yields and relative intensities from the ^{107}Sn and ^{109}Sn experiments (Papers I and II, respectively) . Energies given in Ref. [73, 74, 75, 76].

	^{109}Sn exp. (Figs. 4.6, 4.7)		
$I_i \rightarrow I_f$	E_γ (keV)	Yield	I_γ
$3/2_1^+ \rightarrow 5/2_1^+$	665	462(40)	0.82(8)
/ $5/2_2^+ \rightarrow 7/2_1^+$	664		
$5/2_2^+ \rightarrow 5/2_1^+$	678	60(31)	0.11(6)
$3/2_2^+ \rightarrow 5/2_1^+$	925	277(32)	0.60(7)
$1/2_2^+ \rightarrow 5/2_1^+$	991	99(26)	0.22(6)
$7/2_2^+ \rightarrow 5/2_1^+$	1078	390(37)[a]	0.93(10)[a]
/ $7/2_2^+ \rightarrow 7/2_1^+$	1064		
$9/2_1^+ \rightarrow 5/2_1^+$	1240	278(27)	0.72(8)
Ni $2^+ \rightarrow 0^+$	1454	350(30)[b]	1.00(9)[b]
	^{107}Sn exp. (Figs. 4.8, 4.9)		
$3/2_1^+ \rightarrow 5/2_1^+$	704	140(20)	1.92(28)
$5/2_2^+ \rightarrow 7/2_1^+$	667	<71	<0.94
$9/2_1^+ \rightarrow 5/2_1^+$	1222	<66	<1.27
Ni $2^+ \rightarrow 0^+$	1454	47(11)[b]	1.00(24)[b]

[a] $3/2_3^+ \rightarrow 5/2_1^+$ transition at 1062 keV may also be present.
[b] The yield and intensity were calculated with the observed ^{58}Ni yield combined with the purity of the radioactive beam.

4.2.5 Experimental results

The measured peak areas and intensities are shown in Table 4.1. The collected spectra from the two experiments are shown in Figs. 4.6 - 4.9 and the previously known experimental level schemes are given in Fig. 4.10, labeled as Exp.

The ^{107}Sn experiment

In Fig. 4.8 the ^{58}Ni 2^+ state at 1454 keV is clearly visible after Doppler correction [73]. In the ^{107}Sn spectrum, the peak at 704 keV corresponds to the $3/2_1^+ \rightarrow 5/2_1^+$ transition while the peak at 1001 keV is related to the isobaric beam contaminant ^{107}In [74]. The peak is still observed when the laser ionization is turned off in the analysis, as shown in Fig. 4.11,

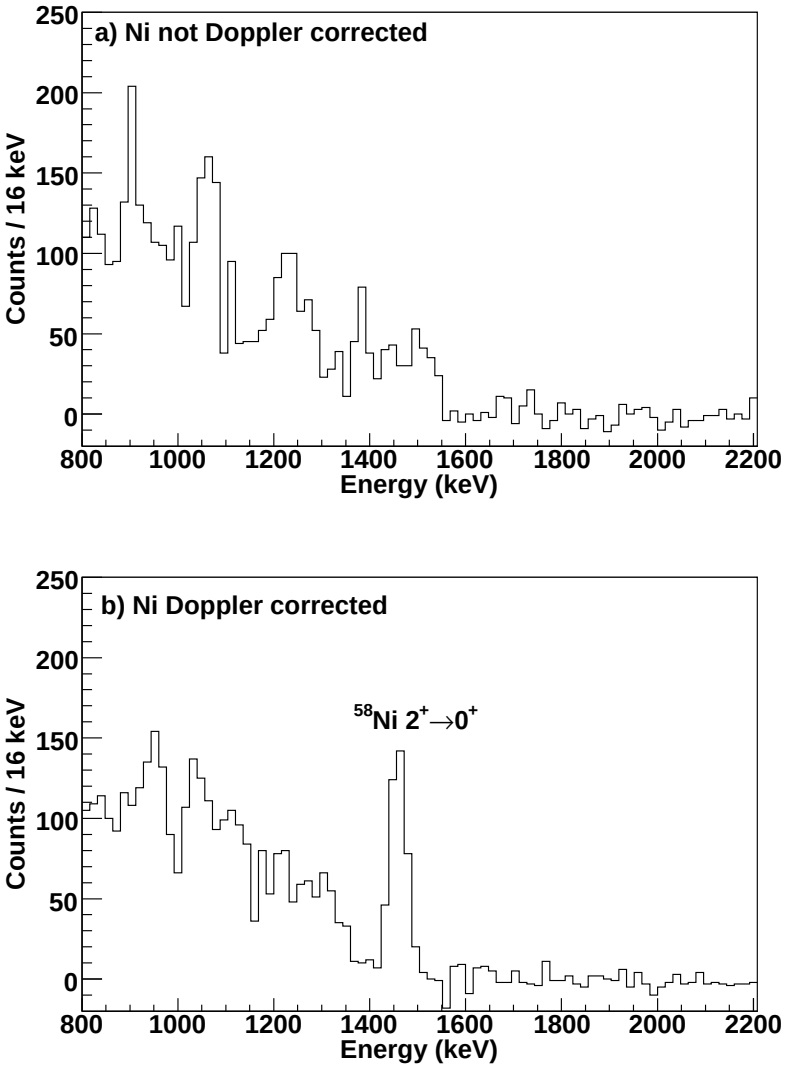

Figure 4.6: The raw and Doppler corrected γ-ray spectrum gated on ^{58}Ni for the ^{109}Sn experiment.

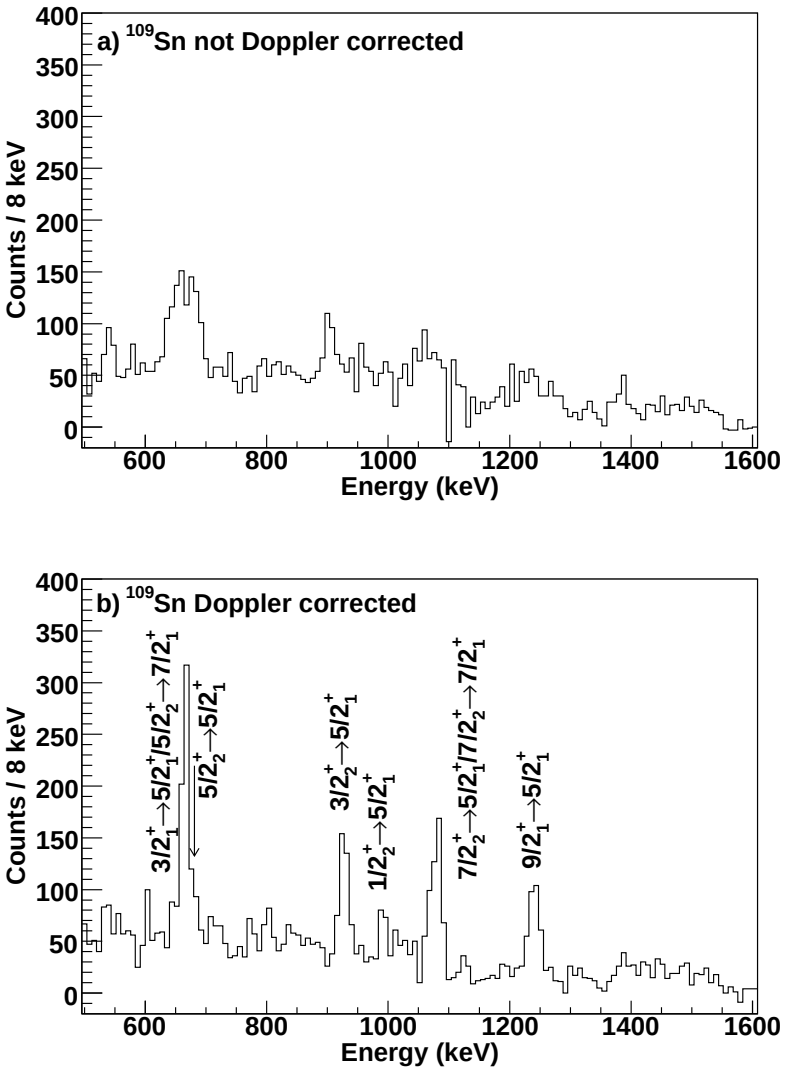

Figure 4.7: The raw and Doppler corrected γ-ray spectrum gated on ^{109}Sn for the ^{109}Sn experiment.

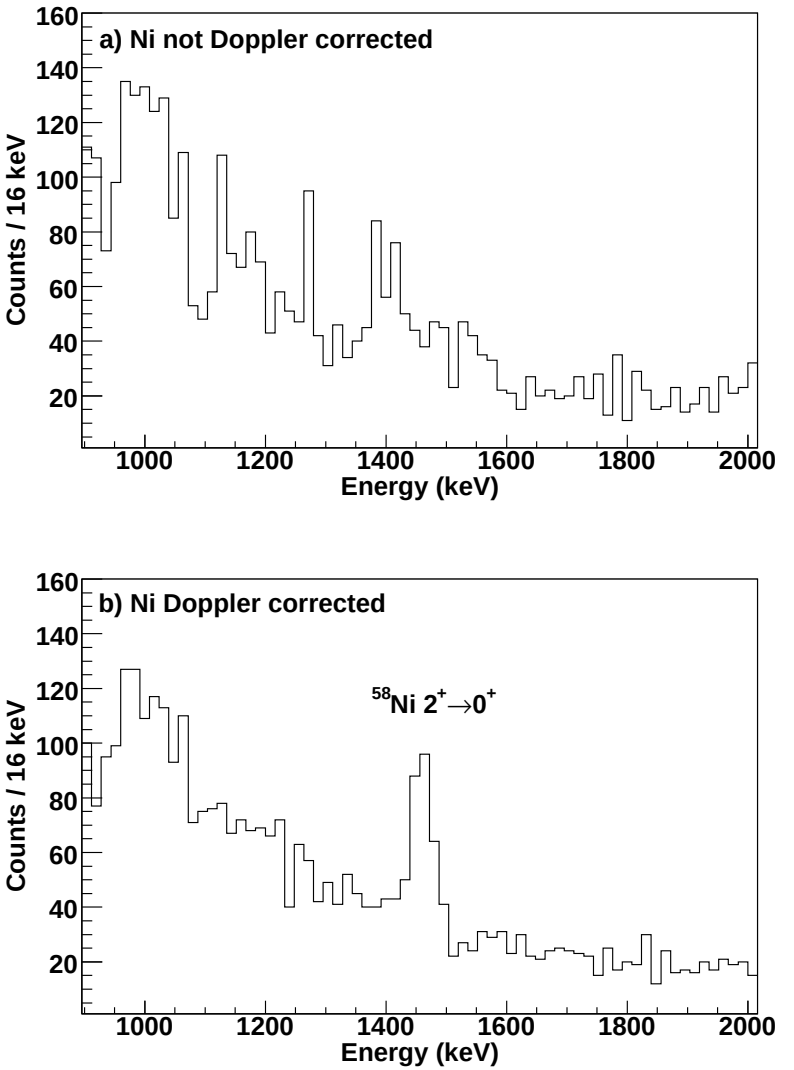

Figure 4.8: The raw and Doppler corrected γ-ray spectrum gated on ^{58}Ni for the ^{107}Sn experiment.

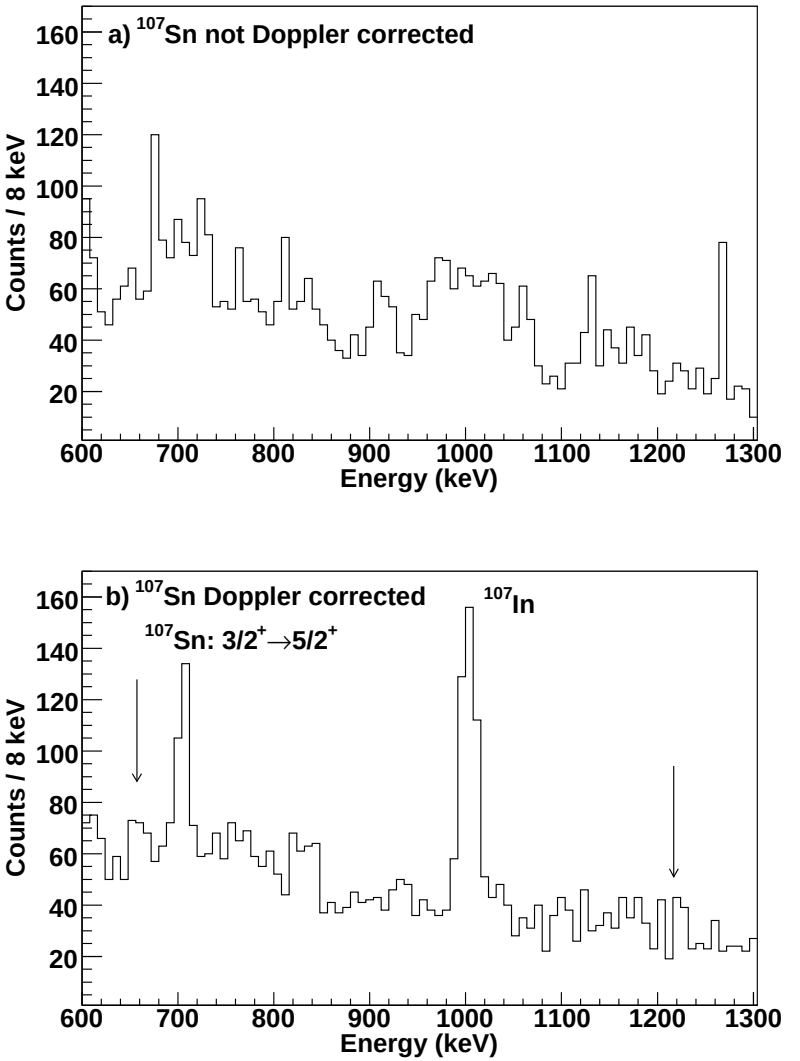

Figure 4.9: The raw and Doppler corrected γ-ray spectrum gated on ^{107}Sn for the ^{107}Sn experiment. The arrows mark the possible weak presence of two other decays from ^{107}Sn.

indicating that it is not a transition belonging to the nucleus ^{107}Sn. There is a weak indication of the $5/2^+_2 \rightarrow 7/2^+_1$ and $9/2^+_1 \rightarrow 5/2^+_1$ transitions at 667 keV and 1222 keV, respectively. Two other low-lying $3/2^+$ states have been observed previously in ^{107}Sn, at 1280 keV and 1454 keV, and one possible $3/2^+$ state at 970 keV [75]. However, none of these were populated with significant intensity in the experiment. The known level scheme of ^{107}Sn is shown in the far left side of Fig. 4.10. The level scheme is compared to shell-model calculations described in detail later in this chapter.

The ^{109}Sn experiment

The measured γ-ray spectrum, gated on ^{109}Sn, is shown in Fig. 4.7 and the experimentally known level scheme is shown on the right side of Fig. 4.10. As oppose to the ^{107}Sn experiment, where only one transition was clearly observed, several previously known transitions can be identified in the ^{109}Sn spectrum and include the following: the doublet at 664 keV, corresponding to the $3/2^+_1 \rightarrow 5/2^+_1$ and $5/2^+_2 \rightarrow 7/2^+_1$ transitions; a hint of the nearby 678 KeV $5/2^+_2 \rightarrow 5/2^+_1$ transition; the $3/2^+_2$ state at 925 keV; the $1/2^+_2$ state at 991 keV; a structure around 1078 keV possibly containing contributions from the 1062 keV $3/2^+_3 \rightarrow 5/2^+_1$, 1064 keV $7/2^+_2 \rightarrow 7/2^+_1$, and 1078 keV $7/2^+_2 \rightarrow 5/2^+_1$ transitions; and finally the $9/2^+_1$ state at 1240 keV [75, 76]. Only transitions connecting to the $5/2^+$ ground state and the $7/2^+$ first excited state were observed with significant intensity in the experiment. These states are only separated in energy by 14 keV. The proposed single-neutron $s_{1/2}$ state at 545 keV was not observed [75]. Interestingly however, the $3/2^+_2$ state has been suggested to be the single-neutron $d_{3/2}$ state and it is clearly seen in the spectrum. This indicates that the state may be partially based on a collective excitation, as further discussed in section 4.2.9. For the analysis of the data, the structure around 1078 keV was attributed to transitions from the 1078 keV state, based on the branching ratio data given in Ref. [77].

4.2.6 Reduced matrix elements and error analysis

The measured yields from the ^{107,109}Sn experiments were analyzed using the Coulomb excitation code GOSIA2. In both experiments a ^{58}Ni target was used for normalization. The adopted Ni reduced matrix elements, used in the analysis, are given in Table 4.2. The extracted $B(E2)$ values from the analysis of the data are given in Table 4.3. The details for each case and the error analysis procedures are discussed in the following.

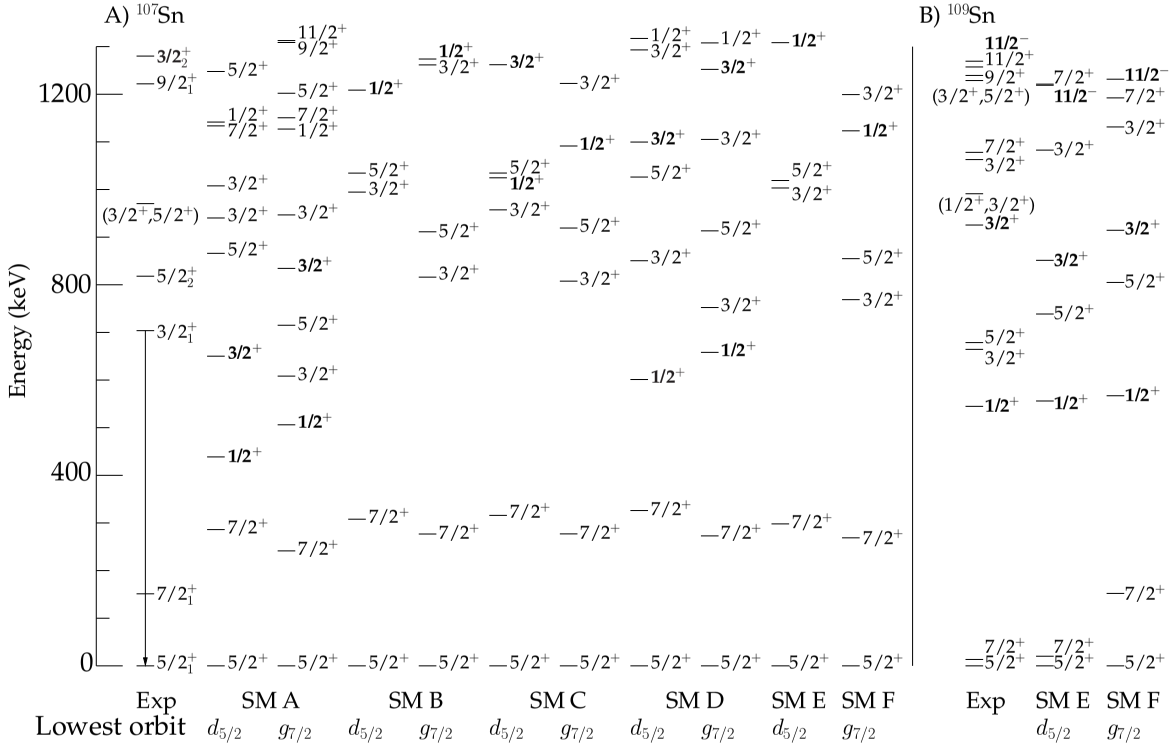

Figure 4.10: The known levels schemes (Exp) of A) ^{107}Sn and B) ^{109}Sn. The arrow marks the observed γ ray in the ^{107}Sn experiment. The shell-model calculations described in the text are given for comparison where the bold labels mark the single-neutron states. The calculations correspond to the single-neutron energies given in Table 4.4. Figure taken from Paper I.

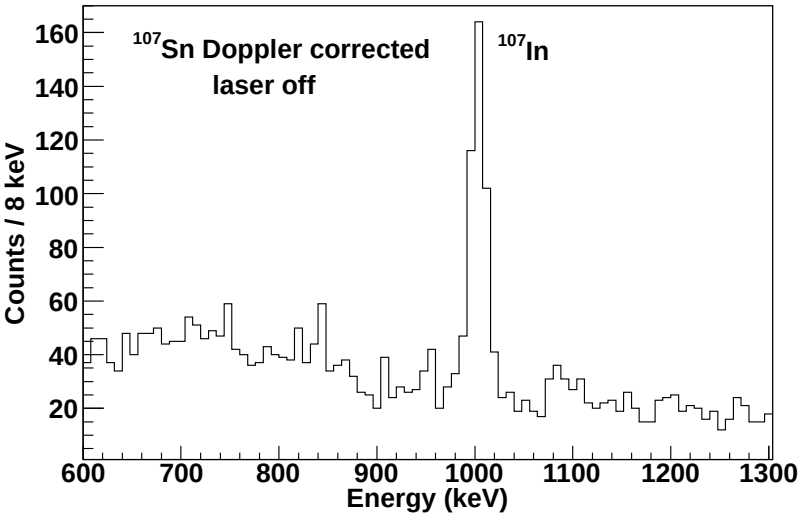

Figure 4.11: The Doppler corrected spectrum for the ^{107}Sn experiment with the laser ionization turned off. Only the peak at 1001 keV remains.

Table 4.2: The Ni reduced matrix elements used in the analysis of the Sn experiments, taken from Ref. [73].

Level	Energy (keV)	I^π	1	2	3	4
1	0.0	0^+	0.0	0.2653(28)	0.0	0.0139(24)
2	1454.2	2^+		-0.1319(792)	0.3666(196)	0.3163(528)
3	2459.2	4^+			0.0	0.0
4	2775.4	2^+				0.0

The ^{107}Sn experiment

In the analysis of the ^{107}Sn data, although only the $3/2_1^+$ state was observed, several states were included to account for any unobserved excitation. The additional states were the $7/2_1^+$, $5/2_2^+$, and the $9/2_1^+$ states at 151 keV, 818 keV, and 1222 keV, respectively. In addition to these, a shell-model predicted 1400 keV $7/2^+$ state was also included. All possible $E2$

and $M1$ reduced matrix elements coupling these states were defined in the input. The starting values were taken from shell-model calculations (SM F), described in section 4.2.7. During the fitting procedure the $M1$ reduced matrix elements and quadrupole moments of all states were fixed. Only the $E2$ reduced matrix elements of the observed states were allowed to vary. The previously known γ-ray branching ratios for the 704 keV and 818 keV states [74] were also included as constraints in the analysis.

While GOSIA2 contains an error estimation routine, it does not include target and projectile reduced matrix element correlations. The error was estimated by using a $\chi^2 + 1$ technique, where the $3/2_1^+$ reduced matrix element was fixed at different points around the determined minimum value. The $\pm\sigma$ limits of the $B(E2)$ value correspond to the χ^2 parameter plus or minus one [78]. The minimization was then repeated by releasing the ^{58}Ni target reduced matrix elements and the ^{107}Sn reduced matrix elements related to the two branching ratios defined in the analysis. At each additional point for the $3/2_1^+$ reduced matrix element, the χ^2 value was calculated. The errors in Table 4.3 correspond to the $\chi^2 + 1$ limits.

The influence of the other fixed ^{107}Sn reduced matrix elements was investigated using several different methods. First, the minimization was repeated by fixing all the values to $\pm 50\%$ their shell-model calculated values. The test is similar to previously used methods for estimating errors using GOSIA [79]. The $3/2_1^+$ value was only effected by a maximum of 0.003 e^2b^2. An effect of the same magnitude was observed when all the other reduced matrix elements were set to zero. As the ordering of the two lowest-lying orbits relative to ^{100}Sn is still uncertain, the SM E values (section 4.2.7) were also tested as initial starting values for the reduced matrix elements. The influence on the $3/2_1^+$ reduced matrix element was less than 0.001 e^2b^2. Lastly, an additional fit was carried out where yields corresponding to the maximum values of the two observed upper limits were input to the code. Again, this had only a small influence on the order of 0.002 e^2b^2. The effects of the above tests are all small when compared to the uncertainty for the $3/2_1^+$ state given in the table.

The ^{109}Sn experiment

The analysis of the ^{109}Sn data was similar to that of ^{107}Sn. Ten states were defined in the input to the code, including all possible $E2$ and $M1$ reduced matrix elements. They were taken from the SM 109 calculations (section 4.2.7). In addition, the analysis included the following data points: the measured quadrupole moment for the ground state from hyperfine measurements [80] and nine previously known branching ratios [75, 76]. In total, fifteen reduced matrix elements were fit to fifteen data points.

Table 4.3: The measured $B(E2)$ values from the ^{107}Sn and ^{109}Sn experiments (Papers I and II, respectively). The core-excitation calculations (CE) were carried out using a ^{108}Sn core, $B(E2) = 0.222(19)e^2b^2$ [9]. The shell-model (SM) value for ^{107}Sn was taken from the SM F calculations. The values for ^{109}Sn were taken from SM 109. Energies as in Table 4.1.

Transition	Energy (keV)	B(E2) e^2b^2	SM	CE
	^{107}Sn exp.			
$B(E2; 5/2_1^+ \rightarrow 3/2_1^+)$	704	$0.045^{+0.023a}_{-0.017}$	0.019	0.030(3)
	^{109}Sn exp.			
$B(E2; 5/2_1^+ \rightarrow 3/2_2^+)$	925	$0.029^{+0.014b}_{-0.015}$	0.007	0.030(3)
$B(E2; 5/2_1^+ \rightarrow 7/2_2^+)$	1078	$0.060^{+0.020b}_{-0.022}$	0.047	0.060(5)
$B(E2; 5/2_1^+ \rightarrow 9/2_1^+)$	1240	$0.085^{+0.032b}_{-0.034}$	0.032	0.074(6)
$B(E2; 5/2_1^+ \rightarrow 3/2_1^+)$	665	$0.013^{+0.008a}_{-0.011}$	0.001	0.030(3)
$B(E2; 5/2_1^+ \rightarrow 5/2_2^+)$	678	$<0.012^a$	0.004	0.044(4)
$B(E2; 5/2_1^+ \rightarrow 1/2_2^+)$	991	$<0.028^b$	0.008	0.015(1)

[a] Error includes Ni-Sn correlations. [b] Error includes Sn correlations.

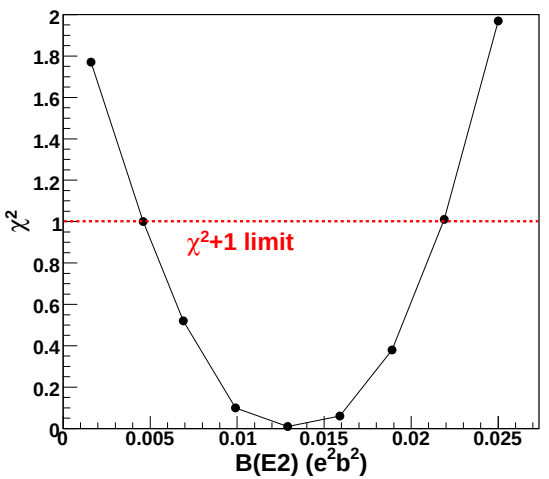

Figure 4.12: The χ^2+1 limits for the $B(E2; 5/2_1^+ \rightarrow 3/2_1^+)$ value. See section 4.2.6 for details. The lines are drawn to guide the eye.

Table 4.4: The single-particle orbits used in the shell-model calculations for ^{107}Sn and ^{109}Sn. The units are in MeV. All sets were used for the ^{107}Sn calculations, with the exception of the set labeled SM 109. The indicated reference was used for the position of the three higher-lying orbits.

Orbit	SM A	SM B	SM C	SM D	SM E	SM F	SM 109
$d_{5/2}$	0.0	0.0	0.0	0.0	0.0	0.172	0.172
$g_{7/2}$	0.172	0.172	0.172	0.172	0.172	0.0	0.0
$s_{1/2}$	1.55	2.45	2.2	1.6	2.6	2.3	2.3
$d_{3/2}$	1.66	2.54	2.3	2.0	2.7	2.5	2.1
$h_{11/2}$	3.55	3.0	2.7	2.3	3.4	3.4	3.4
Reference	[6]	[18]	[81]	[82]			

The procedures for the error analysis were also similar to as described previously. Each reduced matrix element was fixed at points around the minimum while other unfixed reduced matrix elements were free to vary. The process was repeated until the $\chi^2 + 1$ limits were found. The procedure is highlighted in Fig. 4.12. The red-dashed line marks the $\chi^2 + 1$ limits. The error given in Table 4.3 also contains an additional contribution. Each Sn reduced matrix element was individually fit with all other Sn reduced matrix elements set to zero. The resulting deviations were treated as systematic errors and included in the total error. In addition, a second set of starting values for the reduced matrix elements was also tested. All relevant reduced matrix elements coupling the two $3/2^+$ states were exchanged. This had an influence of $\sim$0.001 e^2b^2 on the reduced transition probabilities of the two $3/2^+$ states.

4.2.7 Shell-model calculations

A series of shell-model calculations were carried out to compare with the measured $B(E2)$ values. In all calculations a ^{100}Sn core was used. The input included an effective interaction based on a G-matrix renormalized CD-Bonn potential and several sets of single-neutron energies relative to ^{100}Sn. The list of single-neutron energies is given in Table 4.4 and the two-body matrix elements for the G-matrix renormalized CD-Bonn interaction are given in Appendix C. The reduced matrix elements for all calculations were generated using the effective neutron charge of e_ν=1.0e and the neutron g-factors g_l=0 and g_s=-3.82.

The sets labeled SM A-SM F were used in the ^{107}Sn calculations and the calculated energy levels are shown in Fig. 4.10. The sets were taken from

several references as the location of the single-neutron energies relative to ^{100}Sn is uncertain at this time. The only known information is the energy splitting between the two lowest-lying orbitals. The spin ordering of the states is however uncertain and each set of calculations was performed with the orbits inverted. Additionally, the single-neutron states used as input were fit to the suggested single-neutron states in ^{109}Sn. The best sets were produced by locating the χ^2 minimum based on the position of the single-neutron states in ^{109}Sn. The single-neutron energies relative to ^{100}Sn were varied in units of 0.1 MeV during the fitting. The results of the fit are given in right side of Fig. 4.10.

For the ^{109}Sn calculations, the single-neutron energies of SM F were used with an adjusted position for the $d_{3/2}$ orbit. The energy of the orbit was adjusted in order to reproduce the position of the $3/2_1^+$ state in ^{109}Sn. Only increments of the orbit in units of 0.1 MeV were considered. The resulting set of energies is labeled as SM 109.

4.2.8 Core-excitation calculations

Calculations based on the simple core-excitation model were also carried out and compared to the extracted $B(E2)$ values. The core-excitation states correspond to a single hole or particle outside of an excited ^{108}Sn core with $B(E2) = 0.222(19)e^2b^2$ [9]. For a particle or hole in the $d_{5/2}$ orbit, the coupling results in a multiplet of states with $J \in 1/2^+, 3/2^+, 5/2^+, 7/2^+, 9/2^+$. The $B(E2)$ values presented in Table 4.3 correspond to the case in which the respective state is a member of the core-excitation multiplet.

4.2.9 Discussion

The shell-model calculated $B(E2)$ values for the $3/2_1^+$ state in ^{107}Sn are compared to the experimentally measured value in Fig. 4.13. All the predicted values lie outside of the 1σ limits of the measurement. Interestingly, in all cases the calculations with the $g_{7/2}$ orbit as the lowest-lying orbit relative to ^{100}Sn are enhanced compared to the respective $d_{5/2}$ calculation. The inversion of the orbits may be partly responsible for explaining the missing strength.

The higher-lying orbits may also contribute to the missing strength. For instance, the calculations were repeated by fixing the $h_{11/2}$ orbits position to 2.3 in the SM F set, which resulted in an $\sim$30% increase in the transition strength. Likewise, setting the $s_{1/2}$ state to 1.55 MeV in the SM F set resulted in an $\sim$10% increase in the value. Finally, setting the $d_{3/2}$ to 1.66

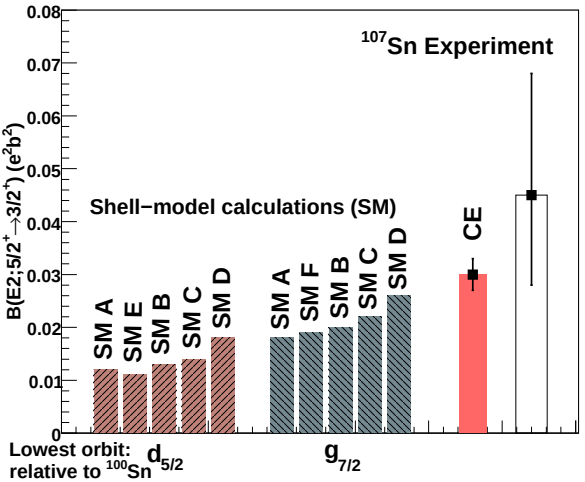

Figure 4.13: The calculated $B(E2)$ values for ^{107}Sn with the various sets of single-neutron energies (see Table 4.4) relative to ^{100}Sn. The core-excitation (CE) calculation, given in Table 4.3, is also shown for comparison.

MeV led to a decrease of $\sim$20%. The positions of the three higher-lying orbits are thus clearly important for explaining the transition strengths in the odd-Sn nuclei.

The ^{108}Sn core-excitation calculations predict a $B(E2)$ value that agrees within the 1σ limits of the measurements. If instead a ^{106}Sn core is assumed, then the core-excitation $B(E2)$ value would be 0.026(5)e^2b^2, based on the value given Ref. [9]. This value underestimates the measured mean value but overlaps within the 1σ limits. Both these predictions lie on the very lower limit of the measured 1σ error bars. A new measurement aiming for better precision would help determine if the core-excitation model provides a good explanation for the increased transition strength.

In ^{109}Sn, the $3/2_2^+$, $7/2_2^+$, and $9/2_1^+$ states are well described by the core-excitation calculations and are underestimated by the shell-model calculations. The $1/2_2^+$ state and $5/2_2^+$ state may also be members of the core-excitation multiplet, however, their transition probabilities agree with both shell-model and core-excitation model calculations. Since the $1/2_1^+$ state is believed to be the single-neutron state, and since it was not observed in the experiment, the $1/2_2^+$ state is left as the best candidate for a collective state. The strong observation of the $3/2_2^+$ state is unexpected since it has

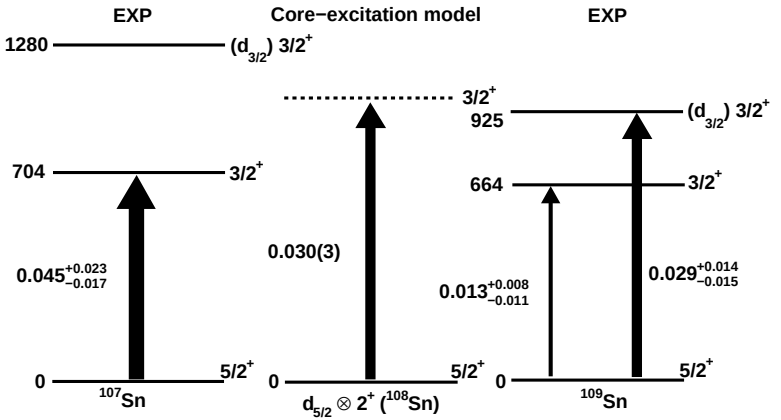

Figure 4.14: Comparison between the $B(E2)$ values for the low-lying $3/2^+$ states in ^{107}Sn and ^{109}Sn with the prediction of the simple core-excitation model (Table 4.3). The energies are given in keV and the $B(E2)$ values are indicated next to the thick arrows and given in e^2b^2. The states thought to be single-neutron states from previous studies are indicated [75, 77].

been labeled as a single-neutron state [75, 77]. The assignment is based on the β-decay feeding strengths when compared to the nuclei $^{111-117}$Sn [83]. The $3/2^+$ states in ^{107}Sn and ^{109}Sn are shown in Fig. 4.14 and are compared to predictions of the core-excitation model. Here, it can be noted that the suggested $d_{3/2}$ state moves up in energy when moving from ^{109}Sn to ^{107}Sn. This may mean that the $3/2^+_2$ state in ^{109}Sn is based on a mixture of collective and single-neutron states. Similar mixed states have been observed in previous Coulomb excitation experiments in ^{117}Sn [84]. An additional study using nuclear reactions could help identify the character of the state.

Lastly, the shell-model calculations employed in this work did not contain any neutron or proton excitations across the $N = Z = 50$ shell gap. The missing degrees of freedom might lead to an increase in the calculated transition probabilities [6, 7, 8, 9]. Recent shell-model calculations in ^{98}Cd, without excitations across the $N = Z = 50$ gap, predicted a $7/2^+$ ground state in ^{101}Sn [85]. When neutron core excitations were included, the calculations instead predicted a $5/2^+$ state in ^{101}Sn. It will be interesting to find out if the effect of the core excitations in ^{107}Sn washes out the differences between the $d_{5/2}$ and $g_{7/2}$ calculations, as shown in Fig. 4.13.

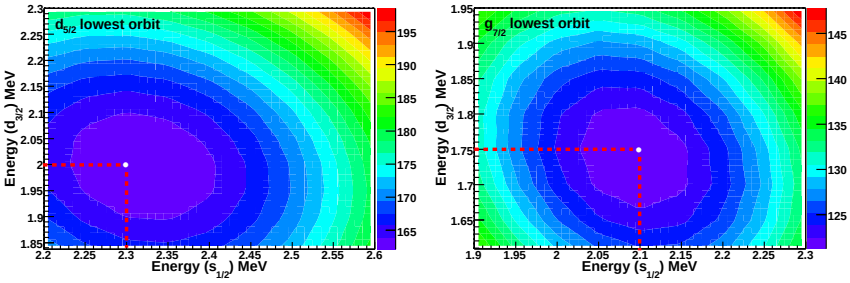

Figure 4.15: The calculated rms deviation for the two fits discussed in the GOSIA simulated γ-ray spectrum section. Based on work presented in Refs. [86, 87].

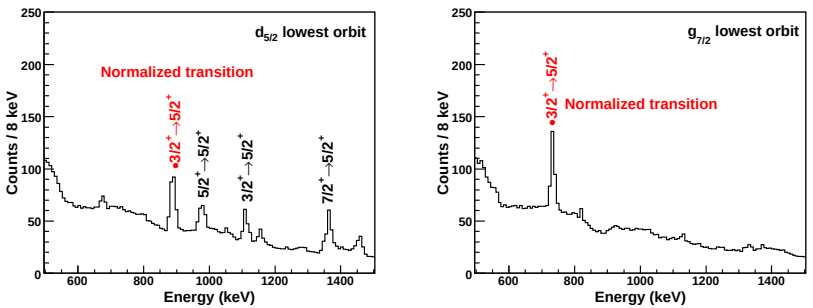

Figure 4.16: The GOSIA simulated spectra for the two low-lying orbits relative to ^{100}Sn. Based on work presented in Refs. [86, 87]

4.2.10 GOSIA simulated γ-ray spectra

While the GOSIA code is mainly used for determining reduced matrix elements from relative γ-ray yields, it can also be used in the reverse order. Given a set of reduced matrix elements, the code can be used to calculate the expected γ-ray yields for a particular experiment. This type of analysis was explored for the ^{107}Sn experiment. The work described in this section is presented in Refs. [86, 87].

The analysis started with a set of reduced $E2$ and $M1$ matrix elements which was generated from a shell-model calculation. The effective interaction was derived as discussed in section 4.2.7 while the single-neutron energies were taken from a two dimensional fit of the $d_{3/2}$ and $s_{1/2}$ orbits

to the excited states in the nucleus ^{109}Sn. The rms deviation of the fits as a function of these two orbits is shown in Fig. 4.15. The fits were carried out for both choices of the lowest-lying orbit relative to ^{100}Sn with a fixed $h_{11/2}$ orbit at 3.0 MeV.

The shell-model reduced matrix elements were fed into the GOSIA code along with the experimental parameters defining the detector geometries. The code was used to calculate the expected peak areas based on normalizing to the single observed γ ray in the ^{107}Sn experiment. The peak areas were added to the experimentally determined background spectrum and broadened to meet the measured full-width-at-half-maximum. The results are shown in Fig. 4.16. The two spectra show that on basis of the shell-model calculations the $g_{7/2}$ orbit would be preferred as the lowest-lying orbit relative to ^{100}Sn. Of course the method depends on to what extend the shell-model calculations reproduce the energies and transition strengths of the experimentally observed excited states. In any case, the method provides an approach for estimating the observed peak areas for a given experiment based on model predictions.

4.3 Coulomb excitation of ^{107}In

As a consequence of the isobaric contamination present during the ^{107}Sn experiment, it was also possible to also extract a $B(E2)$ value for the isotope ^{107}In. The peak areas and intensities relevant for the analysis are given in Table 4.5. Two γ rays were observed which could be assigned to ^{107}In [74]. These include the 1001 keV γ ray from the $11/2^+$ state at 1001 keV and the 429 keV γ ray depopulating the $3/2^-$ state at 1107 keV. This latter transition feeds the isomeric $1/2^-$ state at 679 keV [88].

The ^{58}Ni peak was corrected for the Sn to In ratio as described in section 4.2.4. However, the In fraction contains two different components. These include ^{107}In in the ground state and also ^{107}In in the isomeric state. Considering this, the 429 keV γ ray could either be the result of Coulomb excitation of the ground-state (see previous measurements of In nuclei [89, 90]) or Coulomb excitation of the isomeric state. The isomeric fraction was estimated using data from previously known electron capture decay measurements [74]. Using this information and measured decay data from the current experiment resulted in an isomeric fraction of 0.04(5) and a ground-state fraction of 0.77(8) of the total data set.

The $B(E2)$ value for the $11/2^+$ state was extracted in the same fashion as described for the ^{107}Sn $B(E2)$ value. The result is presented in Table 4.6 along with the results of large-scale-shell model calculations, previous unified-model calculations, and earlier Coulomb excitation experiments

Table 4.5: Relevant data for the analysis of the ^{107}In experiment (Paper III), energies taken from Refs. [73, 74].

Transition	E_γ (keV)	Yield	I_γ
In $3/2^- \rightarrow 1/2^-$	429	<315	<0.77
In $11/2^+ \rightarrow 9/2^+$	1001	658(31)	2.68(17)
Ni $2^+ \rightarrow 0^+$	1454	196(28)	1.00(15)

Table 4.6: Measured and calculated reduced transition probabilities, $B(E2, 9/2^+ \rightarrow 11/2^+)$ values, for ^{107}In. Experimental data for the heavier-mass In isotopes taken from Refs. [89]. See section 4.3 for a discussion regarding the shell-model (SM) calculations and the unified-model (UM) calculations.

	Energy (keV)	$B(E2)$ (e^2b^2)
Exp	1001	0.12(2)
SM A	1063	0.09
SM B	1063	0.12
UM	-	0.08
^{113}In	1173	0.093(6)
^{115}In	1133	0.100(5)

[89]. The shell-model calculations were carried out using a G-matrix renormalized CD-Bonn interaction with ^{88}Sr as the core. The proton and neutron single-particle energies were taken from Ref. [91] and were $d_{5/2} = 0.00$ MeV, $s_{1/2} = 1.26$ MeV, $d_{3/2} = 2.23$ MeV, $g_{7/2} = 2.63$ MeV, and $h_{11/2} = 3.50$ MeV for neutrons and $p_{1/2} = 0.00$ MeV and $g_{9/2} = 0.90$ MeV for protons. In order to gain computational efficiency, only a maximum of three neutrons were allowed to occupy the $h_{11/2}$ orbit. The effective charges used in the calculations were taken from Refs. [92, 93]. These values, e_ν=1.1e and e_π=1.7e, however underestimate the extracted $B(E2)$ value, indicated as SM A in Table 4.6. Better agreement can be found by increasing the neutron effective charge to e_ν=1.3e (SM B). The unified-model calculations were carried out in Ref. [94] for ^{115}In. These calculations were normalized using the known $B(E2, 0^+ \rightarrow 2^+)$ value for ^{116}Sn. It can be expected that this value holds for ^{107}In based on the roughly constant $B(E2)$ values down to ^{106}Sn (Fig. 1.2). This observation is also supported by the Coulomb excitation measurements in ^{113,115}In where these results overlap within the 1σ limits of the ^{107}In measurement.

Table 4.7: Preliminary analysis for FRS and LYCCA identification of Sn nuclei.

Isotope	ZvsAoq	ZvsAoq +LYCCA	time
^{112}Sn	5.7×10^7 p	2.6×10^7 p	20 h
^{104}Sn	1.5×10^7 p	5.7×10^6 p	64 h

4.4 Relativistic Coulomb excitation of ^{104}Sn

The ^{107,109}Sn radioactive ion beam experiments are part of a more general study of isotopes near ^{100}Sn. The main goals have been to identify and characterize the collective properties of low-lying states in this mass region. In particular, much of the interest has been driven by the observed enhancement in the reduced transition probabilities in the neutron-deficient even-even Sn nuclei (see Fig. 1.2b). The previously reported results include Sn nuclei down to mass number $A = 106$. In the current section, the preliminary results of a relativistic ion beam experiment, aimed at measuring the reduced transition probability of the first 2^+ state in ^{104}Sn, are described.

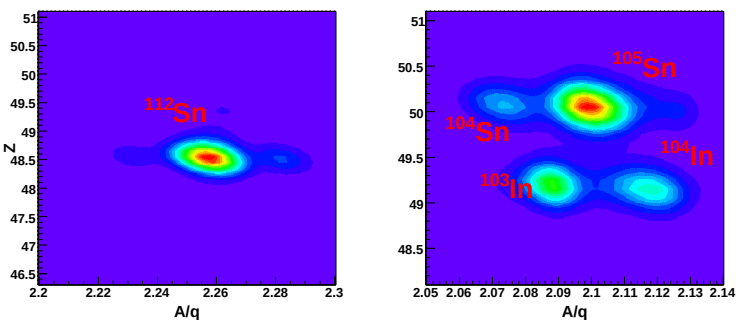

Figure 4.17: FRS identification for the ^{112}Sn normalization run (left) and for the ^{104}Sn run (right).

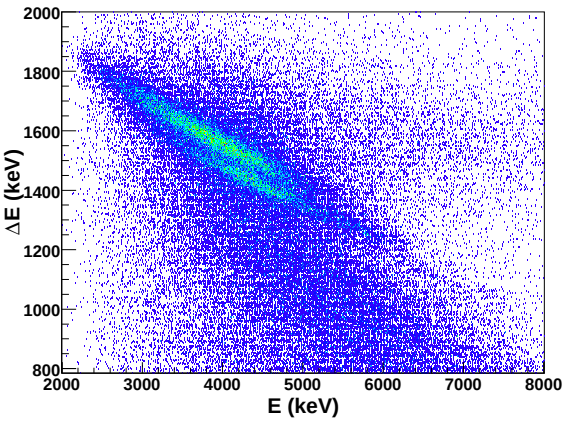

Figure 4.18: LYCCA ΔE vs E spectrum from part of the ^{104}Sn run.

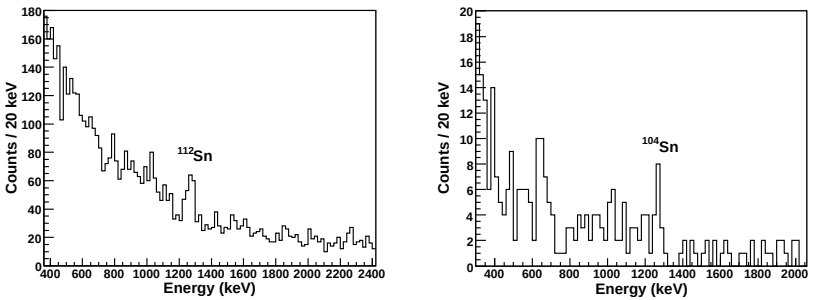

Figure 4.19: Preliminary γ-ray spectra for ^{112}Sn and ^{104}Sn.

Two different beams were used during the course of the experiment. A ^{112}Sn beam, created by the fragmentation of the ^{9}Be target using a 700 MeV/u ^{124}Xe primary beam with an intensity of $\sim 1\times10^{7}$ p/s, was used for normalization. The ^{104}Sn beam was produced with a 793 MeV/u ^{124}Xe primary beam with an intensity of $\sim 1\times10^{9}$ p/s. The FRS identification is shown in Fig. 4.17, where the stable primary beam is seen in the normalization run and four different isotopes were present during the ^{104}Sn run. These include ^{104,105}Sn and ^{103,104}In. The number of identified ^{112}Sn and ^{104}Sn ions, in the FRS and also in LYCCA, over the course of the experiment is shown in Table 4.7. It can be seen that there is a significant loss in

the number of ions before and after the secondary target, which is as of yet unexplained. A sample of the collected ΔE vs E spectrum from LYCCA is shown in Fig. 4.18.

Preliminary γ-ray spectra from the experiment for ^{112}Sn and ^{104}Sn are shown in Fig. 4.19. The spectra were generated using a number of different conditions placed on the various detectors in the flight path of the ions. These cuts included identification using the FRS detectors, i.e. Z vs A/q, target multiplicity equal to one, identification in LYCAA ΔE vs E, and a cut on the scattered particle angles in order to remove contributions from nuclear interactions. The work is still ongoing in order to identify the best selection of cuts to maximize the signal to background ratio.

Chapter 5

The ^{170}Er experiment

5.1 Introduction

The Er nuclei, starting from ^{162}Er up to ^{170}Er, exhibit very similar features. These nuclei are characterized by rotational ground-state bands and several other low-lying rotational structures. There are smooth variations in the energies and transition probabilities of the ground-state bands across the chain of nuclei, as shown in Ref. [95], for example. This is a typical characteristic of rotational motion. Furthermore, low-lying rotational bands with large transition probabilities to the ground state have also been observed in these nuclei. The bands are thought to be based on one-phonon vibrational states. An interesting question is related to the existence of rotational bands built upon two-phonon states. Levels in the nuclei ^{166,168}Er have been interpreted as such states [96, 97, 98, 99, 100]. One of the main motivations for the ^{170}Er experiment was to search for two-phonon vibrational states.

A unique feature of ^{170}Er is that two low-lying rotational bands have been observed at about the same energy. In the model of Bohr and Mottelson, to the first order, rotational bands should exhibit smooth variations in the energies and transition probabilities of the states within and between the bands. However, the closeness in energy of the two low-lying bands results in a strong interaction between them [101], leading to deviations from the expected smooth behavior. Studying the transition probabilities of states within and connecting the two bands makes it possible to get a handle on the strength of the interaction. This was also one of main the goals for the analysis of the experimental data.

The ^{170}Er experiment was carried out using the GASP and LuSiA detector systems as described in Ch. 3. A 117 MeV ^{32}S beam was produced

Table 5.1: Example of a single GASP event buffer.

GASP format		ROOT format
f008	New event	
	RunNumber	1
0001	GeMult	1
0324	GeEnergy	804
040c	GeTime	1036
0026	GeID	38
0001	SiMult	1
00f2	SiEnergy	242
0776	SiTime	1910
006f	SiID	111
	SiDet	4
	SiSide	0

using the accelerator at the Laboratori Nazionali di Legnaro and incident on a 1 mg/cm^2 thick isotopcially enriched ^{170}Er target. The data reduction techniques, analysis, and discussion of the results are presented in detail in this chapter. The work described here is presented in Paper IV.

5.2 Data acquisition, sorting, and reduction

The LuSiA detector was fully integrated into the EUCLIDES [102] data acquisition setup. The detector preamplifier signals were processed using mesytec shaping amplifiers [67] and further by the pre-existing ADC/TDC conversion system [103]. After the read out of the signals, the data were written in standard GASP event-by-event format to disk using the GSORT program [104]. Each event buffer contained the Ge and Si detector multiplicities and the corresponding time and energy signals. The events were recorded under the condition that at least one particle and at least one γ ray were detected in LuSiA and GASP, respectively.

The data were sorted and reduced to a form suitable for analysis using a series of ROOT based programs. The initial step was to convert the raw GASP data to ROOT trees. Table 5.1 shows the format of the data in a single buffer. The ROOT data was subsequently reduced based on several conditions described in the following sections. These conditions included

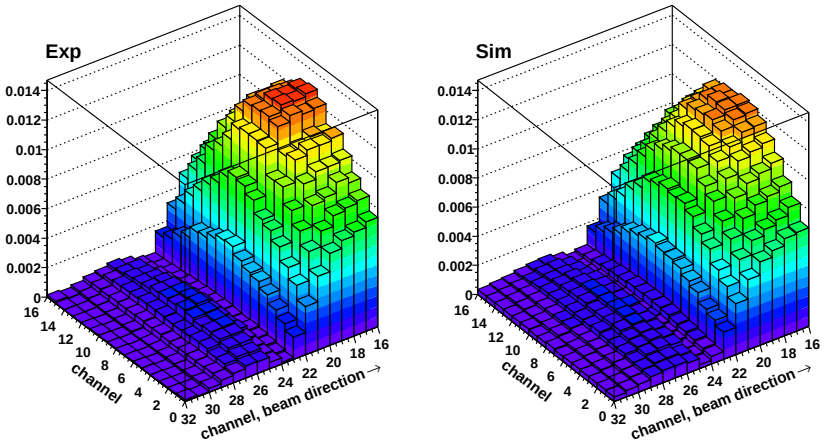

Figure 5.1: Normalized measured particle hit pattern for a single DSSSD in LuSiA (left) compared to the normalized simulated hit pattern (right).

1) event selection based on DSSSD strip multiplicity, 2) a kinematical cut on the energy and scattering angles of the detected particles, 3) a coincidence condition between front and back strips of the DSSSD and between particles and γ rays, 4) reconstruction of the scattered ^{170}Er target nuclei, and 5) Doppler correction of the γ-ray spectrum.

5.3 Particle data

A typical particle hit pattern from the left DSSSD, gated on the $2_g^+ \rightarrow 0_g^+$ transition in ^{170}Er, is shown in the first panel of Fig. 5.1. Left refers to the direction when facing downstream with respect to the beam direction. As a result of the energy loss in the target and the Al foil placed around the target, only the ^{32}S particles were detected. The observed features arise from a combination of different sources. These include the angular distribution of the Coulomb excitation cross section, energy loss in the target and Al foil, and the kinematics of the reaction.

To get a better understanding of the observed structure in Fig. 5.1, Geant4 [105] simulations of the detector setup were carried out. The results are shown in the second panel in Fig. 5.1. The simulations included the ge-

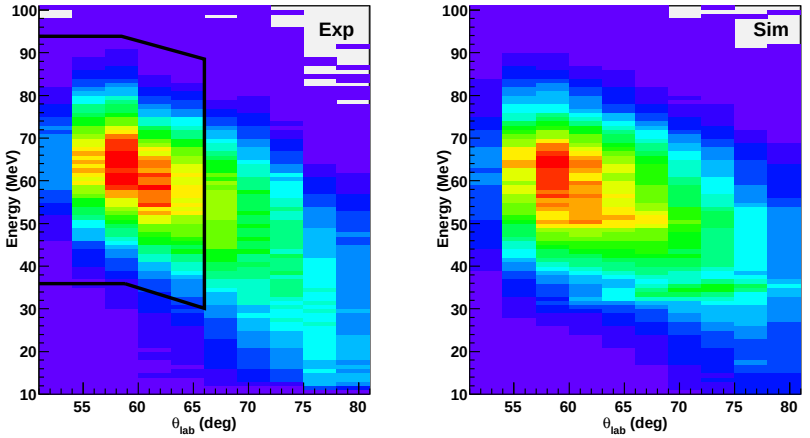

Figure 5.2: Experimentally determined energy vs scattering angle (left) compared to the simulated energy vs scattering angle (right).

ometry of the target, DSSSD, and Al foil. The ^{32}S particles were emitted from a source placed in the ^{170}Er target. The energies of the particles were calculated from the two-body kinematics of the reaction while the emission angles were determined from the GOSIA calculated angular distributions for the 2_g^+ state. The simulated pattern well reproduces the measured pattern. The broad bump in the forward beam direction, corresponding to lower scattering angles, is related to the Coulomb excitation cross section (see Fig. 3.2). The Al foil and target thickness are both important for the attenuation at the higher scattering angles. The target shadow is clearly visible around strips 23 and 24 in both hit patterns. At these angles, the scattered particles do not escape the target volume. The simulations show that the Al foil was thinner than the quoted value of 12 μm as this thickness resulted in a larger attenuation of the scattered particles than what was observed experimentally.

The measured energy versus scattering angle for the collected particles is shown in the left panel of Fig. 5.2 when gated on the $2_g^+ \rightarrow 0_g^+$ transition. Without the γ-ray gate, a broad band of particles appears below 30 MeV, indicating that these events originate from particles scattered by other materials than the target. The data presented in the figure correspond to the events collected in one of the four DSSSDs.

The detected particle energy in Fig. 5.2 was calibrated based on the

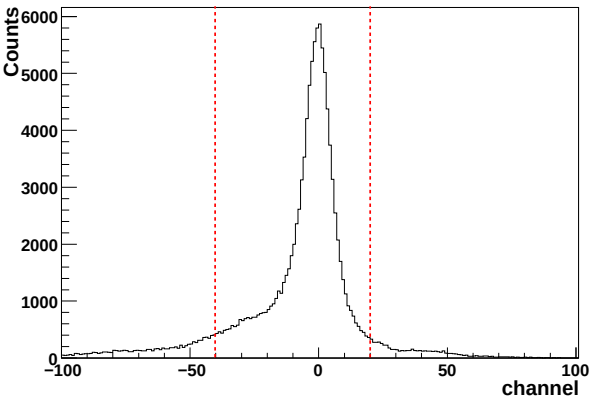

Figure 5.3: Time difference spectrum between front and back strip hits of the DSSSD. The red lines mark the conditions imposed during the data analysis.

Geant4 simulations. The corresponding simulated plot is shown in the right panel of Fig. 5.2. The calibrated energy depends on the Al foil thickness. This is however not an issue for the analysis for two reasons. The detected particle energy is only used to set the kinematical cut to select events scattered from the target. During the Doppler correction, the detected particle angles were used to determine the energies of the scattered particles rather than using the energies measured in the DSSSD. The kinematical cut imposed during the analysis is represented by the black markers in Fig. 5.2 and corresponds to the angular range of $52.4^o < \theta < 66.0^o$.

For the particle events, coincidence cuts were defined for the front and back strips of the DSSSD. The time spectrum is shown in Fig. 5.3 and the red markers indicate the conditions imposed in the analysis. The width of the cut corresponds to 14 ns.

5.4 Particle-γ-ray coincidence data

After selection of the suitable events based on the particle energies and scattering angles, the data were processed in a reconstruction and Doppler correction routine. The Doppler correction formula depends on the angles and energies on the scattered ^{170}Er particles. This information was cal-

culated using the standard formulation for two-body scattering (see Appendix A) and the measured angles of the ^{32}S particles, since the ^{170}Er nuclei were not detected by the DSSSD. The scattering was assumed to have occurred in the center of the target. The collected γ-ray spectrum from the experiment before and after the Doppler correction is shown in Fig. 5.4.

A coincidence condition was also applied on the particle-γ-ray time difference. The measured time difference spectrum is shown in Fig. 5.5 and the cut used in the analysis corresponds to 61 ns.

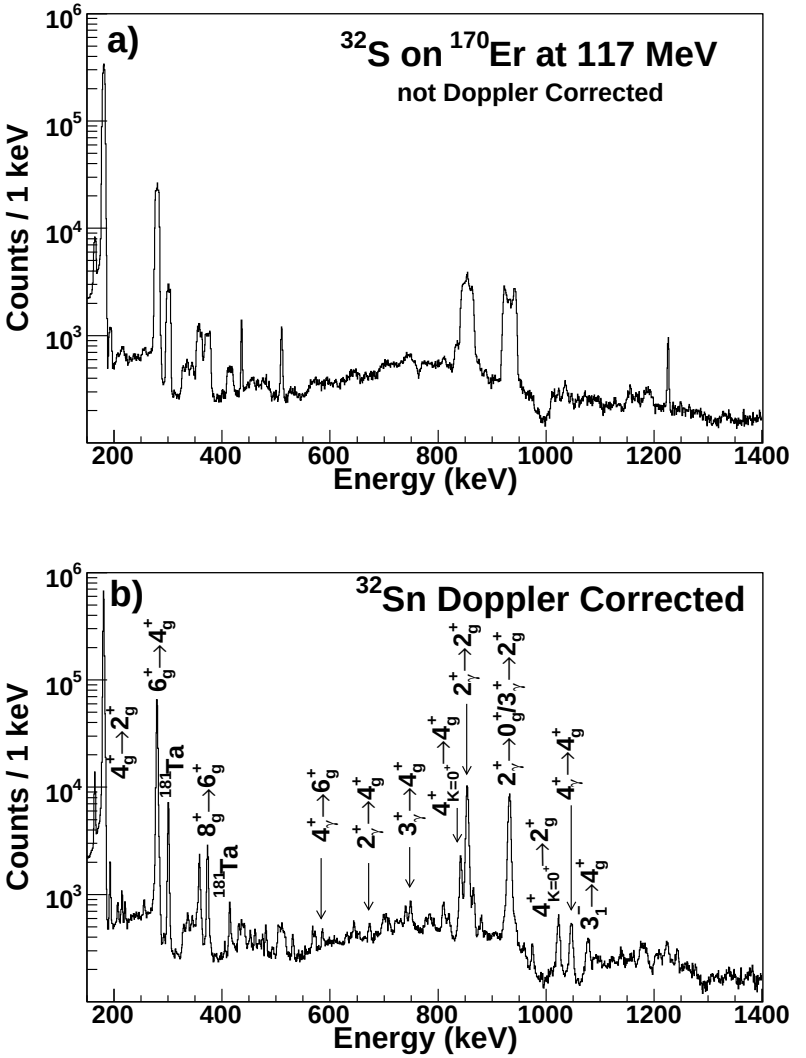

Figure 5.4: The (a) raw and (b) Doppler corrected γ-ray spectra from the ^{170}Er experiment. The ^{181}Ta peaks originate from the collimator placed upstream of the target.

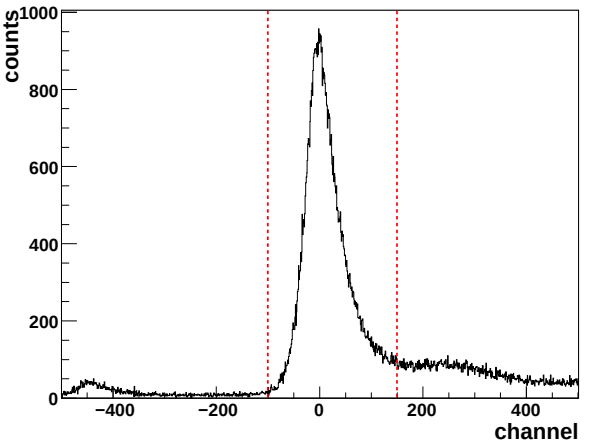

Figure 5.5: Time difference spectrum between particles and γ rays. The red lines mark the conditions imposed during the data analysis.

5.5 Data analysis

The γ-ray data were analyzed in the standard fashion by constructing a γ-γ matrix to assign each of the γ rays a position in the level scheme of the nucleus. The scheme is shown in Fig. 5.6 and is based on the adopted data given in Ref. [106]. The ground-state band was observed up to spin 10^+, the $K^\pi = 0^+$ band up to 6^+, and the γ band also up to spin 6^+. Three other low-lying structures were observed, which include the band head of the $K = 2^+$ band at 1416 keV, a member of the $K = 2^-$ band, and three states belonging to the $K = 1^-$ band. A previously unobserved level was also found at 1789 keV, based on a 686 keV γ ray in coincidence with the 843 keV transition.

A set of intensities was extracted for the observed γ rays using the RADWARE [107, 108] package and is given in Table 5.2. The intensities of the two lowest-lying ground-state transitions were not possible to extract due to uncertainties in the efficiency calibration at low energies. These were not used directly in the analysis but instead their reduced matrix elements provided additional tests of the fit results.

The yields were analyzed using the GOSIA code discussed in Ch. 3. The observed levels for the three lowest-lying bands were included in the analysis with all possible $E2/M1$ matrix elements. The coupling between the γ and $K^\pi = 0^+$ bands was however assumed to be zero. In addition,

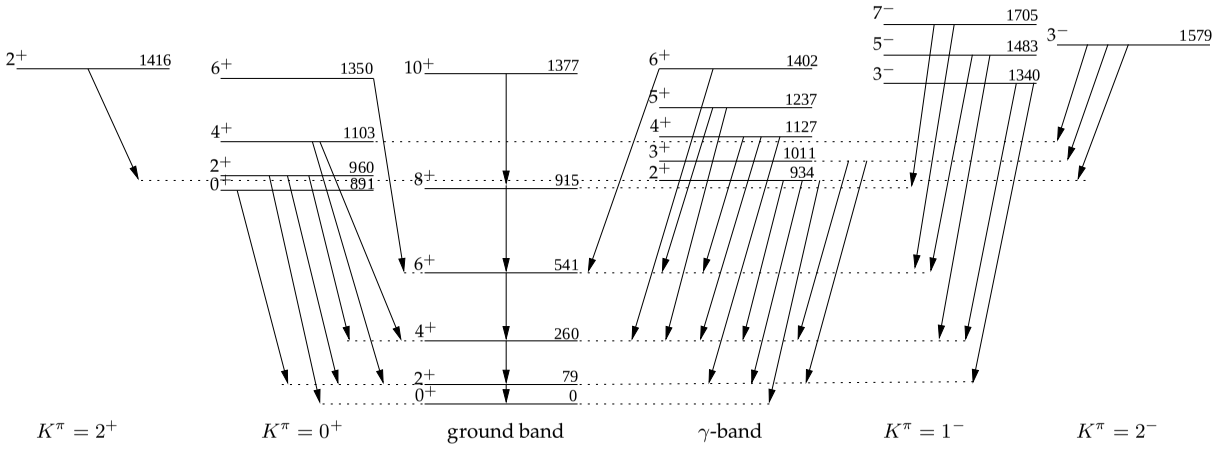

Figure 5.6: The determined level scheme from the ^{170}Er experiment. The arrows indicate the observed transitions and the energies are given in keV. Figure from Paper IV.

Table 5.2: Experimental data used in the GOSIA analysis of the ^{170}Er experiment.

Transition	Energy (keV)	Rel. Int.	$I_i \rightarrow I_f / I_i \rightarrow I_f$	Ref. [106]
$6^+_g \rightarrow 4^+_g$	280	100(6)	$2^+_\gamma \rightarrow 4^+_g / 2^+_\gamma \rightarrow 2^+_g$	0.014(3)
$8^+_g \rightarrow 6^+_g$	374	4.88(30)	$2^+_\gamma \rightarrow 0^+_g / 2^+_\gamma \rightarrow 2^+_g$	0.897(24)
$10^+_g \rightarrow 8^+_g$	462	0.37(4)	$3^+_\gamma \rightarrow 4^+_g / 3^+_\gamma \rightarrow 2^+_g$	0.146(11)
$2^+_\gamma \rightarrow 0^+_g / 3^+_\gamma \rightarrow 2^+_g$	934/932	42(3)	$4^+_\gamma \rightarrow 2^+_g / 4^+_\gamma \rightarrow 4^+_g$	0.86(11)
$2^+_\gamma \rightarrow 2^+_g$	855	43(3)	$2^+_{K=0^+} \rightarrow 4^+_g / 2^+_{K=0^+} \rightarrow 2^+_g$	0.65(4)
$2^+_\gamma \rightarrow 4^+_g$	674	0.55(6)	$2^+_{K=0^+} \rightarrow 0^+_g / 2^+_{K=0^+} \rightarrow 2^+_g$	0.63(7)
$3^+_\gamma \rightarrow 4^+_g$	750	1.45(11)	$4^+_{K=0^+} \rightarrow 2^+_g / 4^+_{K=0^+} \rightarrow 4^+_g$	0.273(22)
$4^+_\gamma \rightarrow 2^+_g$	1049	2.37(18)	$6^+_{K=0^+} \rightarrow 4^+_{K=0^+} / 6^+_{K=0^+} \rightarrow 6^+_g$	0.076(25)
$4^+_\gamma \rightarrow 4^+_g$	867	3.26(22)		
$4^+_\gamma \rightarrow 6^+_g$	587	0.44(5)		
$5^+_\gamma \rightarrow 4^+_g$	976	0.72(7)		
$5^+_\gamma \rightarrow 6^+_g$	696	0.17(11)		
$6^+_\gamma \rightarrow 4^+_g$	1142	<0.62		
$6^+_\gamma \rightarrow 6^+_g$	861	<2.50		
$0^+_{K=0^+} \rightarrow 2^+_g$ / $6^+_{K=0^+} \rightarrow 6^+_g$	812/810	1.67(16)		
$2^+_{K=0^+} \rightarrow 0^+_g$	960	0.35(7)		
$2^+_{K=0^+} \rightarrow 2^+_g$	881	0.92(10)		
$2^+_{K=0^+} \rightarrow 4^+_g$	700	0.73(13)		
$4^+_{K=0^+} \rightarrow 2^+_g$	1024	2.37(17)		
$4^+_{K=0^+} \rightarrow 4^+_g$	843	7.96(49)		
$4^+_{K=0^+} \rightarrow 6^+_g$	563	<0.11		
$3^-_1 \rightarrow 4^+_g$	1080	1.36(11)		
$3^-_1 \rightarrow 2^+_g$	1262	<0.40		
$3^-_2 \rightarrow 2^+_\gamma$	645	0.56(6)		
$3^-_2 \rightarrow 3^+_\gamma$	569	0.50(6)		
$3^-_2 \rightarrow 4^+_{K=0^+}$	476	0.26(4)[a]		
$2^+_{K=2^+} \rightarrow 2^+_\gamma$	481	0.48(5)[a]		

Level	Lifetime (ps) Ref. [106]
2^+_γ	2.61(9)
$2^+_{K=0^+}$	17.46(216)

[a] May contain a contribution from ^{181}Ta.

several states on top of each band were also included to account for any unobserved excitation. The observed three higher-lying structures exhibited little sensitivity to the data set and were not included. The effects of these matrix elements were instead estimated as discussed later in this chapter. In addition to the definition of the level scheme, several previously known branching ratios and lifetimes were used as input to the code and are also

shown in Table 5.2.

The first attempt at fitting the matrix elements was carried out using the coupling schemes defined in Ch. 2, based on the collective model of Bohr and Mottelson. An intrinsic matrix element was defined for each of the bands and inter-band transitions. The $E2$ reduced matrix elements were coupled using the leading order relation (Eq. 2.24). The $M1$ reduced matrix elements for the γ and $K^\pi = 0^+$ bands were coupled using Eqs. 2.28 and 2.29, respectively. The simplified nature of the coupling schemes was however not sufficient to reproduce the observed intensities. The reason may be related to the near degeneracy of the two 4^+ levels in the γ and $K^\pi = 0^+$ bands, which may result in mixing of the two states [101]. The mixing breaks the simple relations of the coupling schemes. For this reason, the inter-band $E2$ reduced matrix elements coupling the 0^+, 2^+, and 4^+ states of each of the bands were varied individually. All other matrix elements were coupled, as described previously. The method is similar to other procedures defined in Refs. [109, 110]. In total, 19 reduced matrix elements were fit to 31 experimentally defined data points and resulted in a χ^2 value of $\sim$1.8.

The determined $E2$ reduced matrix elements are given in Table 5.3. For the uncoupled reduced matrix elements the values predicted by Eq. 2.24 are also given for comparison. Calculations using the IBA-1 model were also carried out (section 5.6) and the results are also given. Previously measured reduced matrix elements are also presented.

Several tests were carried out to check the sensitivity of the determined reduced matrix elements to the higher-lying states, to the phases of the reduced matrix elements, and to test the uniqueness of the χ^2 minimum. The effect of the higher-lying states was investigated by including these states in the GOSIA fit with fixed reduced matrix elements based on observations from nearby nuclei. However, no significant effect was found. The effect of the phases was investigated by flipping the signs of the uncoupled reduced matrix elements and repeating the minimization. In the best set presented here, the initial starting values corresponded to the signs of the Clebsch Gordan coefficients. The only case which produced a lower χ^2 value was for the $2^+_\gamma \rightarrow 2^+_g$ transition. The positive choice was however adopted as it agrees with both the Bohr-Mottelson model and the IBA-1 calculations. The analysis was not sensitive to the signs of the $M1$ reduced matrix elements. Finally, when performing a least-squares minimization there is always the chance that the determined minimum is not the global minimum. To examine this, several different starting values for the uncoupled $E2$ reduced matrix elements and intrinsic $M1$ matrix elements were tested. The procedure revealed the existence of several local minima, but none with lower χ^2 values than the minimum presented here.

Table 5.3: The extracted $E2$ reduced matrix elements, given in eb, from the GOSIA analysis for the ^{170}Er experiment. The IBA-I calculations are described in section 5.6.

Transition	GOSIA	IBA-I	BM[b]	Previous
In-band E2 transition matrix elements.				
$2^+_g \rightarrow 0^+_g$	$2.59^{+0.05}_{-0.09}$	2.59[a]		2.33(3), 2.48(9), 2.41(2)[c]
$4^+_g \rightarrow 2^+_g$	$4.15^{+0.08}_{-0.27}$	4.12		3.74(5)[d]
$6^+_g \rightarrow 4^+_g$	$5.23^{+0.16}_{-0.15}$	5.14		5.00(11)[d]
$8^+_g \rightarrow 6^+_g$	$6.12^{+0.93}_{-0.32}$	5.92		5.66(21), ±5.93(24)[e]
$4^+_\gamma \rightarrow 2^+_\gamma$	$2.70^{+0.37}_{-0.08}$	2.45		
$6^+_\gamma \rightarrow 4^+_\gamma$	$4.56^{+0.22}_{-2.52}$	4.09		
$2^+_{K=0^+} \rightarrow 0^+_{K=0^+}$	$1.91^{+0.16}_{-0.18}$	2.28		
$4^+_{K=0^+} \rightarrow 2^+_{K=0^+}$	$3.07^{+0.40}_{-0.57}$	3.62		
Inter-band E2 transition matrix elements.				
$2^+_\gamma \rightarrow 0^+_g$	$0.32^{+0.01}_{-0.01}$	0.32[a]		±0.321(5)[f]
$2^+_\gamma \rightarrow 2^+_g$	$0.41^{+0.01}_{-0.01}$	0.40	0.38	>0.413[f]
$2^+_\gamma \rightarrow 4^+_g$	$0.09^{+0.01}_{-0.01}$	0.10	0.09	±0.09(1)[f]
$3^+_\gamma \rightarrow 2^+_g$	$-0.51^{+0.11}_{-0.03}$	-0.50		
$3^+_\gamma \rightarrow 4^+_g$	$-0.32^{+0.02}_{-0.07}$	-0.36		
$4^+_\gamma \rightarrow 2^+_g$	$0.14^{+0.01}_{-0.01}$	0.31	0.33	
$4^+_\gamma \rightarrow 4^+_g$	$-0.05^{+0.07}_{-0.07}$	0.59	0.57	
$4^+_\gamma \rightarrow 6^+_g$	$0.25^{+0.02}_{-0.02}$	0.21	0.17	
$6^+_\gamma \rightarrow 4^+_g$	$0.36^{+0.03}_{-0.27}$	0.31		
$6^+_\gamma \rightarrow 6^+_g$	$0.70^{+0.53}_{-0.54}$	0.70		
$0^+_{K=0^+} \rightarrow 2^+_g$	$0.04^{+0.01}_{-0.01}$	0.13	0.09	
$2^+_{K=0^+} \rightarrow 0^+_g$	$0.09^{+0.01}_{-0.01}$	0.12		±0.088(5)[f].
$2^+_{K=0^+} \rightarrow 2^+_g$	$-0.05^{+0.03}_{-0.03}$	-0.15	-0.11	$\lvert 0.04\rvert^{+0.03}_{-0.02}$[f]
$2^+_{K=0^+} \rightarrow 4^+_g$	$0.22^{+0.01}_{-0.02}$	0.22	0.14	±0.199(14)[f]
$4^+_{K=0^+} \rightarrow 2^+_g$	$0.33^{+0.01}_{-0.01}$	0.17	0.14	
$4^+_{K=0^+} \rightarrow 4^+_g$	$-0.96^{+0.04}_{-0.05}$	-0.19	-0.14	

[a] Reduced matrix element used for normalization in the IBA-1 calculations.
[b] Prediction of the Bohr and Mottelson model (BM) for the uncoupled reduced matrix elements.
[c] [111, 112, 113]
[d] [114]
[e] [114, 106]
[f] [106]

5.6 IBA-1 calculations

The programs PHINT and FBEM [115] were used to calculate reduced matrix elements under the framework of the IBA-1. The following parameters were used as input; PAIR=1.06 keV, ELL=17.08 keV, QQ=-21.23 keV, as found in Ref. [116]. The transition strength parameters were calculated from the data given in Table 5.3 and found to be E2SD=0.1565 eb and E2DD=-0.162 eb. Overall there is good agreement between the calculations of the IBA-1 and the measured values, the exception being the two 4^+ states of the γ and $K^\pi = 0^+$ bands.

An interesting feature of the IBA-1 model is the prediction of collective transitions between the γ and $K^\pi = 0^+$ bands. Interestingly, if the $K^\pi = 0^+$ band is interpreted as a β-vibrational band, transitions between the two different vibrational modes of motion are predicted to be zero under the collective model of Bohr and Mottelson, at odds with the predictions of the IBA-1 model. This was investigated by including an inter-band matrix element between the two bands based on the IBA-1 calculations, however no significant effect was observed.

5.7 Discussion

The ground-state band reduced matrix elements in general give good agreement with previous measurements, overlapping with at least one previous value within the $\sim 1\sigma$ limits. The determined $B(E2)$ value for the 2^+_g state is compared with other deformed Er nuclei in Fig. 5.7. It can be seen that the smooth trend of increasing $B(E2)$ values and decreasing energies continues with ^{170}Er. Here, the effect of the target position on the ground-state band reduced matrix elements was also investigated in further detail. The simulated hit pattern in Fig. 5.1 suggests that the target may be $\sim$1.1 mm off center or that the target is tilted slightly. The effect of a possible offset in the position on the ground-state band reduced matrix elements was investigated and found to decrease the matrix element values by only $\sim 2\%$.

The 0^+ and 2^+ transitions to the ground-state band from the $K^\pi = 0^+$ band are in excellent agreement with previous measurements and are generally well described by the collective model of Bohr and Mottelson. There are however large deviations for the reduced matrix elements of the 4^+ state. The $4^+_{K=0^+} \rightarrow 4^+_g$ transition is enhanced significantly with a reduced transition probability of $\sim$18(2) W.u. The enhancement is possibly related to the mixing with the nearby 4^+ state in the γ band. The extrapolated $E2/M1$ mixing ratio for this state, based on the $2^+_{K=0^+} \rightarrow 2^+_g$ reduced matrix element of $0.1^{+0.01}_{-0.01}\ u_N$, is $|2.67|^{+0.19}_{-0.26}$, in excellent agreement with the

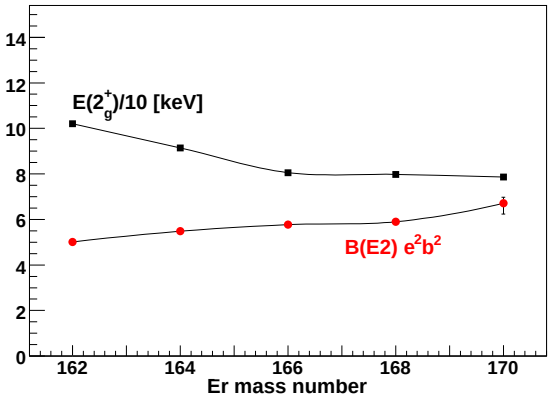

Figure 5.7: Energies and $B(E2)$ values of the 2^+ ground states in the deformed Er nuclei. The experimental point for ^{170}Er is from the current work.

previously reported value of +2.81(10) [117].

All the γ-band reduced matrix elements are well described by the coupling scheme of the Bohr and Mottelson model with the exception of the 4^+_γ state. As already mentioned, the possible reason for the deviation may be related to mixing with the 4^+ state in the $K^\pi = 0^+$ band. The $4^+_\gamma \rightarrow 4^+_g$ transition deviates significantly from the Bohr and Mottelson and IBA-1 predictions. The corresponding reduced matrix element in the nearby nucleus ^{168}Er is 0.72(2) eb [118]. The small value of the $E2$ transition strength and the measured branching ratios for this level indicate a strong $M1$ transition in ^{170}Er. The GOSIA value at the minimum was found to be -0.18$^{+0.02}_{-0.01}$ μ_N, yielding an $E2/M1$ mixing ratio of 0.23$^{+0.27}_{-0.30}$. Three values have been previously reported as -1.29$^{+0.07}_{-0.12}$, -4.3$^{+2.3}_{-9.9}$, and -9.8$^{+2.2}_{-6.3}$ [106]. Part of the difficulty in measuring the mixing ratio may be related to the presence of a nearby γ-ray line. In this case, possibly the 861 keV $6^+_\gamma \rightarrow 6^+_g$ transition.

It was also found that in-band reduced $M1$ matrix elements of $2.46^{+0.55}_{-0.19}$ μ_N and $3.28^{+0.52}_{-1.11}$ μ_N were needed for the $4^+_\gamma \rightarrow 3^+_\gamma$ and $6^+_\gamma \rightarrow 5^+_\gamma$ transitions, respectively, in order reproduce the observed intensities. The analysis was not sensitive to the reduced $E2$ matrix elements for these states. Extrapolation based on the $4^+_\gamma \rightarrow 2^+_g$ $E2$ reduced matrix element leads to an $E2/M1$ mixing ratio near zero for these transitions, suggesting pure $M1$ character. However, it should be noted that as the analysis was not directly sensitive to the reduced $E2$ matrix elements, this approach may not be valid,

especially in light of band mixing with the $K^\pi = 0^+$ band. Little information exists in the literature on the $E2/M1$ mixing ratios for in-band transitions. Measurements of such transitions are difficult due to their relatively weak intensities combined with the fact that they occur in a region of high γ-ray line density. Typically, these have been extracted assuming that the Alaga rules [119], which state that the reduced transition probabilities from a single state to two different final states are equal to the ratio of their Clebsch-Gordan coefficients squared, hold for the $E2$ components. The additional intensity is then ascribed to the $M1$ components and the mixing ratio can be deduced (see Eq. B.7 and Refs. [120, 121] for examples.). In Ref. [120], observation of three ΔI=-1 transitions in ^{168}Er was possible in conversion electron measurements. The measurements also suggested that the Alaga rules hold to a good approximation for the in-band transitions. Through comparison of their results with systematics of other rare-earth nuclei, it was concluded that the mixing ratio for these types of transitions had a nearly constant value of $\delta^2 \simeq 2.0$. This was supported by a theory proposed by Greiner [122] based on the rotation-vibration model. There still however remains several values which deviate from the expected theory and are close to zero, as shown in the tables contained in Refs. [120, 121]. Considering the above and the analysis presented in this work, it can be concluded that the current theory could benefit greatly from new measurements aimed at collecting high quality data for in-band and inter-band transitions of low-lying excitations, especially in regions where band-mixing effects may be present.

Chapter 6

The Lund R^3B calorimeter prototype

The development of new detector equipment provides experimentalists with more sensitive probes of nuclear structure. At the current date, a new radioactive ion beam facility is being built in Germany, known as FAIR [123]. One of the main experiments to take place at the new facility is known as R^3B [124]. The setup will be predominately used for nuclear reaction studies using relativistic radioactive ion beams. The target position of the experiment will be surrounded by a large CsI(Tl) crystal calorimeter called the CALorimeter for In-Flight emitted gAmmas (CALIFA) [125], which will contain several thousand detector elements. At Lund university, a small fifteen element version of the calorimeter was constructed and tested using a 180 MeV proton beam the The Svedberg Laboratory (TSL) [126]. The results were compared to simulations in order to evaluate the performance of the prototype. Of particular interest is the effects of inelastic interactions, multiple scattering, and the gain corrected summing procedure. This chapter is based on the work presented in Paper V.

6.1 The CALIFA calorimeter

The CALIFA calorimeter will be placed at the target position of the upcoming R^3B experiment at the FAIR facility. The technical design of the system is described in detail in the technical status report [125]. A brief overview of the requirements, relevant for the experimental tests and simulations is discussed in the following. The calorimeter will be used to detect both γ

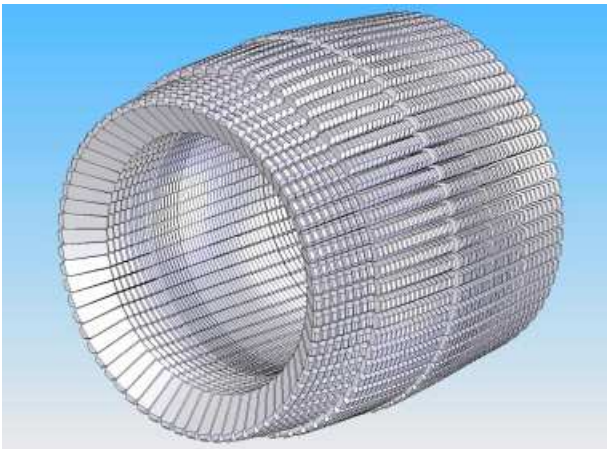

Figure 6.1: A schematic of the CALIFA barrel section. Reprinted from Ref. [127] with permission from Elsevier.

rays and light charged particles emitted in nuclear reactions with relativistic radioactive beams. The aim is to measure γ rays up to 15 MeV with an efficiency of 80% and light charged particles, i.e. protons, up to 300 MeV. The energy resolution for γ rays at 1 MeV should be $\sim$5%.

The analysis of nuclear reaction experiments using relativistic beams requires event-by-event Doppler correction. Thus, it is important to know as precisely as possible the interaction point of a γ ray. For this reason, the CALIFA calorimeter will ultimately consist of between $\sim$4000-5000 detector elements. The polar angle coverage of the detector will be 7^o-133^o divided into three primary subsections: the forward and end caps, and the barrel section. The shapes and sizes of the crystals used in the different regions of the calorimeter will be selected based on the Lorentz boosted γ-ray energies. At larger polar angles, the Lorentz boost reduces the energies of the γ rays and thus shorter crystals can be used. At smaller polar angles, the Lorentz boost increases the energies and longer crystals will be needed in order to capture the resulting electromagnetic shower. A rendering of the calorimeter barrel is shown in Fig. 6.1.

The crystals in the barrel region will be CsI(Tl) scintillator crystals. Each crystal will be wrapped in a reflective foil in order to guide the emitted scintillation light to either an avalanche photodiode (APD), photodiode (PD), or photomultiplier (PM). In addition to the reflective wrapping material, support structures will also be used in order to hold small clusters of detectors in place. As discussed in the following, it is important that

the excess material between the detectors be minimized. A high energy γ ray or charged particle traversing the detector will deposit energy into a number of crystals. In order to find the true energy of the particle it is required to add up the energy signals from these crystals. Any material between the detector elements will absorb some energy and the gain corrected summing routine will produce the incorrect total energy.

A possible nuclear physics investigation using CALIFA might involve Coulomb dissociation, which is similar to the method of Coulomb excitation. The physics motivation for such an experiment is of a completely different nature than investigating the collectivity of low-lying nuclear excited states. Capture cross sections involving light charged particles are useful in understanding various nuclear astrophysics phenomena. For example, estimation of the ^{8}B solar neutrino flux is related to the ^{7}Be$(p,\gamma)^{8}$B reaction, which has been previously studied via Coulomb dissociation [128]. The Coulomb dissociation technique is based on the following reaction

$$\gamma + a \rightarrow b + c. \tag{6.1}$$

In this process, the Coulomb field of a nucleus serves as a source of virtual photons which leads to the breakup of a second nucleus. The radiative capture cross section can be calculated based on the Coulomb dissociation cross section.

6.2 Overview of the Lund prototype

The prototype, constructed at Lund University, is shown in Fig. 6.2. The prototype represents detector elements corresponding to the angles 38^{o}-84^{o} of the barrel region of CALIFA. Each crystal has the shape of the two truncated rectangular pyramids joined together. The length of the crystals is 130 mm, with a front area of 15×42 mm^2 and a back area of 10×30 mm^2. The light collected at the back surface of a crystal is read out using a PD with an area of 10×10 mm^2. The individual crystals are wrapped with ESR reflective foils [129], each with a thickness of 65 μm. In addition, Al foils equivalent to 10 μm of Mylar, were also placed in between each crystal to serve as additional protection against light crosstalk. The CsI(Tl) crystals, when received in their raw form, exhibit a smooth exponential decrease in the light output as a function of the distance from the readout area. Each crystal was therefore adjusted to have a more uniform response in light output before the in-beam proton tests. The light output non-uniformity was better than 0.6% after these adjustments.

Figure 6.2: Photograph of the Lund R^3B calorimeter prototype. Reprinted from Paper V with permission from Elsevier.

6.3 Experimental tests

The prototype detector was tested using 179.3 MeV protons at TSL. The beam energy was further reduced to an energy of 178.2 MeV by a stainless steal window and two 1 mm thick 60×60 mm^2 single-sided silicon strip detectors (SSSDs) placed in front of the prototype. The two SSSDs provided information on the profile of the proton beam, which had a beam spot of about 40 mm^2. The two SSSDs defined a hit pattern of pixels, as the strips of the back SSSD were perpendicular to the strips on the front SSSD. The count rate was around 100 counts per second. The detector sat on top of a moveable table which made it possible to center the beam onto the surface of each of the individual detector elements. The energy calibration of the detector elements was carried out by using a 25 mm thick Cu collimator, with an 8 mm diameter hole, which was placed in front of the two SSSDs. This provided a second energy point of 92.7 MeV for the energy calibration. The trigger condition during the experiment was a coincident signal in the two SSSDs.

An example of the measured proton spectrum for a single crystal during the experiment is shown in Fig. 6.3. Only protons which produced signals in the central pixel of the hit pattern, defined by the two SSSDs, were considered in the generation of the spectrum. In addition, the spec-

trum only includes events which produced signals in up to two detector elements. For events with multiplicity two, the scattering had to also occur in one of the adjacent crystals above or below the central one and thus only three crystals were used in this part of the analysis. Two different structures can be observed in the spectrum. The first is the peak around the primary beam energy, corresponding to multiplicity one events. Roughly 50% of the events lie under the peak. The second is the broad plateau at lower energies. The structure is composed of events which interacted inelastically in the crystal volume or were scattered elastically to another crystal. Inelastic events result in energy losses which cannot be fully recovered. Events which interact elastically can be recovered by adding back the signals from the surrounding crystals.

An example of the gain corrected summing procedure, for the case previously described, is shown in Fig. 6.4. The black line represents the spectrum without any condition on the event multiplicity. There is a struc-

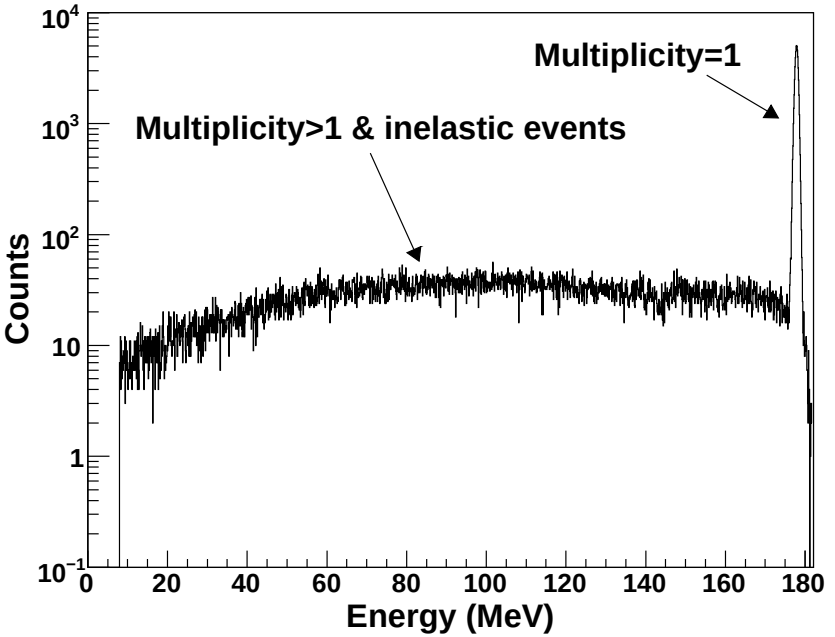

Figure 6.3: The measured proton energy spectrum in the central detector element from the TSL experiment.

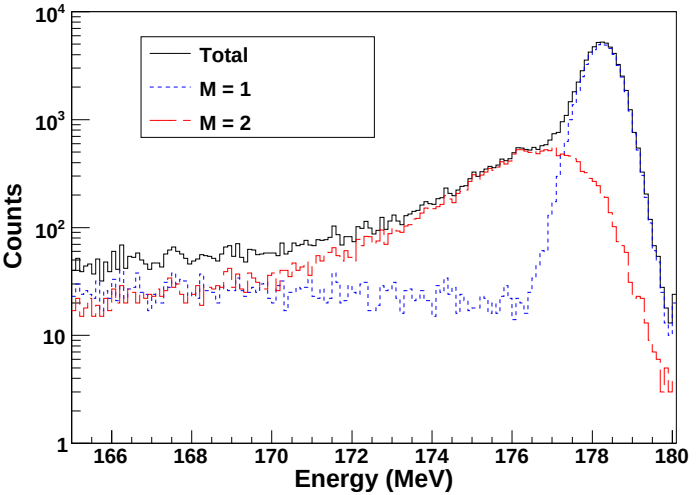

Figure 6.4: The proton energy spectrum for multiplicity one, multiplicity two, and the total of all event types. Reprinted and adapted from Paper V with permission from Elsevier.

ture appearing at lower energies than the full energy peak. The blue curve shows the events with only multiplicity one and the red curve shows the events with multiplicity two. The lower energy structure arises from events in which the protons were scattered between crystals. The effect is related to the energy loss in the matter between the crystals, as discussed and investigated with the simulations described in the next section.

6.4 Geant4 simulations of the prototype

The performance of the prototype was simulated using a Geant4/ROOT based program. The simulated prototype is shown in Fig. 6.5. The geometry of the prototype was input to the code, including all relevant matter between the crystals. The reflective foils used in the simulation were made up of Mylar ($C_5H_40_2$) and pure CsI was used for the crystals.

All the relevant electromagnetic physics processes were included in the simulation. For γ rays, this included the photoelectric effect, Compton and Raleigh scattering, and conversion. For electrons, these included Brem-

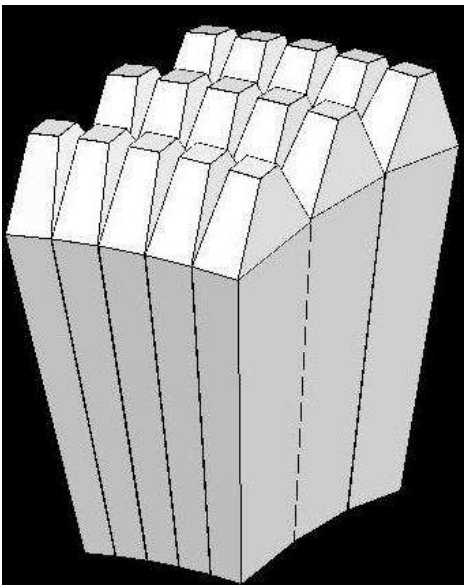

Figure 6.5: A graphical rendering the prototype used in the Geant4 simulations.

sthralung, positron annihilation, ionization, and multiple scattering. The low-energy extensions for these processes were used, which extends the energy range of the interactions down to ∼100 eV from the standard cut-off at 1 keV. The standard package was however used for the positron interactions. Two different physics lists were investigated for the hadronic interactions. The first used the binary cascade model [130]. The model treats the propagation of the primary hadron and secondaries in a nucleus as a series of two particle interactions. The second list tested was based on the Bertini intranuclear cascade [131]. The binary cascade model was ultimately used in the simulations, however no significant differences between the two physics lists were observed. After running the Geant4 simulations, the deposited energies in each crystal were broadened to meet the experimentally determined resolution for CsI(Tl)/APD systems, given by

$$R(\%) = 5.15/\sqrt{E(MeV)}. \tag{6.2}$$

The formula is the result of a compilation of data from CsI(Tl)/APD experiments combined with the results of the resolution measurements presented in Paper V.

The simulated spectra for multiplicity one and two events for the sit-

uation described in the experimental test section is shown in Fig. 6.6. A very similar pattern, as seen in the experimental data, is observed in the spectrum. The multiplicity one events are contained within the full energy peak while the multiplicity two events lie in a structure just shifted to lower energies. Further analysis reveals that the missing energy can be contributed to protons scattering between the two crystals. This was confirmed by adding back the energy deposited in the wrapping, which resulted in the full energy being recovered. The procedure is highlighted in Fig. 6.7, where the black curve represents the energy lost in the wrapping. Furthermore, the simulated energy loss in the wrapping is shown in Fig. 6.8 for electrons and protons. Electrons only contribute a small fraction of the energy loss compared to protons. The material between the crystals has little to or no effect on γ-ray events, as shown in the simulated spectra in Fig. 6.9 for two different energies. The simulated spectra with and without the foils are nearly identical. The proton energy loss in the reflective foils can of course be made smaller by using thinner foils between the crystals. The effect of using thinner foils is illustrated in Fig. 6.10 for multiplicity two events. When no foil is between the crystals, a symmetric full energy peak is observed. However, for thinner foils the peak remains asymmetric and is always shifted to lower energies.

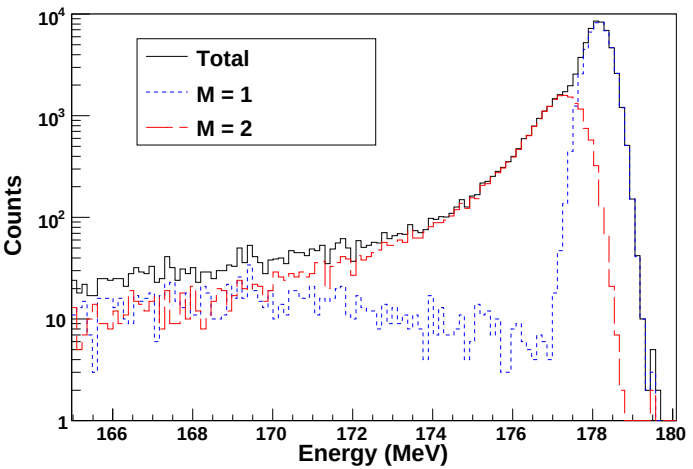

Figure 6.6: Gain corrected sum spectrum for the Geant4 proton simulations and spectra for the different multiplicity events. Reprinted and adapted from Paper V with permission from Elsevier.

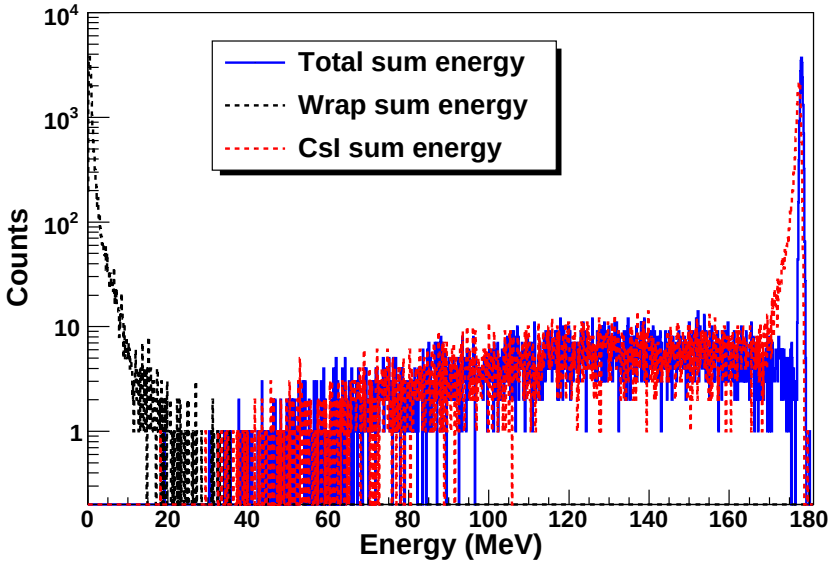

Figure 6.7: The sum spectra including the energy loss in the wrapping. The full energy can be recovered by considering this energy loss.

6.5 Inelastic and elastic events

One of the important design issues for CALIFA is the maximum possible efficiency of the system. This depends on the number of unrecoverable events, i.e. those lost to inelastic reactions, and the number of recoverable events, i.e. those which can be added back to the full energy peak after implementing gain corrected summing. The latter depends on the shapes and sizes of the crystals used in the detector. This issue has been explored through an ideal gain corrected summing scenario and the results are presented in Fig. 6.11. The unrecoverable events have been estimated by simulations using a block of CsI, which could be considered infinite in size compared to the shape of a standard CALIFA crystal. Those events which fall outside of the full energy peak are deemed unrecoverable. The maximum number of recoverable events is then estimated by comparing the number of events in the full energy peak of the infinite block simulations

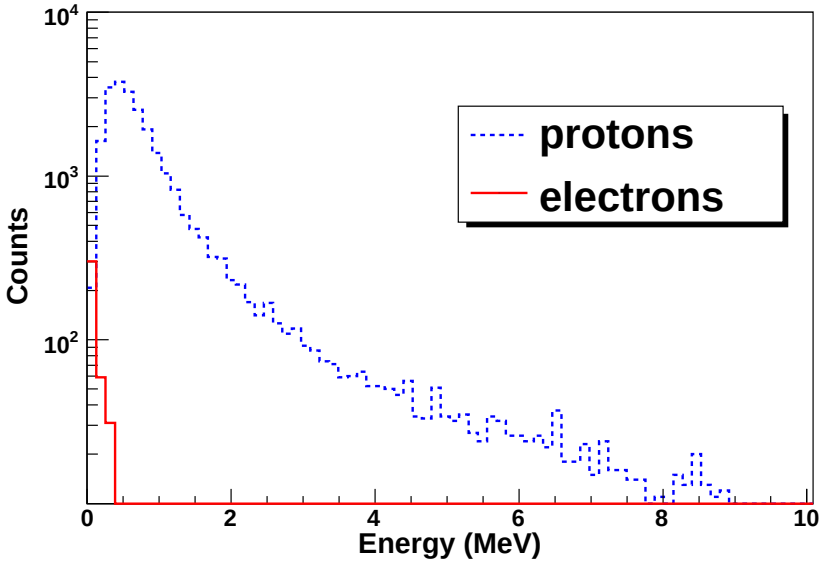

Figure 6.8: Simulated energy loss in the wrapping due to protons and electrons.

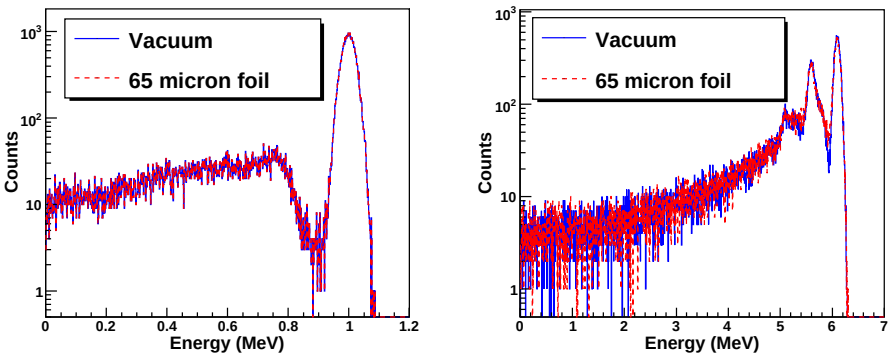

Figure 6.9: Geant4 simulations of γ rays with and without the reflective foils between the crystals.

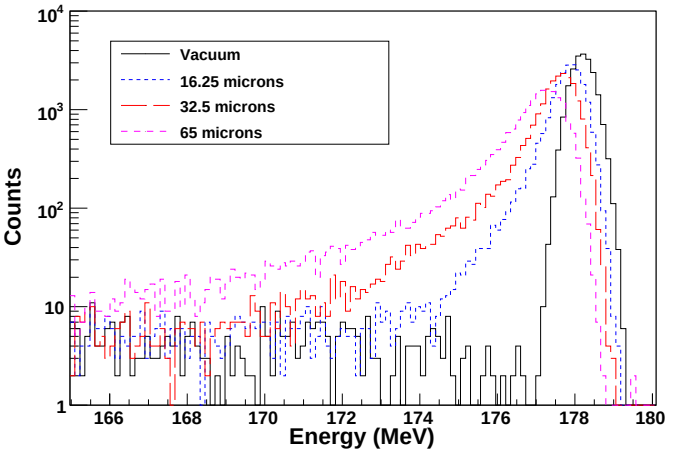

Figure 6.10: Effect of changing the foil thickness on the multiplcity two spectrum. Reprinted and adapted from Paper V with permission from Elsevier.

to the full energy peak of a simulation using a crystal representative of the CALIFA type. As an example, at 200 MeV 42% of the events are contained within the full energy peak of a standard CALIFA crystal. When simulating with an infinite block, the full energy peak contains 76% of the events, yielding an add back factor of 34%. The remaining 24% of the events are lost to inelastic processes. The losses become even more severe at higher energies. At 300 MeV, no protons lose their full energy in a single crystal and only 60% of the events can be recovered by gain corrected summing.

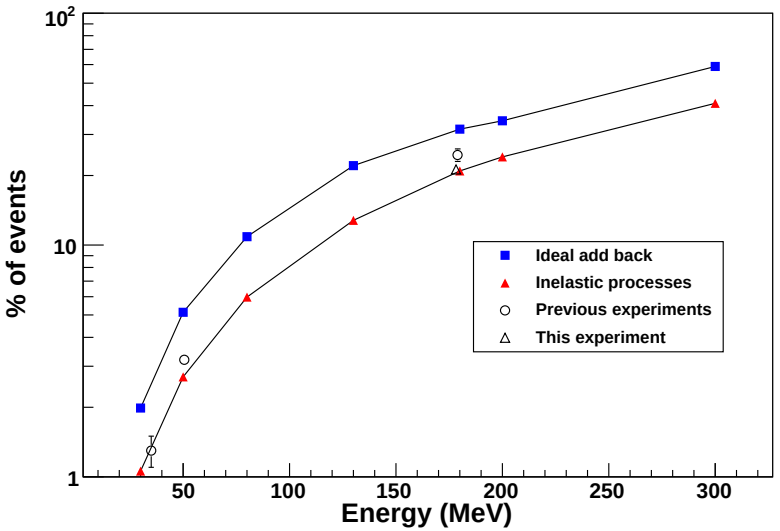

Figure 6.11: The percentage of unrecoverable and recoverable events for crystals of the CALIFA barrel. Reprinted and adapted from Paper V with permission from Elsevier.

Chapter 7

Summary and Outlook

A series of Coulomb excitation measurements were performed using both radioactive and stable ion beams. The radioactive ion beam experiments were carried out at the REX-ISOLDE facility at CERN and at the fragment recoil separator at GSI. The experiments were aimed at studying the properties of low-lying excited states in nuclei near the doubly magic nucleus ^{100}Sn. They were primarily motivated by two previous interesting physics cases: the unexpected increased transition strengths, relative to shell-model calculations, of the 2^+ states in the neutron-deficient Sn isotopes and also the location of the single-neutron states relative to ^{100}Sn. The two studies are complimentary to each other as the single-neutron states relative to ^{100}Sn are important input parameters for shell-model calculations. This was indicated in the results of the ^{107}Sn experiment as the calculated transition probabilities were sensitive to the placement of the single-neutron states. In general, the measured transition probabilities were underestimated by the shell-model calculations and collective models were instead found to give a better overall reproduction of the results. These findings, in combination with the previous measurements in the even-even Sn nuclei, point towards missing degrees of freedom in the shell-model calculations. One possibility is the lack of proton and neutron excitations across the $N = Z = 50$ shell gap.

Another interesting question regarding the transition strengths is the continuing trend towards ^{100}Sn (see Fig. 1.2) and whether or not the transition probabilities stay level around midshell values or decrease as expected. One of the aims of the ^{104}Sn experiment was to investigate this question. The above mentioned studies attempt to address some of the fundamental assumptions of the nuclear shell model near the doubly magic nucleus ^{100}Sn. Future plans are being made to remeasure and investigate

higher-lying transition probabilities in the neutron-deficient Sn isotopes. Another possibility is to continue the march towards ^{100}Sn and measure the transition probability of the first excited state in ^{102}Sn.

While radioactive ion beam experiments are much of the focus of modern day nuclear structure experiments, there is still much left unexplored in stable isotopes. The stable ion beam experiment presented in this was carried out on the nucleus ^{170}Er. The aim was to use Coulomb excitation to search for new excited states and also to explore the interactions of various low-lying structures in this nucleus. The search for excited states is related to the possible existence of two-phonon γ-vibrational bands, which have been identified in ^{166,168}Er. Exploring these states in other Er nuclei would provide a very interesting picture of how the two-phonon γ-vibrational excitation evolves with neutron number. The other interesting feature of ^{170}Er is the presence of two low-lying rotational bands at nearly the same energy. Because of their closeness in energy, they interact strongly, as also indicated by the measured deviations in the reduced transition probabilities from the predictions of the collective model of Bohr and Mottelson. A possible extension of this study is to repeat the measurement with the aim of obtaining higher statistics in order to observe the low-energy transitions between and within the rotational bands. This information would provide firmer constraints for the band mixing and also details on the $E2/M1$ mixing ratios for these types of transitions.

As already mentioned, technological advancements have paved the way for the recent progress in nuclear structure physics with radioactive ion beams. The last study presented in this thesis is related to the development of a new detector to be used in relativistic radioactive ion beam experiments. A small version of the detector, to be placed around the target position at the upcoming R^{3}B experiment, was built and tested using proton beams. The results were compared with simulations and design constraints, relevant for the construction of CALIFA, were discovered. These results will provide important information for the ongoing discussions regarding the design of the detector system.

Chapter 8

Popular summary in Swedish

Atomer är de grundläggande byggstenarna för alla material runt omkring oss. Varje enskild atom består av ett tätt packat område i centrum, som kallas atomkärnan, omgivet av ett moln av elektroner. Atomkärnan innehåller neutroner och protoner, hopbundna av den starka kärnkraften. Vissa kombinationer av neutroner och protoner leder till bildandet av kärnor som är stabila medan andra förhållanden leder till kärnor som är instabila och därmed radioaktiva. Den största delen av världen runt omkring oss består av de stabila kärnorna och därmed är kunskap om deras egenskaper omfattande. Dessa kärnor har studerats i detalj sedan början av kärnfysiken, omkring 1900. Sammantaget uppgår denna grupp till ungefär 300 stabila kärnor, vilket bara är en bråkdel jämfört med några tusen instabila kärnor som har observerats i laboratorier och som väntar på att bli upptäckta. Dessa kärnor är svårare att studera i laboratorier på grund deras korta livstider. Ett av de viktigaste målen med kärnfysik idag är att utforska dessa instabila kärnor och förstå deras egenskaper.

Denna avhandling kretsar kring en serie experiment samt utveckling av detektorer relaterade till atomkärnstruktur. Studien av kärnstruktur handlar om hur de grundläggande egenskaper av en atomkärna, till exempel dess massa eller excitationsnivåer, härrör från neutroner och protoner och interaktionerna dem emellan. För att förstå dessa typer av egenskaper, har kärnfysiker utvecklat ett stort antal modeller, främst baserade på information från gruppen av stabila kärnor. En intressant fråga att ställa är om dessa modeller är fullständiga och i så fall hur de står sig mot nya observationer av egenskaper i instabila kärnor. Först nyligen har detta gjorts möjligt genom ett antal tekniska framsteg i den experimentella

kärnfysiken.

Fyra olika experimentella undersökningar har genomförts i denna avhandling. De första två studierna handlar om instabila kärnor nära ^{100}Sn medan den tredje studien omfattar den stabila kärnan ^{170}Er. Målet för var och en av studierna var att mäta egenskaper som aldrig tidigare observerats samt att jämföra resultaten med moderna kärnstruktursmodeller. Den sista studien i denna avhandling är relaterad till utvecklingen av ny detektorutrustning som skall användas i framtida anläggningar för studier av instabila kärnor.

Acknowledgments

This thesis represents the culmination and end of a roughly five year journey as a PhD student. My journey was supported by a number of individuals who contributed to various aspects of the work. Foremost, I would like to thank my supervisor Joakim Cederkäll for his continuous encouragement and support. You were always available to discuss any part of the work and provided much needed criticism and guidance. I also truly appreciated the effort to make me feel welcome in Sweden, particularly in the beginning of my studies.

My sincere thanks also goes to my second supervisor Claes Fahlander for providing important feedback and whose continuous enthusiasm was a source of motivation for me.

I would like to also say thank you to Pavel Golubev, Vladimir Avdeichikov, Bo Jakobsson, and Dirk Rudolph for their encouragement and insightful discussions.

Finally, I would like to extend the thanks to all other members of the nuclear physics division at Lund University. I have always felt very welcome in the division and appreciated the pleasant working environment.

Appendix A
Two-body kinematics

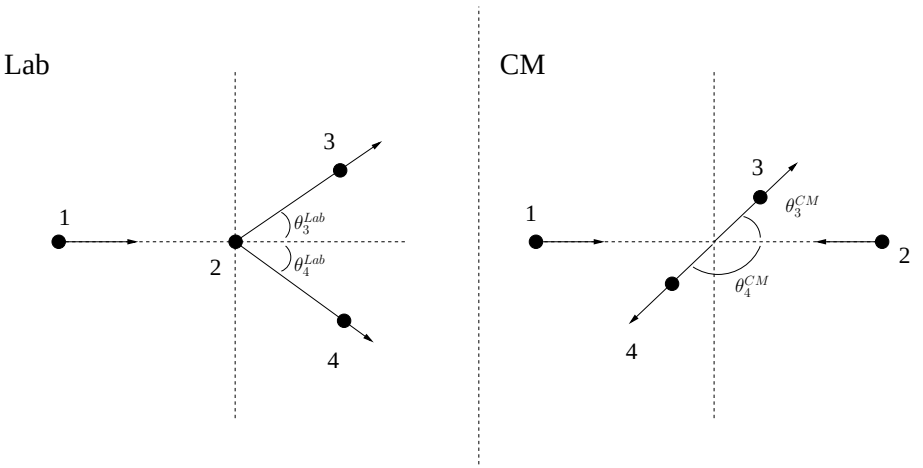

Figure A.1: Two-body kinematics in the lab and center-of-mass (CM) frame of reference.

For two-body elastic reactions occurring at non-relativistic energies, the available energy in the center-of-mass (CM) frame T_{Tot}^{CM} is related to the projectile energy T_1^{Lab} by

$$T_{Tot}^{CM} = \frac{M_2}{M_1 + M_2} T_1^{Lab}, \tag{A.1}$$

where M denotes the relevant particle mass. The energies of the particles in the CM frame, with $M1 = M3$ and $M2 = M4$, can be expressed in terms

of this energy, given as

$$T_{1,3}^{CM} = \frac{M2}{M1+M2} T_{Tot}^{CM}, \tag{A.2}$$

and

$$T_{2,4}^{CM} = \frac{M1}{M1+M2} T_{Tot}^{CM}. \tag{A.3}$$

The CM and laboratory scattering angles for the particles are related by

$$\tan\theta_3^{Lab} = \frac{\sin\theta_3^{CM}}{\cos\theta_3^{CM} + K}, \tag{A.4}$$

where $K = M1/M2$, or alternatively,

$$\cos\theta_3^{CM} = [\cos^2\theta_3^{Lab}(1 - K^2\sin^2\theta_3^{Lab})]^{1/2} - K\sin^2\theta_3^{Lab}, \tag{A.5}$$

and

$$\theta_4^{Lab} = \theta_4^{CM}/2. \tag{A.6}$$

The energies of the scattered particles in the lab frame are given by

$$T_3^{Lab} = \frac{M_2^2}{(M_1+M_2)^2} T_1^{Lab}\left[1 + \frac{M_1^2}{M_2^2} + 2\frac{M_1}{M_2}\cos\theta_3^{CM}\right], \tag{A.7}$$

and

$$T_4^{Lab} = \frac{4M_1M_2}{(M_1+M_2)^2} T_1^{Lab}\cos\theta_4^{Lab}. \tag{A.8}$$

For reactions in inverse kinematics, there exists a maximum scattering angle for the scattered projectile, given by

$$\theta_3^{Lab,MAX} = \sin^{-1}\left(\frac{M2}{M1}\right). \tag{A.9}$$

A detailed and thorough overview of the formulas presented here is given in Ref. [132].

Appendix B
Electromagnetic transitions

The mean lifetime of a decaying state is equal to the inverse of the transition probability, which is given by

$$T(\mathcal{O}\lambda; I_i \rightarrow I_f) = \frac{8\pi(\lambda+1)}{\lambda[(2\lambda+1)!!]^2}\frac{1}{\hbar}(q)^{2\lambda+1}B(\mathcal{O}\lambda; I_i \rightarrow I_f), \tag{B.1}$$

where $\mathcal{O}$ denotes either an electric or magnetic transition, λ is the multipolarity of the transition, I_i is the initial state spin, and I_f is the final state spin. The reduced transition probability is related to the reduced matrix element for a transition by

$$B(\mathcal{O}\lambda; I_i \rightarrow I_f) = \frac{1}{2I_i+1}|\langle I_f||\mathcal{M}(\mathcal{O}\lambda)||I_i\rangle|^2. \tag{B.2}$$

The quantity q is given by

Table B.1: Weisskopf single-particle units. The downward reduced transition probabilities are typically given in the literature. Units are in e^2b^λ or $\mu_N^2 b^{\lambda-1}$.

Electric	Magnetic
$B(E1)_W = 6.45 \times 10^{-4}A^{2/3}$	$B(M1)_W = 1.79$
$B(E2)_W = 5.94 \times 10^{-6}A^{4/3}$	$B(M2)_W = 1.65 \times 10^{-2}A^{2/3}$
$B(E3)_W = 5.94 \times 10^{-8}A^{2}$	$B(M3)_W = 1.65 \times 10^{-4}A^{4/3}$
$B(E4)_W = 6.29 \times 10^{-10}A^{8/3}$	$B(M4)_W = 1.75 \times 10^{-6}A^{2}$

$$q = \frac{w}{c} = \frac{E(MeV)}{197.329\ MeV \cdot fm}. \tag{B.3}$$

The units for the reduced transition probabilities are typically given in e^2b^λ or $e^2fm^{2\lambda}$ for electric transitions and $\mu_N^2 b^{\lambda-1}$ or $\mu_N^2 fm^{2\lambda-2}$ for magnetic transitions, where 1 b = 100 fm^2. The transition probabilities are also frequently given in single-particle Weisskopf units, i.e.

$$B_W(E\lambda) = \frac{(1.2)^{2\lambda}}{4\pi}\left(\frac{3}{\lambda+3}\right)^2 A^{2\lambda/3} e^2 fm^{2\lambda}, \tag{B.4}$$

for electric transitions and

$$B_W(M\lambda) = \frac{10(1.2)^{2\lambda-2}}{\pi}\left(\frac{3}{\lambda+2}\right)^2 A^{(2\lambda-2)/3} \mu_N^2 fm^{2\lambda-2}, \tag{B.5}$$

for magnetic transitions. These formulas are summarized in Table B.1 for commonly encountered types of transitions.

The $E2/M1$ mixing ratio for an electromagnetic decay is given by

$$\delta = 0.835 E_\gamma(MeV) \frac{\langle I_i || \mathcal{M}(E2) || I_f \rangle}{\langle I_i || \mathcal{M}(M1) || I_f \rangle}. \tag{B.6}$$

The transition probability branching ratio for a state is related to the mixing ratio by

$$\frac{B(E2, I_i \to I_{f1})}{B(E2, I_i \to I_{f2})} = \frac{I_\gamma(I_i \to I_{f1})}{I_\gamma(I_i \to I_{f2})}\left(\frac{E_\gamma(I_i \to I_{f2})}{E_\gamma(I_i \to I_{f1})}\right)^5 \frac{\delta^2}{1+\delta^2}, \tag{B.7}$$

where $\frac{\delta^2}{1+\delta^2}$ denotes the $E2$ fraction of the decay, I_γ is the intensity of the γ ray, E_γ is its energy, and $f1$ and $f2$ denote two different final states.

Appendix C
Two-body matrix elements

The tables on the following pages list the two-body matrix elements (ME) used in the ^{107,109}Sn calculations. They were generated using a CD-Bonn potential and the G-matrix renormalization procedure with ^{100}Sn as the core. The matrix elements are given in MeV, n is the radial quantum number, l is the orbital angular momentum, j is the total angular momentum for the orbit, T is the isospin, and J is the coupled angular momentum.

Table C.1: Two-body matrix elements used in the Sn shell-model calculations.

n_1	l_1	j_1	n_2	l_2	j_2	n_3	l_3	j_3	n_4	l_4	j_4	$2T$	$2J$	ME
0	4	7	0	4	7	0	4	7	0	4	7	2	0	-1.30725
0	4	7	0	4	7	1	2	5	1	2	5	2	0	-0.64045
0	4	7	0	4	7	1	2	3	1	2	3	2	0	-0.65732
0	4	7	0	4	7	2	0	1	2	0	1	2	0	-0.31608
0	4	7	0	4	7	0	5	11	0	5	11	2	0	1.34930
1	2	5	1	2	5	1	2	5	1	2	5	2	0	-0.87671
1	2	5	1	2	5	1	2	3	1	2	3	2	0	-1.06409
1	2	5	1	2	5	2	0	1	2	0	1	2	0	-0.44930
1	2	5	1	2	5	0	5	11	0	5	11	2	0	0.89184
1	2	3	1	2	3	1	2	3	1	2	3	2	0	-0.43865
1	2	3	1	2	3	2	0	1	2	0	1	2	0	-0.37591
1	2	3	1	2	3	0	5	11	0	5	11	2	0	0.62290
2	0	1	2	0	1	2	0	1	2	0	1	2	0	-0.90313
2	0	1	2	0	1	0	5	11	0	5	11	2	0	0.39533
0	5	11	0	5	11	0	5	11	0	5	11	2	0	-1.32242
0	4	7	1	2	5	0	4	7	1	2	5	2	2	-0.15771
0	4	7	1	2	5	1	2	5	1	2	3	2	2	-0.02257
0	4	7	1	2	5	1	2	3	2	0	1	2	2	-0.11204
1	2	5	1	2	3	1	2	5	1	2	3	2	2	0.00310
1	2	5	1	2	3	1	2	3	2	0	1	2	2	-0.02159
1	2	3	2	0	1	1	2	3	2	0	1	2	2	0.07821
0	4	7	0	4	7	0	4	7	0	4	7	2	4	-0.32776
0	4	7	0	4	7	0	4	7	1	2	5	2	4	-0.02699
0	4	7	0	4	7	0	4	7	1	2	3	2	4	-0.36070
0	4	7	0	4	7	1	2	5	1	2	5	2	4	-0.10691
0	4	7	0	4	7	1	2	5	1	2	3	2	4	-0.19988
0	4	7	0	4	7	1	2	5	2	0	1	2	4	-0.21036
0	4	7	0	4	7	1	2	3	1	2	3	2	4	-0.24387
0	4	7	0	4	7	1	2	3	2	0	1	2	4	0.13211
0	4	7	0	4	7	0	5	11	0	5	11	2	4	0.26657
0	4	7	1	2	5	0	4	7	1	2	5	2	4	0.03012
0	4	7	1	2	5	0	4	7	1	2	3	2	4	0.26818
0	4	7	1	2	5	1	2	5	1	2	5	2	4	0.07946
0	4	7	1	2	5	1	2	5	1	2	3	2	4	0.09525
0	4	7	1	2	5	1	2	5	2	0	1	2	4	0.08818

Table C.2: Two-body matrix elements used in the Sn shell-model calculations.

n_1	l_1	j_1	n_2	l_2	j_2	n_3	l_3	j_3	n_4	l_4	j_4	$2T$	$2J$	ME
0	4	7	1	2	5	1	2	3	1	2	3	2	4	0.02471
0	4	7	1	2	5	1	2	3	2	0	1	2	4	-0.09958
0	4	7	1	2	5	0	5	11	0	5	11	2	4	-0.28697
0	4	7	1	2	3	0	4	7	1	2	3	2	4	-0.44810
0	4	7	1	2	3	1	2	5	1	2	5	2	4	-0.18774
0	4	7	1	2	3	1	2	5	1	2	3	2	4	-0.19679
0	4	7	1	2	3	1	2	5	2	0	1	2	4	-0.25174
0	4	7	1	2	3	1	2	3	1	2	3	2	4	-0.21454
0	4	7	1	2	3	1	2	3	2	0	1	2	4	0.29969
0	4	7	1	2	3	0	5	11	0	5	11	2	4	0.41660
1	2	5	1	2	5	1	2	5	1	2	5	2	4	-0.31338
1	2	5	1	2	5	1	2	5	1	2	3	2	4	-0.12866
1	2	5	1	2	5	1	2	5	2	0	1	2	4	-0.34963
1	2	5	1	2	5	1	2	3	1	2	3	2	4	-0.23709
1	2	5	1	2	5	1	2	3	2	0	1	2	4	0.28786
1	2	5	1	2	5	0	5	11	0	5	11	2	4	0.41598
1	2	5	1	2	3	1	2	5	1	2	3	2	4	-0.06419
1	2	5	1	2	3	1	2	5	2	0	1	2	4	-0.15827
1	2	5	1	2	3	1	2	3	1	2	3	2	4	-0.27314
1	2	5	1	2	3	1	2	3	2	0	1	2	4	0.27125
1	2	5	1	2	3	0	5	11	0	5	11	2	4	0.03334
1	2	5	2	0	1	1	2	5	2	0	1	2	4	-0.51766
1	2	5	2	0	1	1	2	3	1	2	3	2	4	-0.27061
1	2	5	2	0	1	1	2	3	2	0	1	2	4	0.56056
1	2	5	2	0	1	0	5	11	0	5	11	2	4	0.23265
1	2	3	1	2	3	1	2	3	1	2	3	2	4	-0.00263
1	2	3	1	2	3	1	2	3	2	0	1	2	4	0.16208
1	2	3	1	2	3	0	5	11	0	5	11	2	4	0.10782
1	2	3	2	0	1	1	2	3	2	0	1	2	4	-0.21823
1	2	3	2	0	1	0	5	11	0	5	11	2	4	-0.23522
0	5	11	0	5	11	0	5	11	0	5	11	2	4	-0.73887
0	4	7	1	2	5	0	4	7	1	2	5	2	6	0.13919
0	4	7	1	2	5	0	4	7	1	2	3	2	6	0.08885
0	4	7	1	2	5	0	4	7	2	0	1	2	6	-0.12909
0	4	7	1	2	5	1	2	5	1	2	3	2	6	-0.03444
0	4	7	1	2	5	1	2	5	2	0	1	2	6	-0.03823

Table C.3: Two-body matrix elements used in the Sn shell-model calculations.

n_1	l_1	j_1	n_2	l_2	j_2	n_3	l_3	j_3	n_4	l_4	j_4	$2T$	$2J$	ME
0	4	7	1	2	3	0	4	7	1	2	3	2	6	0.15316
0	4	7	1	2	3	0	4	7	2	0	1	2	6	-0.12305
0	4	7	1	2	3	1	2	5	1	2	3	2	6	-0.00973
0	4	7	1	2	3	1	2	5	2	0	1	2	6	-0.00326
0	4	7	2	0	1	0	4	7	2	0	1	2	6	0.16408
0	4	7	2	0	1	1	2	5	1	2	3	2	6	-0.00015
0	4	7	2	0	1	1	2	5	2	0	1	2	6	0.02580
1	2	5	1	2	3	1	2	5	1	2	3	2	6	0.08739
1	2	5	1	2	3	1	2	5	2	0	1	2	6	-0.04968
1	2	5	2	0	1	1	2	5	2	0	1	2	6	-0.00366
0	4	7	0	4	7	0	4	7	0	4	7	2	8	0.09797
0	4	7	0	4	7	0	4	7	1	2	5	2	8	0.10194
0	4	7	0	4	7	0	4	7	1	2	3	2	8	-0.24836
0	4	7	0	4	7	0	4	7	2	0	1	2	8	0.10916
0	4	7	0	4	7	1	2	5	1	2	5	2	8	-0.07943
0	4	7	0	4	7	1	2	5	1	2	3	2	8	-0.22296
0	4	7	0	4	7	0	5	11	0	5	11	2	8	0.15756
0	4	7	1	2	5	0	4	7	1	2	5	2	8	0.11574
0	4	7	1	2	5	0	4	7	1	2	3	2	8	0.18166
0	4	7	1	2	5	0	4	7	2	0	1	2	8	-0.30149
0	4	7	1	2	5	1	2	5	1	2	5	2	8	0.08082
0	4	7	1	2	5	1	2	5	1	2	3	2	8	0.19039
0	4	7	1	2	5	0	5	11	0	5	11	2	8	-0.20582
0	4	7	1	2	3	0	4	7	1	2	3	2	8	0.06683
0	4	7	1	2	3	0	4	7	2	0	1	2	8	0.25560
0	4	7	1	2	3	1	2	5	1	2	5	2	8	-0.06078
0	4	7	1	2	3	1	2	5	1	2	3	2	8	-0.18832
0	4	7	1	2	3	0	5	11	0	5	11	2	8	0.14921
0	4	7	2	0	1	0	4	7	2	0	1	2	8	-0.08731
0	4	7	2	0	1	1	2	5	1	2	5	2	8	0.11798
0	4	7	2	0	1	1	2	5	1	2	3	2	8	0.24606
0	4	7	2	0	1	0	5	11	0	5	11	2	8	-0.20652
1	2	5	1	2	5	1	2	5	1	2	5	2	8	-0.05635
1	2	5	1	2	5	1	2	5	1	2	3	2	8	-0.39775
1	2	5	1	2	5	0	5	11	0	5	11	2	8	0.20784
1	2	5	1	2	3	1	2	5	1	2	3	2	8	-0.57846

Table C.4: Two-body matrix elements used in the Sn shell-model calculations.

n_1	l_1	j_1	n_2	l_2	j_2	n_3	l_3	j_3	n_4	l_4	j_4	$2T$	$2J$	ME
1	2	5	1	2	3	0	5	11	0	5	11	2	8	0.20218
0	5	11	0	5	11	0	5	11	0	5	11	2	8	-0.24599
0	4	7	1	2	5	0	4	7	1	2	5	2	10	0.19470
0	4	7	1	2	5	0	4	7	1	2	3	2	10	-0.00966
0	4	7	1	2	3	0	4	7	1	2	3	2	10	0.21475
0	4	7	0	4	7	0	4	7	0	4	7	2	12	0.25754
0	4	7	0	4	7	0	4	7	1	2	5	2	12	0.19129
0	4	7	0	4	7	0	5	11	0	5	11	2	12	0.10586
0	4	7	1	2	5	0	4	7	1	2	5	2	12	-0.36753
0	4	7	1	2	5	0	5	11	0	5	11	2	12	-0.27382
0	5	11	0	5	11	0	5	11	0	5	11	2	12	-0.06973
0	5	11	0	5	11	0	5	11	0	5	11	2	16	0.01564
0	5	11	0	5	11	0	5	11	0	5	11	2	20	0.07430
0	4	7	0	5	11	0	4	7	0	5	11	2	4	-0.77089
0	4	7	0	5	11	0	4	7	0	5	11	2	6	-0.35195
0	4	7	0	5	11	1	2	5	0	5	11	2	6	0.23051
1	2	5	0	5	11	1	2	5	0	5	11	2	6	-0.71995
0	4	7	0	5	11	0	4	7	0	5	11	2	8	-0.00406
0	4	7	0	5	11	1	2	5	0	5	11	2	8	0.08050
0	4	7	0	5	11	1	2	3	0	5	11	2	8	-0.14412
1	2	5	0	5	11	1	2	5	0	5	11	2	8	-0.02271
1	2	5	0	5	11	1	2	3	0	5	11	2	8	-0.17670
1	2	3	0	5	11	1	2	3	0	5	11	2	8	-0.13412
0	4	7	0	5	11	0	4	7	0	5	11	2	10	-0.07556
0	4	7	0	5	11	1	2	5	0	5	11	2	10	0.08841
0	4	7	0	5	11	1	2	3	0	5	11	2	10	-0.22542
0	4	7	0	5	11	2	0	1	0	5	11	2	10	0.12855
1	2	5	0	5	11	1	2	5	0	5	11	2	10	-0.12849
1	2	5	0	5	11	1	2	3	0	5	11	2	10	0.16971
1	2	5	0	5	11	2	0	1	0	5	11	2	10	-0.35912
1	2	3	0	5	11	1	2	3	0	5	11	2	10	0.01127
1	2	3	0	5	11	2	0	1	0	5	11	2	10	0.29659
2	0	1	0	5	11	2	0	1	0	5	11	2	10	-0.20178
0	4	7	0	5	11	0	4	7	0	5	11	2	12	0.12328
0	4	7	0	5	11	1	2	5	0	5	11	2	12	0.06460
0	4	7	0	5	11	1	2	3	0	5	11	2	12	-0.09441

Table C.5: Two-body matrix elements used in the Sn shell-model calculations.

n_1	l_1	j_1	n_2	l_2	j_2	n_3	l_3	j_3	n_4	l_4	j_4	$2T$	$2J$	ME
0	4	7	0	5	11	2	0	1	0	5	11	2	12	0.01293
1	2	5	0	5	11	1	2	5	0	5	11	2	12	0.16289
1	2	5	0	5	11	1	2	3	0	5	11	2	12	-0.00732
1	2	5	0	5	11	2	0	1	0	5	11	2	12	-0.16325
1	2	3	0	5	11	1	2	3	0	5	11	2	12	0.15870
1	2	3	0	5	11	2	0	1	0	5	11	2	12	-0.08249
2	0	1	0	5	11	2	0	1	0	5	11	2	12	0.10989
0	4	7	0	5	11	0	4	7	0	5	11	2	14	-0.11506
0	4	7	0	5	11	1	2	5	0	5	11	2	14	0.11561
0	4	7	0	5	11	1	2	3	0	5	11	2	14	-0.34373
1	2	5	0	5	11	1	2	5	0	5	11	2	14	-0.00365
1	2	5	0	5	11	1	2	3	0	5	11	2	14	0.33617
1	2	3	0	5	11	1	2	3	0	5	11	2	14	-0.40522
0	4	7	0	5	11	0	4	7	0	5	11	2	16	0.16996
0	4	7	0	5	11	1	2	5	0	5	11	2	16	0.05627
1	2	5	0	5	11	1	2	5	0	5	11	2	16	0.16803
0	4	7	0	5	11	0	4	7	0	5	11	2	18	-0.88081

Bibliography

[1] A. Bohr and B. Mottelson. *Nuclear Structure Vol. II*. W.A. Benjamin Inc., Reading, MA, USA, 1975.

[2] K. Alder et al. Study of Nuclear Structure by Electromagnetic Excitation with Accelerated Ions. *Rev. Mod. Phys.*, 28:432, 1956.

[3] Evaluated nuclear structure data file (ensdf). http://www.nndc.bnl.gov/ensdf/.

[4] D. Seweryniak et al. Single-Neutron States in ^{101}Sn. *Phys. Rev. Lett.*, 99:022504, 2007.

[5] I. G. Darby et al. Orbital Dependent Nucleonic Pairing in the Lightest Known Isotopes of Tin. *Phys. Rev. Lett.*, 105:162502, 2010.

[6] A. Banu et al. ^{108}Sn studied with intermediate-energy Coulomb excitation. *Phys. Rev. C*, 72:061305(R), 2005.

[7] J. Cederkäll et al. Sub-Barrier Coulomb Excitation of ^{110}Sn and Its Implications for the ^{100}Sn Shell Closure. *Phys. Rev. Lett.*, 98:172501, 2007.

[8] C. Vaman et al. Z=50 Shell Gap near ^{100}Sn from Intermediate-Energy Coulomb Excitations in Even-Mass $^{106-112}$Sn Isotopes. *Phys. Rev. Lett.*, 99:162501, 2007.

[9] A. Ekström et al. $0^+_{gs} \rightarrow 2^+_1$ Transition Strengths in ^{106}Sn and ^{108}Sn. *Phys. Rev. Lett.*, 101:12502, 2008.

[10] A. Jungclaus et al. Evidence for reduced collectivity around the neutron mid-shell in the stable even-mass Sn isotopes from new lifetime measurements. *Phys. Lett. B*, 695:110, 2011.

[11] L. C. Biedenharn and P. J. Brussaard. *Coulomb Excitation*. Clarendon press, Oxford, UK, 1965.

[12] M. Goeppert Mayer. On Closed Shells in Nuclei. II. *Phys. Rev.*, 75:1969, 1949.

[13] O. Haxel et al. On the "Magic Numbers" in Nuclear Structure. *Phys. Rev.*, 75:1766, 1949.

[14] R. F. Casten. *Nuclear structure from a simple perspective*. Oxford University Press, Oxford, UK, 2000.

[15] P. J. Brussaard and P. W. M. Glaudemans. *Shell-model applications in nuclear spectroscopy*. North-Holland Publishing Company, Amsterdam, Netherlands, 1977.

[16] R. Machleidt and D. R. Entem. Chiral effective field theory and nuclear forces. *Phys. Reports*, 503:1, 2011.

[17] R. Machleidt. High-precision, charge-dependent Bonn nucleon-nucleon potential. *Phys. Rev. C*, 63:024001, 2001.

[18] T. Engeland et al. Large Shell Model Calculations with Realistic Effective Interaction. *Phys. Scr. T*, 56:58, 1995.

[19] G. Racah. Theory of Complex Spectra. III. *Phys. Rev.*, 63:367, 1943.

[20] I. Talmi. *Simple Models of Complex Nuclei*. Harwood Academic Publishers, Switzerland, 1993.

[21] I. Talmi. Generalized seniority and structure of semi-magic nuclei. *Nucl. Phys. A*, 172:1, 1971.

[22] I. O. Morales et al. Generalized seniority and $E2$ transitions in the tin isotopes. *Phys. Lett. B*, 703:606, 2011.

[23] W. Greiner and J. Maruhn. *Nuclear Models*. Springer-Verlag Berlin Heidelberg, Germany, 1996.

[24] J. Eisenberg and W. Greiner. *Nuclear theory vol 1, Nuclear Models*. North-Holland Physics Publishing, Amsterdam, Netherlands, 1987.

[25] P. O. Lipas. Perturbation corrections to energies of collective states in deformed even nuclei. *Nucl. Phys. A*, 39:468, 1962.

[26] L. L. Riedinger et al. β- and γ-Vibrational Bands of ^{152}Sm and ^{154}Gd. *Phys. Rev.*, 179:1214, 1969.

[27] A. de-Shalit. Core Excitations in Nondeformed, Odd-A, Nuclei. *Phys. Rev.*, 122:1530, 1961.

[28] A. deShalit and H. Feshbach. *Theoretical nuclear physics, vol. 1*. John Wiley and Sons, Inc., New York, USA, 1974.

[29] K. Heyde et al. COEXISTENCE IN ODD-MASS NUCLEI. *Phys. Rep.*, 102:291, 1983.

[30] A. Arima and F. Iachello. Collective Nuclear States as Representations of a SU(6) Group. *Phys. Rev. Lett.*, 35:1069, 1975.

[31] R. F. Casten. Quantum phase transitions and structural evolution in nuclei. *Prog. Part. Nucl. Phys.*, 62:183, 2009.

[32] K. Alder and A. Winther. *Electromagnetic excitation*. North-Holland Publishing Company, Amsterdam, Netherlands, 1975.

[33] T. Czosnyka et al. *GOSIA Coulomb excitation codes*. User Manual, 2011.

[34] D. Cline. Nuclear Shapes Studied by Coulomb Excitation. *Annu. Rev. Nucl. Part. Sci.*, 36:683, 1986.

[35] L. D. Tolsma et al. Solving coupled equations by iteration for heavy ion multiple Coulomb excitation. *Phys. Rev. C*, 20:592, 1979.

[36] M. Ferentz and N. Rosenzweig. Table of F coefficients. Argonne National Laboratory Report No. ANL-5324, 1955.

[37] H. J. Rose and D. M. Brink. Angular Distributions of Gamma Rays in Terms of Phase-Defined Reduced Matrix Elements. *Rev. Mod. Phys.*, 39:306, 1967.

[38] A. N. F. Aleixo and C. A. Bertulani. Coulomb excitation in intermediate-energy collisions. *Nucl. Phys. A*, 505:448, 1989.

[39] T. Glasmacher. COULOMB EXCITATION AT INTERMEDIATE ENERGIES. *Annu. Rev. Nucl. Part. Sci.*, 48:1, 1998.

[40] A. Winther and K. Alder. Relativistic coulomb excitation. *Nucl. Phys. A*, 319:518, 1979.

[41] C. Rossi Alvarez. The GASP array. *Nucl. Phys. News*, 3:10, 1993.

[42] Laboratori Nazionali di Legnaro. http://www.lnl.infn.it/.

[43] REX-ISOLDE. http://isolde.web.cern.ch/isolde/rex-isolde/.

[44] O. Kester et al. Accelerated radioactive beams from REX-ISOLDE. *Nucl. Instrum. Methods Phys. Res. B*, 204:20, 2003.

[45] V. N. Fedoseyev et al. The ISOLDE laser ion source for exotic nuclei. *Hyp. Int.*, 127:409, 2000.

[46] F. Ames et al. Cooling of radioactive ions with the Penning trap REXTRAP. *Nucl. Instrum. Methods Phys. Res. A*, 538:17, 2005.

[47] F. Wenander. EBIS as charge breeder for radioactive ion beam accelerators. *Nucl. Phys. A*, 701:528, 2002.

[48] A. Ekström. *Effective charges in nuclei in the vicinity of* ^{100}Sn. PhD thesis, Lund University, 2009.

[49] A. N. Ostrowski et al. CD: A double sided silicon strip detector for radioactive nuclear beam experiments. *Nucl. Instrum. Methods Phys. Res. A*, 480:448, 2002.

[50] N. Warr et al. The Miniball Spectrometer. Submitted to Eur. Phys. J, 2012.

[51] The lund/LBNL nuclear data search. http://nucleardata.nuclear.lu.se/toi/.

[52] H. J. Wollersheim et al. Rare ISotopes INvestigation at GSI (RISING) using gamma-ray spectroscopy at relativistic energies. *Nucl. Instrum. Methods Phys. Res. A*, 537:637, 2005.

[53] H. Geissel et al. The GSI projectile fragment separator (FRS): a versatile magnetic system for relativistic heavy ions. *Nucl. Instrum. Methods Phys. Res. B*, 70:286, 1992.

[54] D. Rudolph et al. The Lund-York-Cologne CAlorimeter (LYCCA) Technical design report. Available at http://www.nuclear.lu.se/english/research/.

[55] Gsi helmholtzzentrum für schwerionenforschung. http://www.gsi.de/.

[56] J. -J. Gaimard and K. -H. Schmidt. A reexamination of the abrasion-ablation model for the description of the nuclear fragmentation reaction. *Nucl. Phys. A*, 531:709, 1991.

[57] Relativistic beams of exotic nuclei - a powerful tool for nuclear structure physics, gsi-nachrichten, 3/97. Available at http://www-w2k.gsi.de/frs/.

[58] R. Schneider. Tehnical Manual Ionisation Chamber MUSIC80. Available at http://www-w2k.gsi.de/frs/.

[59] R. Hoischen et al. Fast timing with plastic scintillators for in-beam heavy-ion spectroscopy. *Nucl. Instrum. and Methods. A*, 654:354, 2011.

[60] F. Schirru et al. Development of large area polycrystalline diamond detectors for fast timing application of high-energy heavy-ion beams. *JINST*, 7:P05005, 2012.

[61] N. Warr. Miniball electronics at may 2009. Unpublished, 2009.

[62] Digital gamma finder (DGF-4C Revision D). http://www.xia.com/.

[63] S. L. Thomas et al. A modular amplifier system for the readout of silicon strip detectors. *Nucl. Instrum. Meth. A*, 288:212, 1990.

[64] T. Davinson et al. Development of a silicon strip detector array for nuclear structure physics. *Nucl. Instrum. Meth. A*, 288:245, 1990.

[65] P. J. Sellin et al. A double-sided silicon strip detector system for proton radioactivity studies. *Nucl. Instrum. Meth. A*, 311:217, 1992.

[66] CAEN. http://www.caen.it.

[67] mesytec. http://www.mesytec.com/.

[68] MARaBOU Data Acquisition. http://www.bl.physik.uni-muenchen.de/marabou/html/.

[69] MBS. http://www-win.gsi.de/daq.

[70] R. Lutter. Med data structure. Unpublished, 2009.

[71] ROOT. http://root.cern.ch/.

[72] J. Van de Walle. *Coulomb excitation of neutron rich Zn isotopes*. PhD Thesis, Instituut voor Kern- en Stralingsfysica, KU, Leuven, 2006.

[73] C. D. Nesaraja et al. Nuclear Data Sheets for A = 58. *Nucl. Data Sheets*, 111:897, 2010.

[74] J. Blachot. Nuclear Data Sheets for A = 107. *Nucl. Data Sheets*, 109:1383, 2008.

[75] J. J. Ressler et al. β decay studies of ^{109,107}Sb. *Phys. Rev. C*, 65:044330, 2002.

[76] J. Blachot. Nuclear Data Sheets for A = 109. *Nucl. Data Sheets*, 107:355, 2006.

[77] I. Dankó et al. Low-lying states of ^{109}Sn from the ^{106}Cd(α, $n\gamma$) reaction. *Nucl. Phys. A*, 646:3, 1999.

[78] D. Cline and P. M. S. Lesser. Error estimation in non-linear least squares analysis of data. *Nucl. Instrum. Methods Phys. Res.*, 82:291, 1970.

[79] M. A. Schumaker et al. Coulomb excitation of radioactive ^{21}Na and its stable mirror ^{21}Ne. *Phys. Rev. C*, 78:044321, 2008.

[80] J. Eberz et al. Nuclear Spins, Moments and Charge Radii of $^{108-111}$Sn. *Z. Phys. A*, 326:121, 1987.

[81] F. Andreozzi et al. Realistic shell-model calculations for neutron deficient Sn isotopes. *Phys. Rev. C*, 54:1636, 1996.

[82] C. Fahlander et al. Excited states in ^{103}Sn: Neutron single-particle energies with respect to ^{100}Sn. *Phys. Rev. C*, 63:021307(R), 2001.

[83] M. E. J. Wigmans et al. Decay of ^{111,112,113,114,115}Sb. *Phys. Rev. C*, 14:229, 1976.

[84] P. H. Stelson. Coulomb excitation of ^{117,119}Sn. *Nucl. Phys. A*, 190:197, 1972.

[85] A. Blazhev et al. High-energy excited states in ^{98}Cd. *J. Phys. Conf. Ser.*, 205:012035, 2010.

[86] D. D. DiJulio et al. Sub-barrier Coulomb excitation of ^{107}Sn. *J. Phys. Conf. Ser. A*, 381:012073, 2012.

[87] D. D. DiJulio et al. Shell model based Coulomb excitation γ-ray intensity calculations in ^{107}Sn. *Phys. Scr. T*, 150:014012, 2012.

[88] H.-C. Hseuh and E. S. Macias. Identification of 2.90-min ^{107}Sn and 50-sec ^{107}In^{m}. *Phys. Rev. C*, 14:345, 1976.

[89] W. K. III Tuttle et al. Coulomb excitation of ^{113,115}In. *Phys. Rev. C*, 13:1036, 1976.

[90] E. M. Bernstein et al. Coulomb excitation of ^{113}In and ^{115}In with oxygen ions. *Nucl. Phys. A*, 141:67, 1970.

[91] A. Holt et al. Application of realistic effective interactions to the structure of the Zr isotopes. *Phys. Rev. C*, 61:064318, 2000.

[92] N. Boelaert et al. Low-spin electromagnetic transition probabilities in ^{102,104}Cd. *Phys. Rec. C*, 75:054311, 2007.

[93] N. Boelaert et al. Shell model description of the low-lying states of the neutron deficient Cd isotopes. *Phys. Rec. C*, 75:014316, 2007.

[94] K. Heyde et al. Unified description of odd-mass indium nuclei I. General theory and comparison to ^{113}In and ^{115}In levels populated in the decay of ^{113}Sn and ^{115}Cd^{m,g}. *Phys. Rev. C*, 17:1219, 1978.

[95] T. J. Humanic et al. Electromagnetic properties of excited states in the even-even erbium isotopes from Coulomb excitation studies. *Phys. Rev. C*, 27:550, 1983.

[96] C. Fahlander et al. Two-phonon γ-vibrational states in ^{166}Er. *Phys. Lett. B*, 388:475, 1996.

[97] P. E. Garrett et al. K$^{\pi}$ = 0^{+} and 4^{+} Two-Phonon γ-Vibrational States in ^{166}Er. *Phys. Rev. Lett.*, 78:4545, 1997.

[98] H. G. Börner et al. Evidence for the existence of two-phonon collective excitations in deformed nuclei. *Phys. Rev. Lett.*, 66:691, 1991.

[99] M. Oshima et al. Two-phonon γ-vibrational state in ^{168}Er. *Phys. Rev. C*, 52:3492, 1995.

[100] T. Härtlein et al. Collective excitations built on the 2^{+}_{γ} state in ^{168}Er. *Eur. Phys. J A*, 2:253, 1998.

[101] C. Y. Wu et al. Complex band interactions in ^{170}Er. *Phys. Rev. C*, 61:021305(R), 2000.

[102] A. Gadea et al. Status and test of the EUCLIDES Si-ball. LNL-INFN (REP)-160/2000, 1999.

[103] GASP @ lnl. http://gasp.lnl.infn.it/.

[104] D. Bazzacco and C. A. Ur. GSORT program. INFN, Sezione di Padova, Italy, 1997.

[105] Geant4. http://geant4.cern.ch/.

[106] C. M. Baglin. Nuclear Data Sheets for A = 170. *Nuclear Data Sheets*, 96:611, 2002.

[107] RadWare. http://radware.phy.ornl.gov.

[108] D. C. Radford. ESCL8R and LEVIT8R: Software for interactive graphical analysis of HPGe coincidence data sets. *Nucl. Instrum. Meth. A*, 361:297, 1995.

[109] C. Y. Wu et al. Electromagnetic properties of the rotationally aligned band in ^{162}Dy. *Phys. Rev. C*, 64:064317, 2001.

[110] C. Y. Wu. Electromagnetic properties of tungsten nuclei. *Nucl. Phys. A*, 533:359, 1991.

[111] B. Elbeck et al. Inelastic scattering from even rare earth isotopes. *Nucl Phys.*, 19:523, 1960.

[112] R. Graetzer and E. M. Bernstein. Double Coulomb Excitation with Oxygen Ions. *Phys. Rev.*, 129:1772, 1963.

[113] K. A. Erb et al. Quadrupole and Hexadecapole Deformations in Rare-Earth Nuclei. *Phys. Rev. Lett.*, 29:1010, 1972.

[114] S. H. Sie and D. W. Gebbie. Recoil-distance lifetime measurements of the ground-state band in ^{168}Dy, ^{170}Er and ^{174}Yb. *Nucl. Phys. A*, 289:217, 1977.

[115] O. Scholten, private communications.

[116] F. K. McGowan. Interacting boson approximation model analysis of $E2$ transition probabilities for transitions in $^{166-170}$Er. *Phys. Rev. C*, 24:1803, 1981.

[117] A. M. Demidov et al. Multipole Mixtures for $(2^+_\gamma - 2^+_g)$ Transitions in N = 90-110 Nonspherical Nuclei. *Phys. At. Nucl.*, 62:1271, 1999.

[118] B. Kotliński et al. Coulomb excitation of ^{168}Er. *Nucl. Phys. A*, 517:365, 1990.

[119] G. Alaga. Selection rules for beta and gamma particle transitions in strongly deformed nuclei. *Nucl. Phys.*, 4:625, 1957.

[120] K. Schreckenback and W. Gelletly. The nature of M1 admixtures in intra-band transitions in the γ-vibrational band. *Phys. Lett. B*, 94:298, 1980.

[121] H. S. Binarh et al. $B(E2)$ Branching and $E2/M1$ Mixing Ratios of Intra γ-Vibrational Band Transitions in Deformed Even-Even ($150 \leq A \leq 190$) Nuclei. *J. Phys. Soc. Japan*, 59:2359, 1990.

[122] W. Greiner. Magnetic properties of even nuclei. *Nucl. Phys.*, 80:417, 1966.

[123] FAIR. http://www.fair-center.eu/.

[124] R^{3}B. http://www-win.gsi.de/r3b.

[125] CALIFA status report. Available at http://www.iem.cfmac.csic.es/departamentos/nuclear/.

[126] The Svedberg Laboratory. http://www.tsl.uu.se/.

[127] H. Alvarez-Pol et al. Design studies and first crystal tests for the R^3B calorimeter. *Nucl. Instrum. Meth. B*, 266:4616, 2008.

[128] N. Iwasa et al. Measurement of the Coulomb Dissociation of ^8B at 254 MeV/nucleon and the ^8B Solar Neutrino Flux. *Phys. Rev. Lett.*, 83:2910, 1999.

[129] 3M Vikuiti. http://vikuiti.com/.

[130] G. Folger et al. The Binary Cascade. *Eur. Phys. J A*, 21:407, 2004.

[131] H. W. Bertini and M. P. Guthrie. News item results from medium-energy intranuclear-cascade calculation. *Nucl. Phys. A*, 169:670, 1971.

[132] A. Michalowicz. *Kinematics of nuclear reactions*. lliffe Books Ltd., London, 1967.